LARGE EDDY SIMULATION (LES) OF FLOW IN MEANDERING VEGETATED RIVER REACH OF PERAK RIVER

GOH HUAN TAO

MASTER OF ENGINEERING SCIENCE

FACULTY OF ENGINEERING AND GREEN TECHNOLOGY
UNIVERSITI TUNKU ABDUL RAHMAN
SEPTEMBER 2022

LARGE EDDY SIMULATION (LES) OF FLOW IN MEANDERING VEGETATED RIVER REACH OF PERAK RIVER

By

GOH HUAN TAO

A dissertation submitted to the Faculty of Engineering and Green Technology,
Universiti Tunku Abdul Rahman,
in partial fulfillment of the requirements for the degree of
Master of Engineering Science
September 2022

ABSTRACT

LARGE EDDY SIMULATION (LES) OF FLOW IN MEANDERING VEGETATED RIVER REACH OF PERAK RIVER

Goh Huan Tao

Low lying ground near lower reaches of Perak River in Malaysia has been facing several problems including constant floods, erosion and sediment deposition. Due to these issues, efforts are being made by the Perak state government to reinforce the banks of Perak River in Teluk Intan, to manage the water passage and to keep the depth for navigation purposes. The erosion of the river bank and the changes of the bed bathymetry in this area are mainly caused by the effects of the meandering river flow which tend to move the surface flow toward outer bank, but are a result of complex interaction of the river flow with the movement of the bed sediment and the vegetation in the flow passage and on the banks. The aim of this study is to develop a numerical method based on an advanced Large Eddy Simulation (LES) technique to simulate the river flow characteristic in the meandering river with vegetation. The LES method solves for the large-scale turbulent fluctuation including the free surface motion on fixed grid by modelling the effects of unresolved turbulent motion and the details of flow through vegetation. Several simulation calculations of the flow in meandering reach of Perak River in Teluk Intan, Perak with different conditions of vegetation and discharge rates have been conducted. Furthermore, in order to compare the simulation result with real situation, site survey has been conducted in the simulated river reach. The flow velocity distribution was measured by an

Acoustic Doppler Current Profiler (ADCP) and the changes of the surface elevation were monitored by water level gauges, sample collection of suspended solid and sedimentation have been conducted. Results from LES simulation and site survey have been compared. In conclusion, general flow characteristics with complex bathymetry and vegetation effects can be reproduced by this LES method which can further be used to examine the effects of any changes in river bed and bank conditions.

ACKNOWLEDGEMENTS

First and foremost, I would like to express my special thanks to my supervisor Prof. Dr. Akihiko Nakayama who has patiently guided me and given me a lot of valuable and sincere advice throughout the process. Also, I would like to express my appreciation to my co-supervisor Dr. Zafarullah Nizamani for his support and encouragement. I would like to express my appreciation to my family for helping and supporting me so patiently throughout the time.

Besides that, I would like to thank JPS (Jabatan Pengairan dan Saliran Malaysia) for providing data from site, and also resources during the site survey. Furthermore, I would like to thank PWRI Japan (Public Works Research Institute) for providing technical support, resources, and data during the site survey.

Last but not least, I would like to thank all the lecturers and fellow students who have participated and helped out during the site survey.

APPROVAL SHEET

This dissertation/thesis entitled "**LARGE EDDY SIMULATION (LES) OF FLOW IN MEANDERING VEGETATED RIVER REACH OF PERAK RIVER**" was prepared by GOH HUAN TAO and submitted as partial fulfillment of the requirements for the degree of Master of Engineering Science at Universiti Tunku Abdul Rahman.

Approved by:

Akihiko Nakayama

____

(Prof. Dr. Akihiko Nakayama) Date:…09/09/2022..

Supervisor

Department of Environmental Engineering

Faculty of Engineering and Green Technology

Universiti Tunku Abdul Rahman

____

(Dr. Zafarullah Nizamani) Date: …09/09/2022..

Co-supervisor

Department of Environmental Engineering

Faculty of Engineering and Green Technology

Universiti Tunku Abdul Rahman

FACULTY OF ENGINEERING AND GREEN TECHNOLOGY

UNIVERSITI TUNKU ABDUL RAHMAN

Date: 09th September 2022

SUBMISSION OF DISSERTATION

It is hereby certified that **GOH HUAN TAO** (ID No:**17AGM00772**) has completed this dissertation entitled "LARGE EDDY SIMULATION (LES)OF FLOW IN MEANDERING VEGETATED RIVER REACH OF PERAK RIVER" under the supervision of Prof. Dr. Akihiko Nakayama (Supervisor) from the Department of Environmental Engineering, Faculty of Engineering and Green Technology , and Dr. Zafarullah Nizamani (Co-Supervisor) from the Department of Environmental Engineering, Faculty of Engineering and Green Technology.

I understand that University will upload softcopy of my dissertation in pdf format into UTAR Institutional Repository, which may be made accessible to UTAR community and public.

Yours truly,

____

(Goh Huan Tao)

DECLARATION

I hereby declare that the dissertation is based on my original work except for quotations and citations which have been duly acknowledged. I also declare that it has not been previously or concurrently submitted for any other degree at UTAR or other institutions.

Name Goh Huan Tao

Date 09-09-2022

TABLE OF CONTENTS

LIST OF TABLES

LIST OF FIGURES

LIST OF SYMBOLS AND ABBREVIATION

Symbols/Abbreviations

ADCP	Acoustic doppler current profiler
ADVP	Acoustic dropper Velocity profiler
B	Width of channel
CFD	Computational Fluid Dynamics
Cs	the Smagorinksy constant
C_v	Average drag coefficient
D	Coefficient of molecular diffusion
D_z	Two-dimensional divergence
DID	Department of Irrigation and Drainage
DDMRC	District Disaster Management and Relief Committee
DNS	Direct numeric simulation
DRM	Disaster risk management
DM	Disaster management
K_s	Roughness height
LES	Large eddy simulation
MFDRPM	Malaysia Flood Disaster Relief and Preparedness Machinery
My DIMS	National Disaster Information Management System
MNSC	Malaysia National Security Council
NADMA	National Disaster Management Agency
NCDMM	National Crises and Disaster Management Mechanism
NFDMRC	National Flood Disaster Management Relief Committee
NDCC	National Disaster Control Centre
NSD	National Security Division
NDMRC	National Disaster Management and Relief Committee

PKOB	Centre of Disaster Operation Control
Q	Flow rate
RANS	Reynolds-averaged Navier–Stokes equations
Re	Reynold number
r_i	Curvature radius at the inner bank
SDMRC	State Disaster Management and Relief Committee
t	time
<tke>/(1/2u_*^2)	Normalized depth-averaged turbulent kinetic energy
$U_n h/UH$	Normalized depth-averaged transverse unit discharge
U_s/U	Depth average streamwise velocity
$U_s h/UH$	Normalized depth-average streamwise unit discharge
u_τ	Friction velocity
U_Z/U	and normalized depth-average vertical velocity
v	kinematic viscosity of water
V_{av}	Bulk velocity
v_n^+	Wall normal velocity
v_{sgs}	Effective kinematics viscosity
ψ	Stream function
ω_z	Vorticity
$(<\omega_s>H/U$	Depth-average streamwise vorticity
$\underline{Z}_b$	Vertical coordinate of the bottom
Ρ	Density
τ	Effective stress
$\gamma_x, \gamma_y, \gamma_z$	sub-grid transport in direction of x, y, and z respectively
Δ	geometric average
τ_w	Wall stress
Λ	Average density of surface area

CHAPTER 1

INTRODUCTION

1.1 Background

Water covers as much as 71% of the total surface of the earth. The largest amount is contained in the ocean amounting about 1338,000,000 km^3 which is 96.54% of total water volume from the earth. The volume of water in the rivers 2,120 km^3 which is 0.0002% of total volume. (Gleick, 1993)

Although rivers constitute only 0002% of total water volume on the earth, historical facts showed that rivers play a very important role in human civilization. It is found that human civilization originated alongside rivers including Tigris River, Euphrates River, Niles River, Indus River, Yellow River. The most important and influential functions of rivers to human kind include freshwater supply, agricultural irrigation, sanitation, transportation, ecological function, and etc.

Rivers are beneficial to human not only in supplying freshwater as a biological demand, lot of values that can be harvested from the rivers. For instance, rivers play a significant role in agriculture. Substances such as nutrient, organic matter, water are exchanged by streamflow. The most exchanged aquifer-river water located at the water-filled space beneath the riverbed, which is termed as a hyporheic zone. (Gibert, Danielopol and Standford, 1994) Natural terrains that are formed by rivers provide living conditions to plants including crops.

Besides, forces that generated by river flow can be harnessed mechanically and converted into electricity. One of the greatest achievements of mankind in history is the usage of electricity. The International Energy Agency had made a report to evaluate the power generation by each different source including coal, natural gas, hydro, nuclear fission, and other renewable source. It is reviewed that among the clean energy sources, hydropower contributes the most to the total energy yield, which is more than the total of combined energy sources that is generated. (International Energy Agency, 2021)

Unfortunately, rivers bring harms and disasters to human kind. According to Department of Irrigation and Drainage Malaysia, there is a total of 189 river basins flowing directly into South China Sea whereby 85 of the aforementioned are prone to recurrent flooding. The total area vulnerable to flood disaster is estimated to be roughly about 29,800km^2 which is 9% of the total land area in Malaysia. (Department of Irrigation and Drainage, 2012)

There are many important characteristics of a river being exhibited by Perak River in Teluk Intan, such as meander, vegetation, active transportation of sedimentation. Therefore this river obviously satisfies the criteria to be chosen as the case study for the Large Eddy Simulation (LES). The Large Eddy Simulation (LES) methods have been developed and applied to various engineering flows, nevertheless application to rial rivers with these characteristics have not been fully explored. The present work implements the detailed methods of reflecting features of the real rivers including acute meander with complex bathymetry and vegetation in the latest LES method and applies to the real flow of Perak River near Teluk Intan. For the welfare of the country, problems pertaining to the river such as flood should not be neglected and proper river management should be prioritized. In order to prevent massive losses which caused by flood, prediction could be made so that prior action could be taken. In order to predict the trend of flood occurrence, further understanding of flow characteristic of the river is needed. With the development of LES method, it should be able to review the effects and correlation of the meander, vegetation and sedimentation. Result of LES should be able to provide a reference or option to the authorities for better policymaking.

1.2 Problem Statement

In the lower part of Sungai Perak in Teluk Intan which is also the area of low-lying ground level, flood and bank erosion occur frequently. As mentioned previously in the background study, several projects have been conducted by the state government for river bank reinforcement due to the problem of bank erosion. Development of simulation can be helpful in providing information as reference for preventive actions and decision making, such information include flow characteristic, area that are prone to flooding or bank erosion and more.

Due to the complexity of river's characteristics such as meander effects, vegetation effects, topographic steering and etc, difficulty for development of numerical simulation could be found in several aspects. Various studies and methods have been conducted such as numerical modelling, laboratory experiment, field investigation and more in order to investigate the characteristics of natural rivers. However, despite the great number of researches that have been done, there are still a number of uncertainties and undiscovered factors (Balen, 2010), for example vegetation effects, which is pointed out in (Termini, 2017) and (Termini,2018) that although most of the researches have reached an understanding that vegetation's effects strongly affect river dynamics. However understanding of the relation between vegetation and river morphodynamics still remain weak.

With the rapid development and advancement of computational technology, 3D flow modelling has become more practical. Most of the characteristic of the flow are able to be resolved. Nevertheless, there are few limitations in these modelling such as the accuracy prediction in the point bar and the pool zone is low. Moreover, usage of these models are often limited to small-scale and short term (Balen et.al, 2010). Different types of simulation have been done such as DNS, RANS, and LES by (Balen et.al, 2010), (Shimada et.al, 2011), (Lee and Choi, 2017) and etc. Most of the simulation result remarkably resolved the flow characteristic. Since most of the simulation are dependent on high computing power due to their choice of numerical model and algorithm, in addition to application on river with complicated conditions they are restricted to less complex and smaller scale configurations, such as laboratory based experiment or small-scale field survey. In addition, most of the simulation model are developed in a manner that river flow calculation is set within a fix river bank shape. As a result, they are unable to simulate or predict certain phenomena such as floods breaking banks.

As a result, for the facts that aforementioned, only few applications of simulation have been done in real river with more complex condition. There are few simulations that are applied in real river in Western Japan which is Ibogawa River by (Nakayama, 2012) and (Nakayama and Asami, 2020) using KULES method. The KULES method is capable in simulating cases with larger scale with limited computing power comparing to other simulation methods. Furthermore, complex condition including complex river bed morphology, meander effect, vegetation effect, river bed coarse and etc. can be taken into consideration. The KULES method is also the simulation method that is used in present study.

Although KULES method is capable with complex situation and has reproduced the important flow characteristic in Ibogawa River in a satisfactory manner (Nakayama, 2012), how well it can be adopted in Sungai Perak in Teluk Intan remain unclear due to the differences between the two rivers. In addition, calculation of sediment transportation is not included in KULES. As a consequence, simulation of sediment transport is not possible. Whereas, bed shear stress is being calculated is directly related to the sediment transport provides insight related to sediment transport which will be further discussed in the result and discussion section.

Overall, comparison with field survey and other researcher's work are necessary in order to verify the simulation result.

1.3 Research objectives

The aims of this study are:

- To develop a simulation method for a meandering river with vegetation based on LES with the river characteristics such as curvature effects, interaction with riparian vegetation and transportation of floating object can be represented.
- To obtain flow characteristic and bed shear stress calculation by conducting LES simulation.
- To obtain flow characteristic and sediment characteristic by field survey.
- Examine the effects of meander and vegetation by examine LES simulation runs with different conditions against data collected from site.

CHAPTER 2

LITERATURE REVIEW

2.1 Floods in Malaysia

Flood happened when river could no longer contain the discharge from its catchment and the bank full stage is exceeded (Sharma and Priya, 2001). There are various types of classification of floods depending on geographical setting (Mohd Taib, Jaharuddin and Mansor, 2016). In Malaysia, flood is categorized into flash flood and monsoon flood according to the period for the river to recede to its normal level (DID, 2000). As mentioned previously, 85 of 189 river that flow directly to South China Sea are prone to recurrent flooding. The area is estimated roughly to be about 29800km^2 which is shown in Figure 2.1 below.

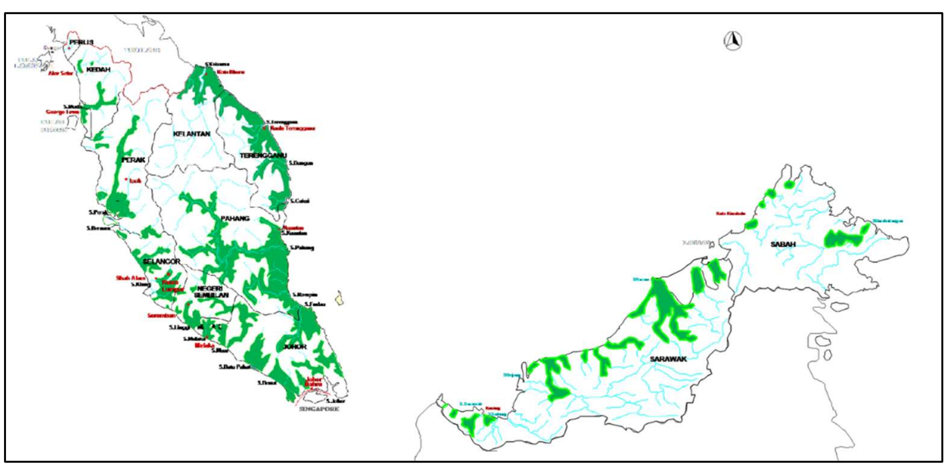

Figure 2.1: Area Prone to Flood in Malaysia (Drainage and Irrigation Department Malaysia, 2012)

Furthermore, as a main disaster in Malaysia, flood has the highest occurrence rate of 62.5% among other disaster including drought, landslide, storm, etc. The frequency is shown in Figure 2.2 below. Not to mention, the mortality rate from flood is 24.1% which is not the highest among the all, but it has the highest impact on the economy compare to all the other disasters, that is 60% as shown in Figure 2.3a and Figure 2.3b below. Such massive loss could be seen during the most devastating flood, which is the 2014-15 Malaysia flood. The flood happened mostly in the east coast and northern region of Peninsular Malaysia starting from 15 December 2014 until 3 January 2015. Total number of 3390 people in Kelantan and 4209 in Terengganu was evacuated. While the precipitations kept increasing, water level of several rivers in Kelantan, Pahang, Perak, and Terengganu rose beyond the safety level.

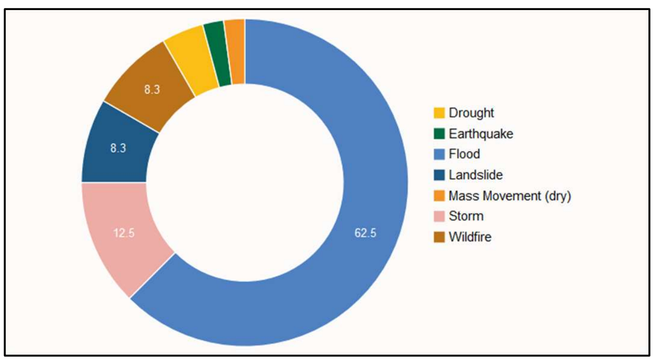

Figure 2.2: Frequency of Different Types of Natural Disaster Occurred in Malaysia (EM-DAT, 2015)

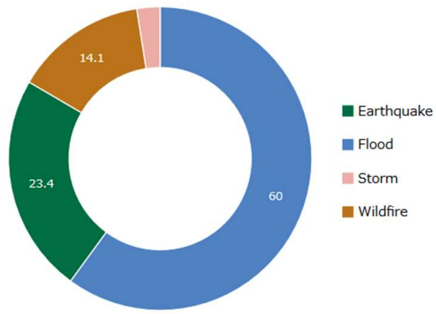

a) Economic Loss of Different Types of Natural Disaster in Malaysia

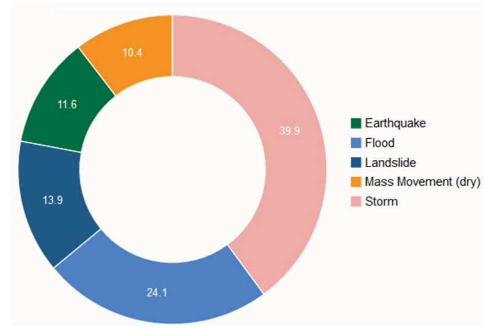

b) Mortality of Different Types of Natural Disaster in Malaysia

Figure 2.3: Impact from Different Types of Natural Disaster in Malaysia (EM-DAT, 2015)

As a result, total number of 60,000 people were evacuated the following days (Estrada *et al.*, 2017). Moreover, the losses that caused by the flood were estimated to be around 1 billion ringgits by Malaysian government. In which, 100 million ringgits and 132 million ringgits are allocated to road repairing in Kelantan and Terengganu respectively (Estrada *et al.*, 2017). This showed that both the preparedness and post handling of flood are equally important.

2.1.1 Structure of disaster management and policy of Malaysia

In general, Disaster management is mainly depending on top-down centred machinery and is considered as a government function. (Chan, 2015). The structure of the management system is shown as Figure 2.4 below. National Security Division (NSD) at the very top of the organization is directly under the Prime Minister’s Department, moreover the activities which the department in charge include preparation, prevention, response and handling of disaster. There are three levels of disaster level including federal level, state level, and district level. Furthermore, they are managed by National Disaster Management and Relief Committee (NDMRC), State Disaster Management and Relief Committee (SDMRC) and District Disaster Management and Relief Committee (DDMRC) respectively. In addition, village-level disasters are also managed by DDMRC (Chan, 2015).

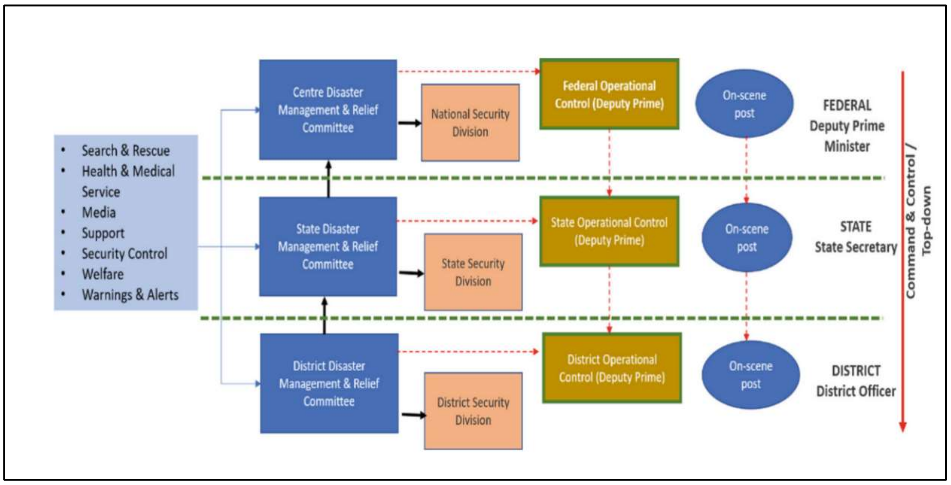

Figure 2.4: Disaster Management Structure in Malaysia (Che Hamid et al., 2019)

In year 1997, national policy, management mechanism and disaster aid known as Directive No. 20. MNSC was formulated by the Malaysia National Security Council (MNSC) (Che Hamid *et al.*, 2019). During October of year 2015, a special agency which is National Disaster Management Agency (NADMA), was established by the federal government dedicated to disaster risk management (DRM) (Che Hamid *et al.*, 2019). Regarding to the Disaster management (DM) structure of Malaysia, seven service themes were established as shown as left hand side in Figure 2.4.The seven services include search and rescue, health and medical, media, support, security control, welfare, and warnings and alerts.

On the other hand, the purpose of National Disaster Control Centre (NDCC) is set to be the Centre of Disaster Operation Control (PKOB) when disaster strike. The workflow of NDCC is shown as Figure 2.5 below which is done by interviewing with staff from NDCC (Che Hamid *et al.*, 2019).

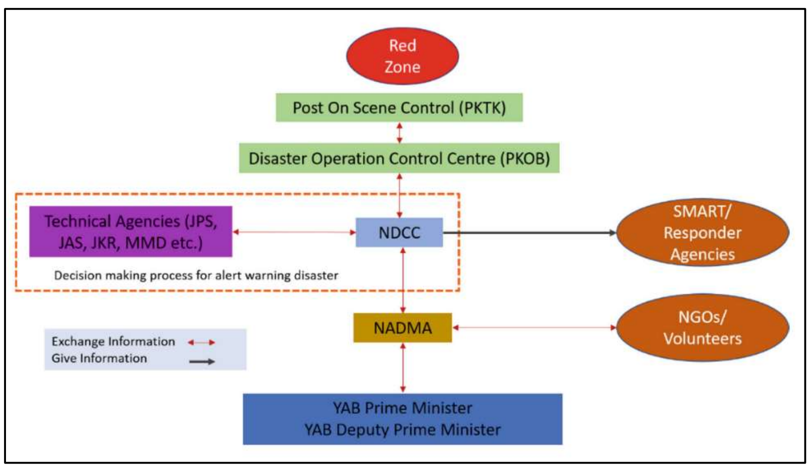

Figure 2.5: Workflow of NDCC (Che Hamid et al., 2019)

A disaster managing system called National Disaster Information Management System (My DIMS) which encompass four phases of disaster management activities was developed and used by NDCC. In which, the four phases include mitigation, inventory, reaction and recovery. Moreover, My DIMS is also capable in several tasks including providing real-time disaster warning, alarm monitoring, and real-time dissemination. The real-time dissemination could be done in several ways including short messaging service (SMS), fax, phone calls, and the disaster portal. Not to mention, the system also acts as an important rule to coordinate information from various sources especially from technical agency (Che Hamid *et al.*, 2019).

2.1.2 Flood management in Malaysia

In the year of 1971, soon after the formation of National Disaster Management and Relief Committee (NDMRC), Set up for Malaysia Flood Disaster Relief and Preparedness Machinery (MFDRPM) was done. The committee of NDMRC is responsible for planning, coordinating, and supervising relief operation during floods (Chan, 2015). While NDMRC as the very top of the management structure, the committee runs a management mechanism which is the National Crises and Disaster Management Mechanism (NCDMM). The purpose for NCDMM to be established is to coordinate relief operation among federal, state, and district level in order to assist victim effectively (Chia, 2004). During the flood events, the NCDMM will be called as National Flood Disaster Relief Machinery (NFDRM), which is a reactive system basically. On the other hand, in related to flood, the operation of disaster relief will be handled by National Flood Disaster Management Relief Committee (NFDMRC). Whether or not any district, state, or even whole nation level is eligible for financial assistance from government, will depend on the declaration from NFDMRC(Chan, 2015). Although the operation at the nation, state, district, and village level seems to be in charged by NFDMRC, in reality NFDMRC coordinates operation at the state level in terms of national level and overseas operation Furthermore, since most of the state activities are handled by respective state authorities, therefore, aids and assistance which can be provided to flood victims effectively are the main task for NFDMRC (Chan, 2015). As an example for the operation of NFDMRC, in order to organize readiness of flood disaster, evacuation, and recovery work, the body will hold meeting annually before the northeast monsoon season. (Chan, 2015). Flood mitigation policy and strategies in Malaysia consist of two measures, which are structural and non-structural measures. Namely as an example, construction of dams and embankments for flood control is structural measure. Usage of flood forecasting and warning system on the other hand is considered as non-structural measure (Chan, 2015).

Ir. Hj Ahmad Hussaini, Director General of DID Malaysia state that during the implementation of flood mitigation measure, policy guideline should include implementations in several aspect such as structural measures, complementary non-structural measures, flood forecasting system and etc.

Furthermore, he also stated that some flood management activities undertaken including study of the national water resources, development of flood forecasting Flood forecasting and warning system such as "Infobanjir" and “Flood Watch” and also writing of manual regarding to the urban storm-water management for Malaysia (MSMA).

As a technical agency, the Department of Irrigation and Drainage (JPS) provide flood forecasting and warning service to the public. The National Flood Monitoring System is established on the internet and can be access through the website: (http://infobanjir. moa.my). As a result, water level data and rainfall data could be collected nationwide.

2.1.3 Limitations of Flood Management and Recommendations for Improvement

The expenses on the flood mitigation by Malaysian government has been increased substantially. During the first Malaysia economic plan, only 4.56 million USD dollars are allocated for the flood mitigation purpose. While it was seem to be less, the expenditure has increased to massive amount of 228.2 million USD dollars during the Sixth Malaysia plan (Chan, 2015). In another terms, the country's financial allocation on flood mitigation has been increased by 50 times over the 20 years. Therefore, it could be said that with the increase implemented measures on flood control and relief, flood mitigation policy of Malaysia is worth mentioning (Chan, 2015). However, there are still several limitations in some aspect including the management strategies, policies, flood related legislation, warning system etc.

As mentioned in section 2.1.2, flood mitigation and strategies in Malaysia include two measures, which are structural measures, and non-structural measures. Based on structural measures, Malaysia government has been conducting a few numbers of flood mitigation project such as raising river embankment, building multi-purpose dam and so forth. However, structural measures are still more preferable despite of its high costing comparing to non-structural measures. The fund that allocated for such project increase significantly in every five years development plan of Malaysia. Although it may not seem bad since it might show the effort of the government on the other way, however the fact of increasing strain on the government is tangible. Moreover, flood forecasting and warning system as one of the non-structural measure, seems to be inadequate in some field. According to (Chan, 2015), rather than inputting forecast from radar or satellite into computer model, current flood warning system in Malaysia is using river level as input. As a consequence, the performance of the current flood forecasting and warning system has not reached its maximum and is seemingly ineffective. Besides that, the total number of telemetric stations for rainfall and river flow seem large enough. However, their distribution in fact is uneven whereby the stations are located in populated areas while it has not been set up in sparsely populated areas (Chan, 2015). It could be concluded that the current flood management models in Malaysia is lack of multi-disciplinary approach, both structural and non-structural measures should be adopted evenly (Chan, 2015). Therefore, while setting the objective to development of method in a more proactive manner, the flood mitigation strategies should be re-examined in order to solve the problem in a holistic manner (Chan, 2015).

From the aspect of legislation, not only the regulation of law is sector-based and outdated, there is no any law that is set in related to flood. Although there are some river regulation laws that include flood mitigation measurements, they are seemingly less clear and forceful. Therefore, in a sense of direct control of usage of water which may affect flooding, more rigid and clear-cut law must be passed to corresponding authorities including the aspect of clearly specified all specs of flood mitigation, flood plain management, and water resource development.(Chan, 2015).

Finally, (Chan, 2015) also pointed out that the need for creating data management system. Namely, which is a database that that data would be displayed spatially and temporally so that it could support communication system in flood disaster management in a more systematic manner. At the current situation, most of the disaster related information are seldom released to public whereby, the information is often treated as "confidential". However, it should be noted that the statistic related to disaster should be opened to the public since they have the right. Therefore, it would be optimal if a geographical information system environment could be used for the data bank management and the data bank could be accessed by all disaster organization (Chan, 2015).

2.2 Computational Fluid Dynamics (CFD)

Physicist Maxwell once said that "All the mathematical sciences are founded on relation between physical laws and laws of numbers, so that the aim of exact science is to reduce the problems of nature to the determination of quantities by operations with numbers." - (James Clerk Maxwell, 1856).

Physically speaking, the mechanics of any fluids are basically govern by 3 equations describing basic laws below which include:

a) Law of conservation of mass

b) Newton's second law of motion

c) Law of conservation of energy

These fundamental laws of physics could be expressed by basic mathematical equations, which is formed by either integral equation or partial equation. The main core of CFD is the replacement of integrals or the partial derivatives with discretized algebraic form in these equations in order to obtain values for the field values at discrete points (both in time and space (Anderson Jr., 1995). In addition, usage of numerical analysis and data structure are involved to breakdown and solve the mechanism of fluid dynamics (Versteeg and Malalasekera, 2007). Nevertheless, the final product of CFD will be collection of numerical data rather that closed form analytical solution.

Fluid mechanics has developed since early history, the earliest literature about fluid mechanics that could be traced was written on parchment by

Archimedes, which is “On Floating Bodies”. Others who had made great contributions in this field including Leonhard Euler, Jean Le Rond d’Alembert, Joseph Louis Lagrange, Pierre Simon Laplace, Simeon Denis Poisson, Gauss etc. Their work carried great influence on numeric analysis of inviscid flow.

On the other hand, Osborne Reynolds, Geoffrey Ingram Taylor and others had worked through a lot including viscid, inviscid flow, and turbulent flow. Fluid mechanics was not treated individually until the publication of “Mathematical Principles of Natural Philosophy” by Isaac Newton during the year 1687. Along with the publication, concept of fluid mechanics had been brought to a new level, which was a remarkable moment throughout history.

2.3 An Introduction to Large Eddy Simulation (LES)

During 1963, Joseph Smagorinsky had proposed a methamatical method in order to simulate atmospheric air current, that is called Large Eddy Simulation (LES) (Smagorinsky, 1963). Most of the methods of Simulation are done by solving Navier-Stroke equation as used in LES method. The main idea of LES is that turbulent motion are separated into large scale and small scale. Large scales are resolved while small scales are modelled.(Rodi, Constantinescu and Stoesser, 2013)Therefore, LES has reduced the computational cost since the small-scale turbulence are the most expensive part to be resolved. Moreover, method such as direct numeric simulation (DNS) resolve every turbulent scale directly regardless of the turbulence scale, which is computationally expensive. Although other method such as RANS need less of the computational power,

2.4 Characteristic of Meandering River

In order to create numerical simulation on river with meander, it is important to understand its characteristic. River meander is one of the major features of stream flow. Formation of the river meander involve scouring of the riverbank and deposition of sedimentation.

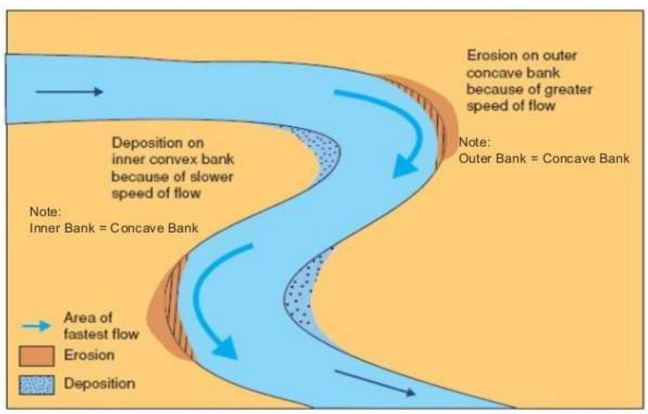

Figure 2.6: Formation of Meander

Meander of river is formed as outer concave bank are eroded and process of sediment deposition at the inner convex bank. The reason of the phenomena is due to difference flow velocity between outer bank and inner bank. Higher velocity at the outer riverbank will have scouring effect, while sediments carried by river flow will deposit at a slower velocity which happened at inner bank as shown in Figure 2.6. As time goes by, curvature of the meander could become bigger or even migrate. According to (Blanckaert, 2010), meander migration will cause shifting boundaries which will result in some problem including threatened property loss, fertile soil losses, and etc. Therefore, it has been a challenge for river management to understand and handle the threat well. Furthermore, meandering rivers had been studied by a range of scientist and practitioners for centuries. Despite that massive research had been conducted which cover aspect such as laboratory experiment, field investigation and numerical modelling, analytical method still consist a lot of uncertainty. In addition, along with the improvement of computational power, fully 3D has become feasible. Although characteristic of flow and bed topography could be resolved by these model, but still a lot of the method are remain in small scale and short-term configuration. (Blanckaert, 2010)

2.4.1 Laboratory study of meander bends of river

Therefore, Blanckaert had set up an experiment with a sharply curved laboratory flume in order to provide insight of meandering river, which is shown as Figure 2.7a. below. Since the curve open channel flow from Blanckaert's experiment has some similarity with the meander river in Teluk Intan which is shown in Figure 2.7b., it would be significant to make comparison between the two.

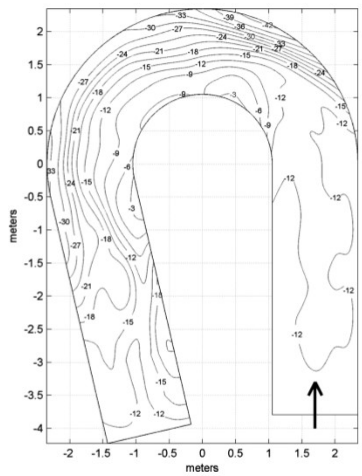

a) Module of the curve open-channel flow from Blanckaert's experiment

b) Meandering River in Teluk Intan

Figure 2.7: Blankcaert's Experiment

The meandering curve from Blanckaert's experiment had been studied, referred, and compared with result from various simulation including RANS, LES, etc. by several researcher. Blanckaert conducted the experiment aforementioned not only to review the experimental technique, procedure of data treatment, but also discover the nature of flow characteristic especially in sharp mender bend. Many phenomena regarding hydrodynamic as well as sedimentation transport (topography steering) are elaborated and explained in his work which include generation of secondary flow, momentum redistribution, occurrence of horizontal flow recirculation. Most importantly, analyzation of result also has been done to evaluate how the result could be used by others in order to validate result from various type of simulation model.

The experiment was conducted in a sharply curved laboratory flume, whereby the curvature reach 193° as shown as Figure 2.8 below. Maximum width of the flume B=1.3m is set to prevent narrow channel according to (Blanckaert, 2010) , centreline radius of curvature was set to be R=1.7m. Straight inflow reach, which had a length of 9m, was installed before the entrance of the sharp bend, while the straight outflow reach was set to be 5m.

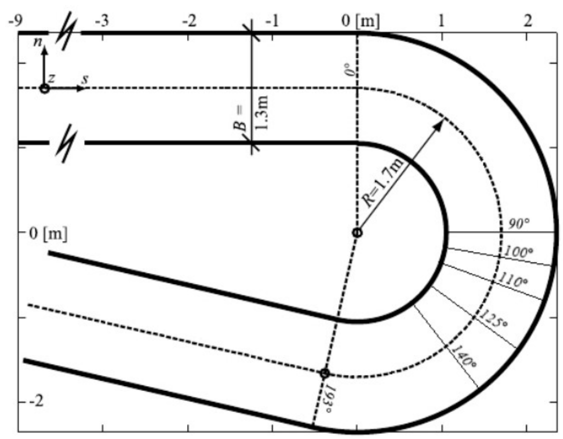

Figure 2.8: Curve Laboratory Flume Set Up by Blanckaert

Flow discharge of the flume was set to be $89Ls^{-1}$ and sediment was continuously fed in at the rate of $0.023kgs^{-1}m^{-1}$. Other parameter are also listed at table 2.1 below.

Table 2.1: Setting of the Curve Laboratory Flume

Description	Value
Inflow reach	9m
Outflow reach	5m
Centre Radius of curvature	1.7m
Maximum Bend	193°
Flow discharge	$89Ls^{-1}$
Sediment entrance rate	$0.023kgs^{-1}m^{-1}$

Two ADVP, which were symmetrical and asymmetrical style, installed near both the inner bank and outer bank as shown as Figure 2.10 below. Transducer were placed inside water-filled housing, the device then was placed on the water with its transparent mylar film touching the water surface. The cross-sectional measurements, which were done by ADVP, are shown in Figure 2.9 below. Implementation of the setting aforementioned, disturbance of the flow on the water surface will be reduced therefore minimizing the systematically error (Lemmin and Rolland, 1997). Eight echo sounders were then moved along the laboratory flume by a carriage at certain point in order to measure water surface and bed topography. Point of the measurement are illustrated at table 2.2 below. Additional bed topography are provided by ADVP measurement. Treatment of the measurement data was done in order to have better result, this process included extrapolation near the water surface, assembling data on overlapping grids, and splining of the measure pattern (Blanckaert, 2010).

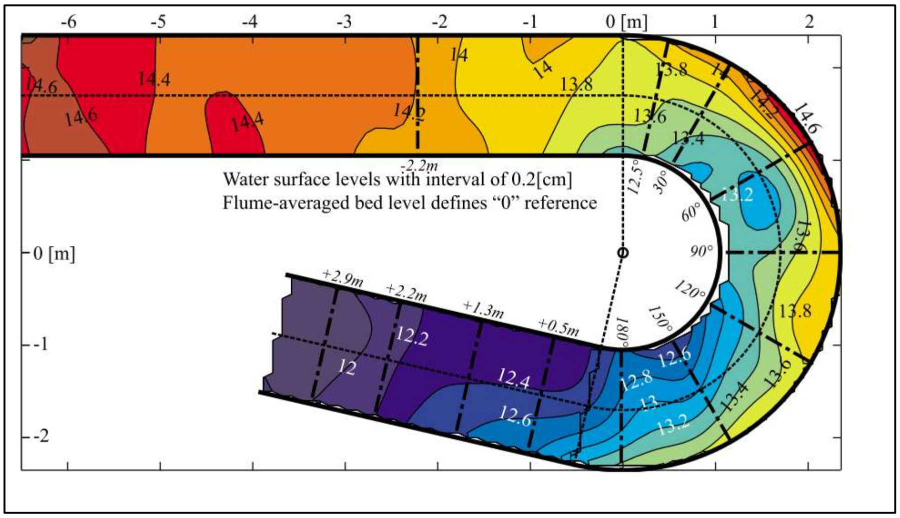

Figure 2.9: Position of ADVP Measurement which is Shown by Transverse Dash Line

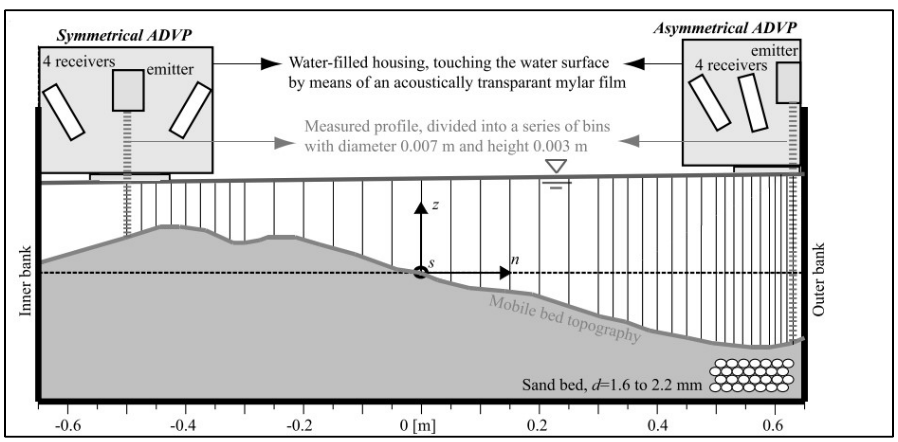

Figure 2.10: Transverse Illustration of ADVP Position at 120°

Table 2.2: Position of Transverse Measurement of Water Surface and Bed Topography Done by Echo Sounder.

Position at inflow (m)	−6.5, −6.3, −6.1, −5.9, −5.7, −5.5, −5.3, −5.1, −4.9, −4.7, −4.5, −4.3, −4.1, −3.9, −3.7, −3.5, −3.3, −3.1, −2.9, −2.7, −2.5, −2.3, −2.1, −1.9, −1.7, −1.5, −1.4, −1.3, −1.2, −1.1, −1, −0.9, −0.8, −0.7, −0.6, −0.5, −0.4, −0.3, −0.2, −0.1, −0.02
Position at bend (°)	0, 2.5, 5, 7.5, 10, 12.5, 15, 20, 25, 30, 35, 40, 45,50, 55, 60, 65, 70, 75, 80, 85, 90, 95, 100, 105, 110, 115, 120, 125, 130, 135, 140, 145, 150, 155, 160, 165, 170, 175, 180, 182.5, 185, 187.5, 190, 193
Position at outflow	0.01, 0.035, 0.5, 0.075, 0.1, 0.125, 0.15, 0.175, 0.2, 0.25, 0.3, 0.35, 0.4, 0.45, 0.5, 0.6, 0.7, 0.8, 0.9, 1, 1.1, 1.2, 1.3, 1.4, 1.5, 1.7, 1.9, 2.1, 2.3, 2.5, 2.7, 2.9, 3.1, 3.3, 3.5, 3.7, 3.9, 4.1

Formation of the bed topography are seemingly interesting, development of dunes, pool and point bar could be seen as shown in Figure 2.11 below. The area of the pool and point bar are plotted by white line whereby point bar area are located near inner bank while the pool is more on the outer bank side. Since the echo sounder's spatial resolution is not capable enough to resolve the dune, therefor the position of the dunes was superimposed. The characteristics and location were observed through photograph. Numbering in Figure 2.11 is the positions of the dunes while their characteristics are listed in table 2.3 below accordingly to the numbers.

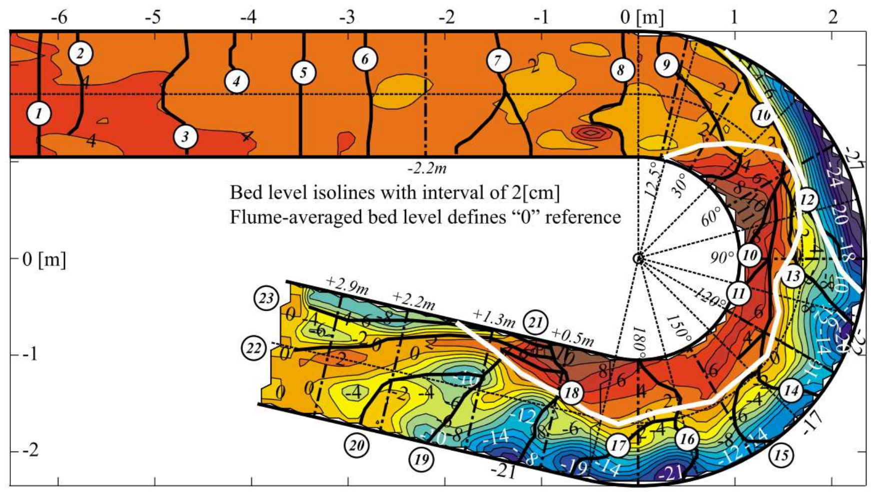

Figure 2.11: Bed Topography with Position of Dunes, Point Bar and Pool

Table 2.3: Characteristic of Each Dune Around the Laboratory Flume

No	Characteristic
1-8	Located in straight inflow, with amplitude less than 1 cm
9	Amplitude less than 1 cm
10	Dune like form corresponding to border of point bar
11	Kind of streamwise ridge with amplitude less than 5 cm
12	Kind of streamwise ridge on separation point bar with amplitude around 5 cm.
13-14	Oblique dune as well as streamwise ridge, with increasing amplitude outward onto 5-10 cm.
15	Oblique dune in outer half of corss-section, with amplitude less than 5cm

16	Irregular dune with amplitude increasing outward onto 5-10 cm
17	Oblique dune in outer half cross section with amplitude 5-10 cm
18	Irregular dune, with amplitude around 1cm within half of cross-section and increasing outward onto 5-10 cm
19	Oblique dune with amplitude around 5cm, maximum of about 10 cm just inward of centre line
20	Oblique dune, kind of streamwise gully, with amplitude around 5 cm
21-23	Streamwise gully, about 10 cm deep.

According to (Blanckaert, 2010), depth average quantities as a means of depth average numerical model are often used in morphodynamics calculation to describe flow field. Such depth average quantities include normalized depth-average streamwise unit discharge $(U_s h/UH)$, normalized depth -average tranverse unit discharge $(\mathrm{U_n\ h/UH})$, depth - average streamwise velocity $(\mathrm{U_s/U})$, and depth - average streamwise vorticity $(<\omega_s> \mathrm{H/U})$.

Location of the first moment (centre gravity) was illustrated by normalized depth-average streamwise unit discharge $(U_s h/UH)$, and normalized depth -average tranverse unit discharge $(\mathrm{U_n\ h/UH})$. Value of $U_s h$ resemble the increment of potential vortex distribution from outer bank to inner bank. Figure 2.12 describe the value of normalized depth-average streamwise unit discharge.

In Figure 2.12, while black vectors represent ($<<U_s h>>$, $<<U_n h>>$)/UH, black lines indicate first moment of the distribution of ($U_s h/UH$)

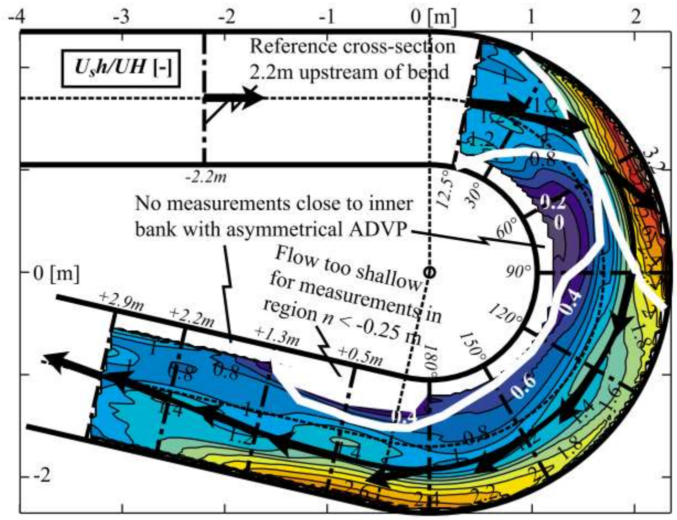

Figure 2.12: Normalized Depth-averaged Streamwise Unit Dischrage ($U_s h/UH$)

On the other hand, normalized depth-average transverse unit discharge ($U_n h/UH$) which is shown at Figure 2.13 below, has close relation with mass transportation. Inward mass transport occur when $U_n h$ less than 0 while outward mass transport happened when $U_n h$ is higher than 0 (Blanckaert, 2010). These values well illustrate the intricate interaction between the flow, sediment transport, flow distribution etc. With the value of $U_n h>0$, and maximum value of $U_n h/UH \approx 0.7$at the bending from 10° to 80°, suggests that there is tendency for the flow colliding to the outer bank while going straight. As a result, the core of maximum streamwise unit discharge is found at 60° bend cross section at the deepest part and has shifted outward.

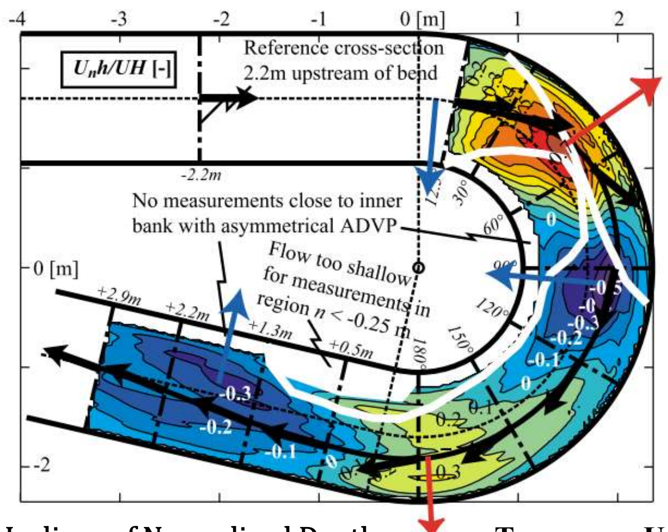

Figure 2.13. Isolines of Normalized Depth-average Transverse Unit Discharge (U_nh/UH)

Inward mass transportation happened at the bend region from 90° to 150°. The process is indicated by the blue arrow in Figure 2.13. Erosion could be seen at the outer bank near the 60° bend region. From Figure 2.14, it could have seen that transverse tilting of the water surface decay after the 150° bend region. The decaying of the water surface causes the flow to be accelerated at the outer half cross section, while the flow at inner half cross section is decelerated. The phenomena aforementioned are clearly resembled in Figure 2.12 previously. There is horizontal flow recirculation occur over the shallow point bar at the bend section from 40° to 120°, which is well represented by value of normalized depth-averaged streamwise velocity. Region of flow recirculation are shown in

Figure 2.15 below which indicate the value of normalized depth-average streamwise velocity (U_S/U).

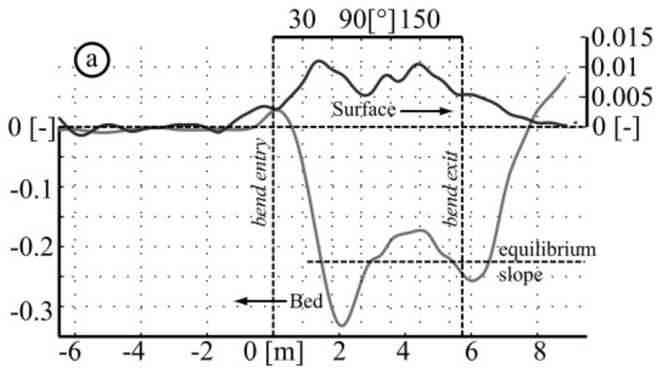

Figure 2.14: Streamwise Evolution of Transverse Bed Slope and Water Surface Slope

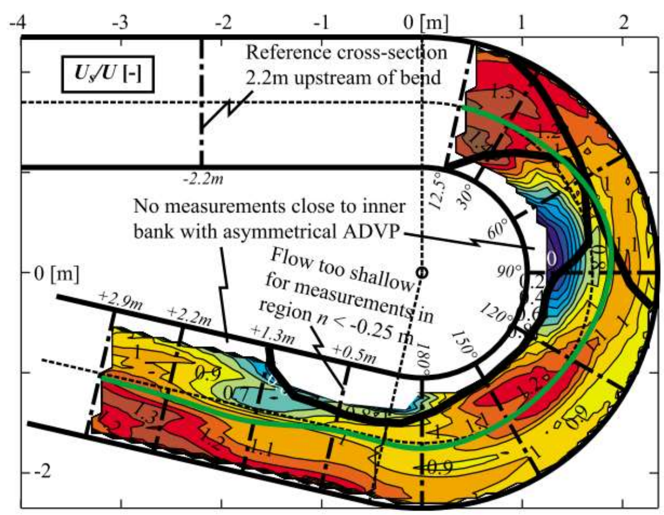

Figure 2.15: Normalized Depth-averaged Stream Velocity (U_S/U)

Besides horizontal circulation flow, 3-D flow structure including secondary flow are as well important in hydrodynamics. Values of normalized depth -averaged streamwise corticity ($< \omega_s > H/U$) and normalized depth-average vertical velocity (U_Z/U) are used to describe 3-D flow structure. Figure 2.16 shows the secondary flow's evolution by depth-average streamwise vorticity ($< \omega_s > H/U$) value. Evolution of secondary flow in a way of damped oscillation could be observed through Figure 2.15. comparing to the equilibrium value in the downstream part of the bend overshoot at about 60° has become more obvious which is 3 time higher. In addition, occurrence of secondary flow could be observed in the straight outflow and was well captured by Figure 2.16 below. According to Figure 2.17, the highest value of the normalized depth-averaged vertical velocity is at first half of the bend, which is around 0.3. With value of the normalized depth-averaged vertical velocity (vz,max/U ≈ ±0.05), it is also suggested that existence of curvature-induced secondary flow seem to be observed at downstream of the 120° cross section.

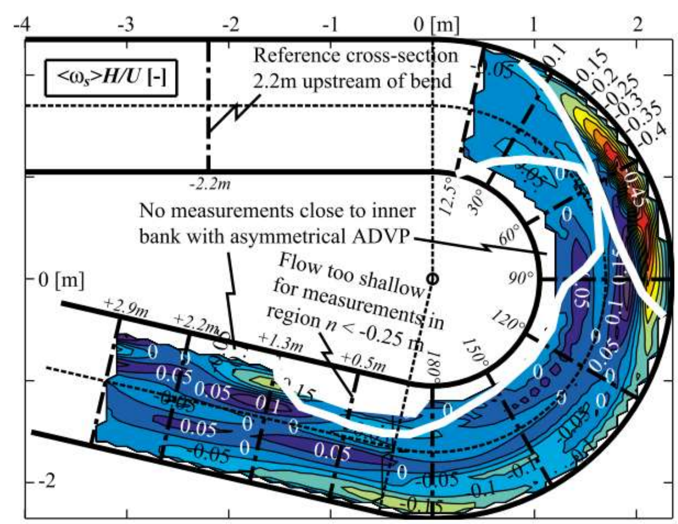

Figure 2.16: Normalized Depth – averaged Streamwise Vorticity ($< \boldsymbol{\omega_s} > \boldsymbol{H/U}$)

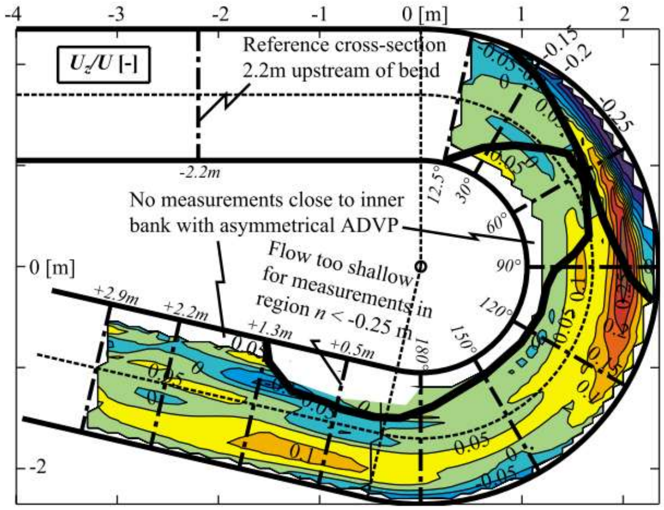

Figure 2.17: Normalized Depth-average Vertical Velocity (U_Z/U)

Another interesting value which is the normalized depth - averaged turbulent kinetic energy $(\mathrm{tke} >/(1/2\mathrm{u}_*^2))$ is used to describe turbulent activity. Turbulent activity is also key factor for transportation of sedimentation and mixing of matter such as oxygen, pollutants, heat, nutrients, and so on. The value of the normalized depth-averaged turbulent kinetic energy is depicted at Figure 2.18 below. According to the Figure, the maximum turbulent activity is not found in the deepest area of the bed. In which suggest that bed topography do not have significant influence on turbulent activity. Suggestion by (Blanckaert, 2010) that increasing of turbulent activity might be due to different physical process such as secondary flow. Intense turbulent activity could be seen at the bend from 30° to 90° of the cross section, this might be caused by the collision of the flow with the secondary flow. In addition, increase of turbulent activity also could be seen at downstream of the 120° cross section area which is the area when curve induced secondary flow occur. The occurrence of secondary flow could be observed in Figure 2.16 and Figure 2.17 above, this show some relationship with turbulent activity.

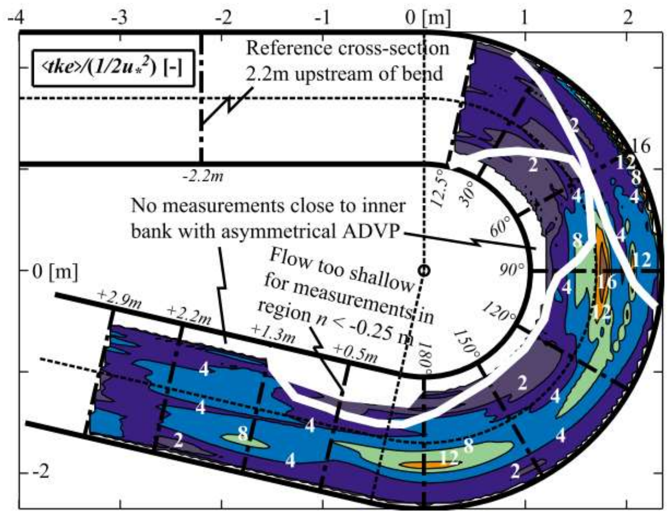

Figure 2.18: Isolines of Normalized Depth – average Turbulent Kinetic Energy $(< \mathbf{tke} >/(\mathbf{1}/\mathbf{2}\boldsymbol{u}_*^{\mathbf{2}}))$

2.5 Study of Vegetation in Meander River

There are studies such as Neph (1999), Termini (2017) and Tominaga et. Al. (1999) that show the effects of vegetation on the flow characteristics in curved and meandering channels. Vegetation plays an important role on bank stability and prevention of bank erosion (Termini, 2017), especially in high amplitude meander rivers, where streamwise velocity and bed shear stress are redistributed by the advective momentum which is transported by the cross-stream circulation. Furthermore, it also causes the bed topography to be reshaped which is known as topographic steering (Blanckeart & Graf, 2004). Besides the curvature-induced circulation cell observed in the centre region, counter-rotating circulation cells are often found in the upper part of the outer-bank region (Termini, 2017). The existence of the counter-rotating cells act as a buffer by maintaining the low level bank shear stress near the outer bank (Blanckaert and Garf, 2004). In addition, according to Termini (2017), existence of vegetation promotes the development of counter-rotating cell while at the same time suppresses the effect from in the central region cell. Therefore, it could be said that the existence of vegetation to some degree prevents the bank erosion by enhancing counter-rotating cell development which act as a buffer layer.

In order to create a simulation model of meander river with vegetation, understanding of effects that are caused by vegetation is important. There are several studies which investigate vegetation effects in meander rivers such as Termini (2017) and Tominaga et al. (1999). Moreover, several studies of numerical models for vegetation effects have also been done by Yang and Neph (2019) and Liu and Zeng (2017). Effects of vegetation on the river flow in meander river as well as their numerical model will be discussed in this section.

2.5.1 Laboratory Study of Vegetation Effect in Meander River

Several laboratory experiments were done by researchers to investigate the effect of vegetation in meandering river. In Termini's experiment, a flume with a centreline based on sine-generated curve was created as shown as Figure 2.19b. On the other hand, Figure 2.19c shows the setup of vegetation on the laboratory flume. The curvature of the flume has some similarity with Sungai Perak in Teluk Intan (Figure 2.19a), therefore comparison could be made.

In Termini's experiment, two runs were conducted including V-run and NV-run. V-run is the case with vegetation while NV-run is the case without vegetation. In V-Run, vegetation is arranged around the flume with density of 200 stems in 1m-2 and average height of 0.075m. Besides the difference of vegetation, other parameter such as flow rate, flume width, and etc. for both cases are the same. Table 2.4 below shows the parameters for both V-run and NV-run.

Table 2.4 Parameters for Both V-run and NV-run

Parameter	**Value**
Flow Discharge Q	0.012 m^3s^{-1}
Channel width B	0.50 m
Sand D_{50}	0.65 mm
Average flow depth h	0.052 m

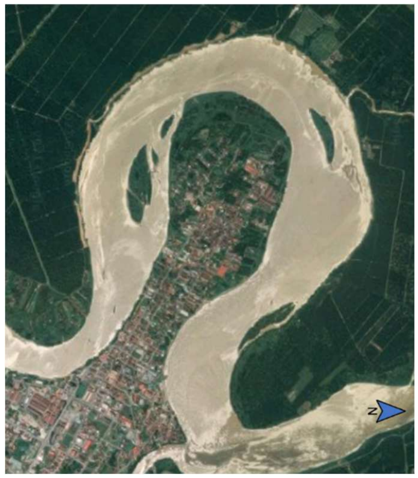

a. Top view of Perak River in Teluk Intan

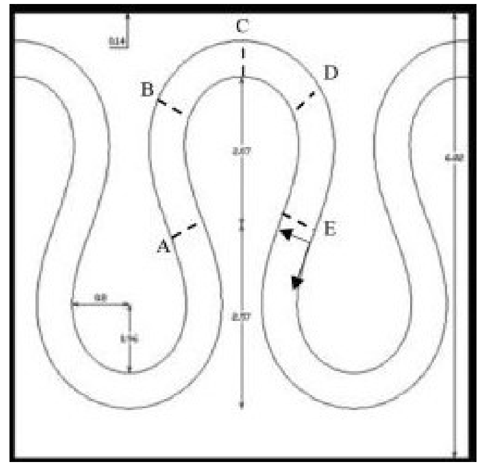

b. Laboratory Flume set up by Termini

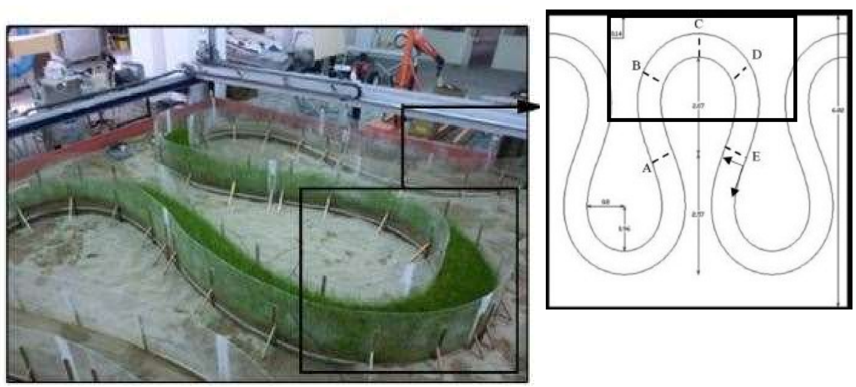

c. Laboratory Flume with Vegetation in Termini's Experiment

Figure 2.19: Top view of Perak River and Termini's laboratory Experiment Set Up

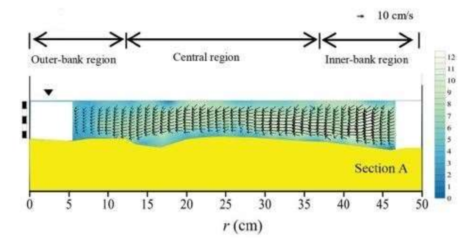

a. NV-run at Section A

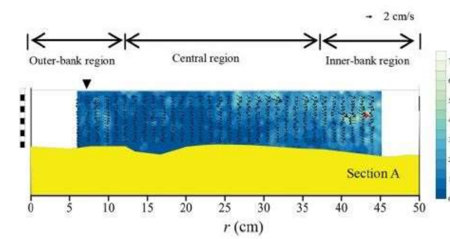

b. V-run at Section A

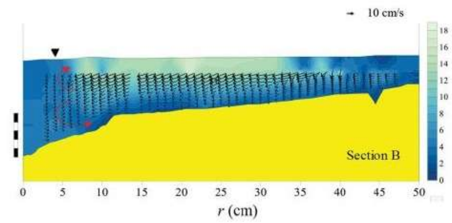

c NV-run at Section B

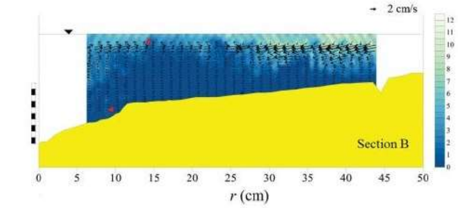

d. V-run at Section B

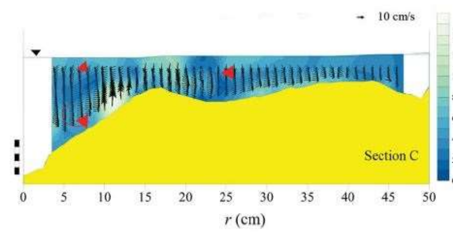

e. NV-run at Section C

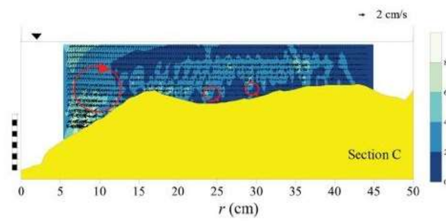

f. V-run at Section C

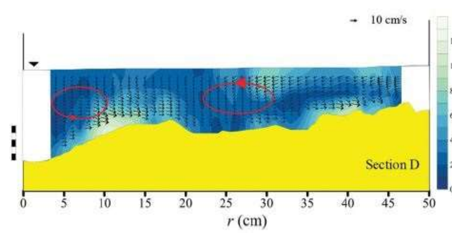

g. NV-run at Section D

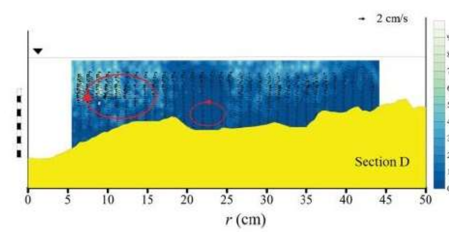

h. V-run at Section D

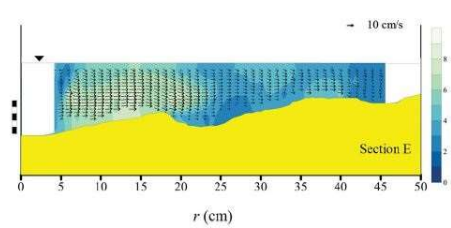

i. NV-run at Section E

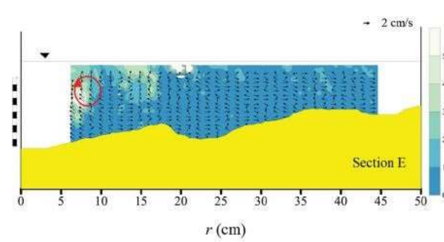

j. V-run at Section E

Figure 2.20: Mean Velocity V_t of NV-run and V-run at Different Section

Figure2.20 shows the results of Termini's experimental result. Each section is divided into three regions which are outer-bank region, central region, and inner bank region as shown in Figure 2.20a and Figure 2.20b. The color legend in the right-hand side of the figure shows the velocity magnitudes in cm s^{-1}, and the velocity vectors are shown by the arrows. Differences of the flow characteristic can be observed for both NV-run and V-run. First, the overall velocity magnitude from NV-run is greater than in V-run which can be seen from the color legend and the magnitude of the arrow. Secondly, the formation of counter-rotating cell is different for both cases especially in Section C as shown as Figure 2.20 e and Figure 2.20f. Although a counter-rotating cell also exists in NV-run near the outer bank, the counter-rotating cell in V-run is wider extended to such a degree that it strongly attenuates the activity of the central region cell. Moreover, the position of the core of high velocities are different in both cases. This phenomenon can be observed in Figure 2.21. In Figure 2.21a and Figure 2.21b, it is obvious that the core of high velocities from NV-run is closer to the outer bank region compared to V-run. On the contrary, the core of high velocities tends to shift inward and keeps some distance away from the outer-bank when there is the vegetation.

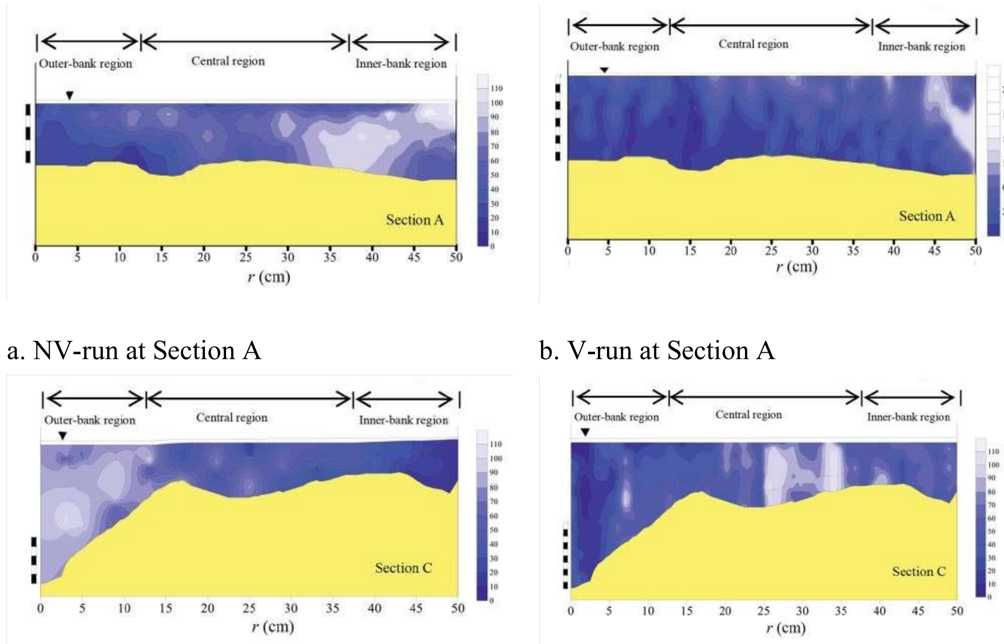

a. NV-run at Section A b. V-run at Section A

c. NV-run at Section C d. V-run at Section C

Figure 2.21 Distribution of the Streamwise Flow Velocity

2.5.2 Numerical Model of Vegetation Effect

In order to describe vegetation effect in a river flow, numerical models were developed and tested by Nepfh (1999). The models depict some physical properties of the interaction between the vegetation and the river flow such as the drag force, the turbulence, and the diffusion. Laboratory experiments and field tests were conducted, and the results were used to compare with the numerical models. The drag model for emergent vegetation is shown in equation (2.1). The vegetation in Neph's experiment is treated by cylinders, and the effect of stem morphology and flexibility are neglected to avoid complication (Neph,1999). In equation (2.1), FT is the drag force, $\overline{C_D}$ is the bulk drag coefficient, a is the density of vegetation per meter, and U is the velocity.

$$F_T = \frac{1}{2}\overline{C_D}aU^2 \tag{2.1}$$

Vegetation density can be determined using equation (2.2). Since the vegetation is treated as a cylinder as mentioned before, the number of the cylinder per unit area, the mean spacing between cylinders, diameter of the cylinder are denoted by n, S, and d, respectively while h is the flow depth. In addition, dimensionless population density (ad) is defined by equation (2.3) below which also represents the fractional volume of the flow domain occupied by plants.

$$a = nd = \frac{dh}{\Delta S^2 h} = \frac{d}{\Delta S^2} \tag{2.2}$$

$$ad = \frac{d^2}{\Delta S^2} \tag{2.3}$$

Regarding the bulk drag coefficient CD, the generation of the wake can suppress the CD. Whereby, it could be explained by Figure 2.22 below which show contours of drag coefficient of cylinders under a constant velocity U. The contours in Figure 2.22 are measured using the data of two cylinders A and B which

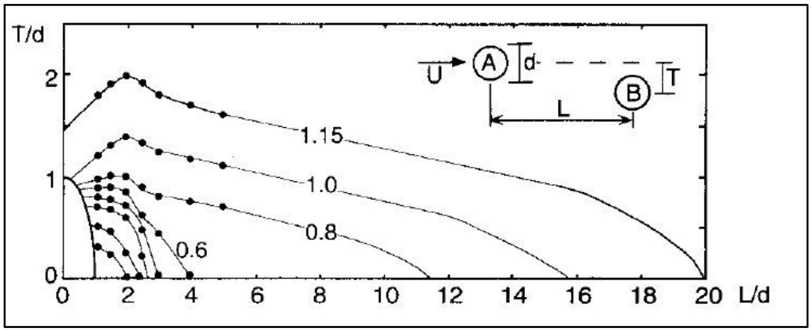

Figure 2.22 Counters of Drag Coefficient

are shown in the top right corner of the figure. T/d and L/d in Figure 2.22 are the lateral spacing and longitudinal spacing between the 2 cylinders, respectively. It can be concluded that from Figure 2.22 that the drag coefficient decreases as T/d and L/d decrease. This is due to the wake generation effects of cylinder A which suppress the drag coefficient of the trailing cylinder B making the CD value to be decreased.

The turbulent intensity within emergent vegetation is derived from production of turbulence within stem wakes, P_w which is estimated by the work input $F_T U$. F_T is mentioned previously in equation 2.1. Therefore, after substituting equation 2.1, P_w can be determined using equation 2.4 below:

$$P_w = \frac{1}{2}\overline{C_D} a U^3 \quad (2.4)$$

According to Neph (1999) turbulent kinetic energy budget is reduced to a balance between wake production Pw and the viscous dissipation ε which is $P_w \sim \varepsilon$, due to the assumption of homogeneity. Through assuming the characteristic length scale of the turbulence is set by the stem geometry d, viscous dissipation is scaled as equation (2.5)

$$\varepsilon \sim k^{\frac{3}{2}} d^{-1} \tag{2.5}$$

Where the turbulent kinetic energy per unit mass is denoted by k. The ratio of the turbulent intensity to the mean velosity $\frac{\sqrt{k}}{U}$ is givrn by equation (2.6) determined by substituting equation (2.5) in equation (2.4). $\alpha_1$in equation (2.6) is a scale coefficient.

$$\frac{\sqrt{k}}{U} = \alpha_1 [\overline{C_D} a d]^{\frac{1}{3}} \tag{2.6}$$

The net diffusion *D* within a cylinder array is determined through summation of two processes which are the turbulent and mechanical diffusion process. Equation (2.7) shows the turbulent diffusivity D_t:

$$D_t = \alpha_2 \sqrt{kd} \tag{2.7}$$

From equation (2.7), α_2 is the scale factor and will differ depending on horizontal and vertical diffusion since the array diffusivity is not isotropic. Mechanical diffusion Dm on the other hand, is shown by equation (2.8) below:

$$D_m = \frac{\beta^2}{2} [ad] U d \tag{2.8}$$

Since the processes of mechanical and turbulent diffusion vary and they are independence, their contribution to the total diffusivity will be additive. Therefore, the total horizontal diffusivity D is the sum of equation (2.6) and equation (2.8) which is shown as equation (2.9)

$$\frac{D}{Ud} = \alpha[\overline{C_D}ad]^{\frac{1}{3}} + \left[\frac{\beta^2}{2}\right]ad \qquad (2.9)$$

In equation (2.9), the total horizontal diffusivity D is nondimensionalized using the mean velocity U and the cylinder diameter d. Moreover, the scale factor α from equation (2.2) are the combination of scale factor α_1 and α_2 from equation (2.6) and equation (2.7), respectively.

In Nepf's study, laboratory experiment and filed survey were conducted and the results such as bulk drag coefficient $\overline{C_D}$, diffusivity *D,* etc. were used to compare with the numeric model. Set up of the laboratory experiment is shown as Figure 2.33 below. The model area is 5m which wooden cylinder arrays with density between a = 1.2 and 10.5 (200 – 2000 stems/m-2) were mounted randomly by using a numerical program. The 5m model was fit into a recirculation flume with a length of 24m. Base of the board was extended 3m upstream in order to prevent flow disruption. In addition, a section of rubberized fibre mat with 0.5m is used to stabilize the flow before entering the model. Velocity components of (u,v,w) were measured by an Acoustic Doppler Velocimeter (ADV) and a Laser Doppler Velocimeter (LDV). In order to

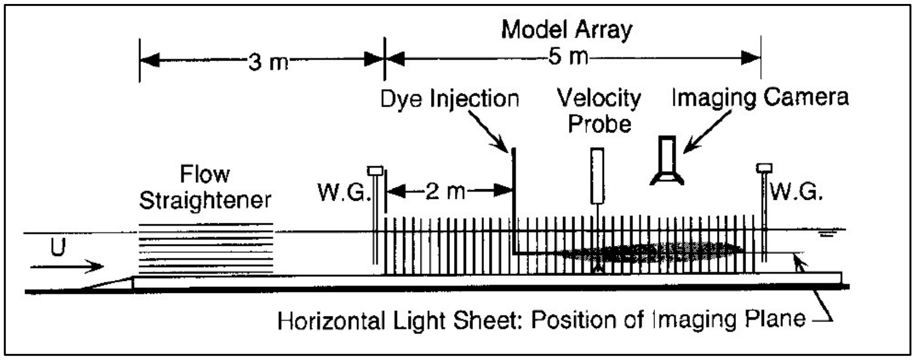

Figure 2.23 Laboratory Experiment Set Up in Nepf's study

determine the diffusivity, a plume of dye was released steadily and continuously at the mid depth and the mid width position of the model array region. A video image of the plume was recorded and transferred to an image analysis software.

On the other hand, field survey was conducted in Great Sippewisset Marsh which covered by *Spartina alterniflora* which is a kind of smooth cord grass. The grass have cylinder like morphology and have little bending movement under normal tidal which i considered ideal for the numerical model discussed in previously. Different stem density values *n* including 96, 196, and 370 stems in m^2 were adjusted by pruning process. Similar dye plume technique which is done in Laboratory experiment was used in the field experiment to measure diffusivity. The field experiment setting is shown as Figure 2.24 below. As shown as Figure 2.24 below, the dye injection table was arranged perpendicular to the flow to prevent interference to the flow. Dye was released at an ambient flow speed with a variable-speed pump at mid depth by a ¼ inch "L" tube. At a distance of 1.5m downstream from the dye injection table, fluorometer was set up in order to record the plume concentration continuously.

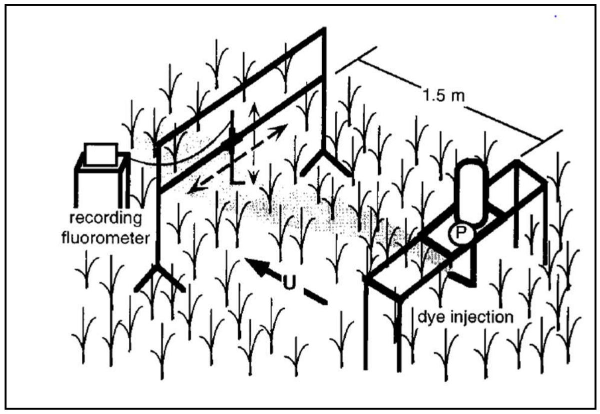

Figure 2.24: Field Experiment Set Up in Nepf's Study

Results of the dimensionless diffusivity of numerical model, laboratory observation, and field observation are shown in Figure 2.25 below. In Figure 2.25 below, 3 different lines which are the solid line, dash-dotted line, dash line represent the numeric models. Whereby, total diffusion is shown by solid line, turbulent diffusion is shown by dash-dotted line, and mechanical diffusion is shown by dash line. Turbulent diffusion (dash-dotted line) is obtained through equation 2.6 and equation 2.7 while mechanical diffusion (dash line) is obtained through equation 2.8. On the other hand, the results obtain from laboratory experiment and field experiment are shown by circle and triangle icon respectively. Moreover, two different wake regimes were used in the laboratory experiment, which are Re_d = 400-2000 (shown by open circles) and Re_d = 60-90 (shown by solid circles). Scale factor including α_1 and α_2 are both 0.9 which are based on the observation during the experiment while scale factor β = 1 is based on assumption.

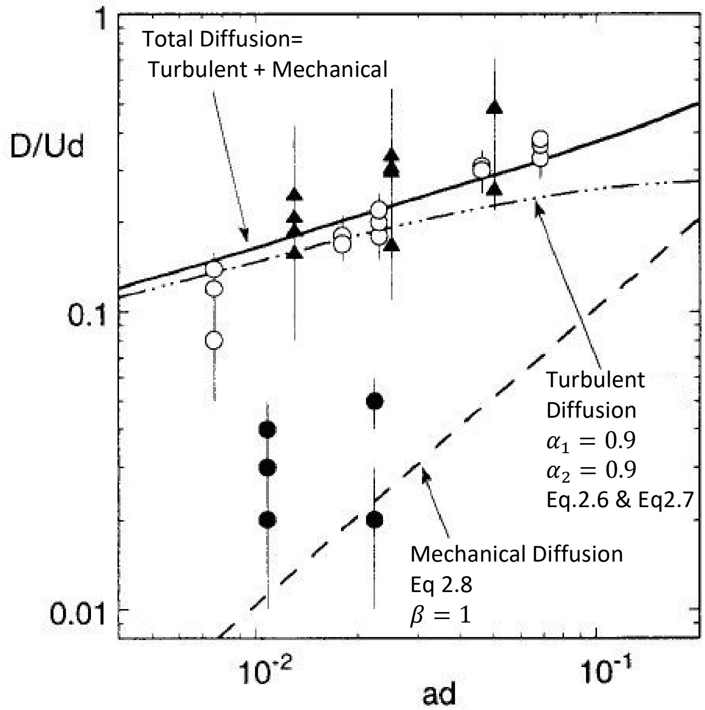

Figure 2.25 Results of Dimensionless Diffusivity of Numerical Model, Laboratory Experiment, and Field Experiment

From Figure 2.25, it could be seen that results of the regimes Re_d = 60-90 (solid circle) do not fit the total diffusion quite well. Explained by (Nepf, 1999) that it might be due to the bed-generated turbulence. Despite of the fact that Re_d =60-90 does not match the numeric model well, the other regimes which is Re_d = 400-2000 from laboratory experiment (open circles) seems to fit the model quite well. Result of field survey with Re_d=300-600 which conducted in Sippewisset Marsh are shown by the triangles in Figure 2.25 above. It is shown that the results in field survey is consistence with both the numerical model and laboratory experiment. Whereby, the diffusion in the field survey increases with vegetation density in a way that it matches the numeric model well which suggest that the numerical model from this study can be used to describe vegetation effects.

2.6 LES Methods for Curved Open Channel Flows

It can be said that the characteristic of a natural river flow is an open channel flow with large width to depth ratio which has high Reynolds number. (Balen et al., 2010) The topography of the river bed will change as a result of interaction between movement of the flow and the river bed.

Downscaling of river flow to laboratory dimension is often being made so that complex flow type can be studied and investigated in several aspects in a manner of optimized and controlled conditions (Balen et al., 2010). LES was set up by Balen in order to have better insight. The purpose of the set up for the LES module is to determine the strongly curved open channel flow over topography's three-dimensional flow, to find out differences of the performance between LES and RANS method, and structure of turbulent model in respect to its boundary shear stress, kinetic energy, and anisotropy. Moreover dominant mechanisms regarding to transport of momentum also being considered (Balen et al., 2010).

The LES method was set up based on Blankceart's work, and was mentioned in the previous section in 2.4.1. Moreover, the meandering curve model in LES are rather the same with Blankcaert's experiment whereby both of the maximum bend are 193°. The physical domain of the curve are listed in table 2.5 below and the LES model are shown as Figure 2.26 below. In Blanckeart's experiment, straight inflow and straight outflow are set to be 9m and 5m respectively. However, in Balen's LES model, both inflow and outflow are set to be 3.8m due to the consideration of computational cost.

Table 2.5: Physical Domain of Meandering Curve in LES Setting

Discharge (Q)	Mean water depth (H)	Width of the Flume (B)	Bulk Velocity (V_{av})
89Ls^{-1}	0.141 m	1.3 m	0.49 ms^{-1}

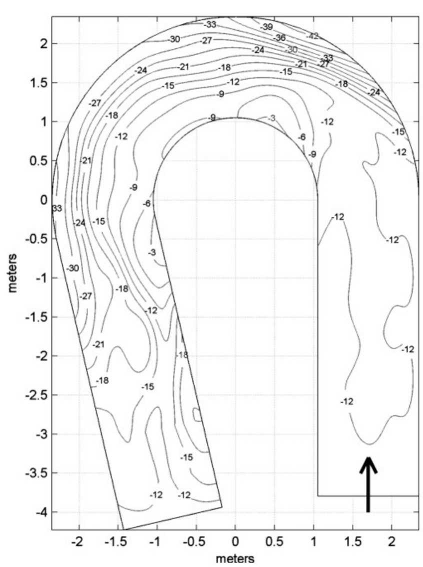

Figure 2.26: Meander curve of Balens's LES model (Bed topography are shown in height (cm) by the isolines using water level as reference.)

Finite Volume model was used as numerical model for this LES simulation. With the usage of midpoint rule, Integrations of incompressible Navier-Stokes equations are numerically done. In addition, the computation of the Navier-Stokes equation was based on structured, regular, and staggered grid within pressure-correction algorithm. Cylindrical reference system was used and by which r, θ, and z are used to represent transverse, streamwise, and vertical direction respectively. Associated velocity vector are denote by u,v, and w accordingly. The cylindrical reference system is shown as Figure 2.27 a below. Navier-Stokes equations are solved within the cylindrical coordinate, which is filtered by top hat filter that is as width as the grid spacing. Meanwhile, the cylindrical reference system can be converted into Cartesian coordinates, which are used in straight part of the geometry. This is done by letting $1/R \rightarrow 0$. The Cartesian coordinates system are shown in Figure 2.27b below.

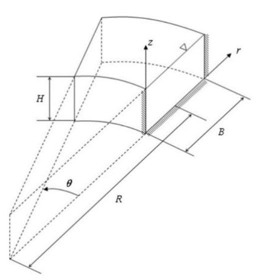

a) Cylindrical Reference System with R as the radius at the channel axis

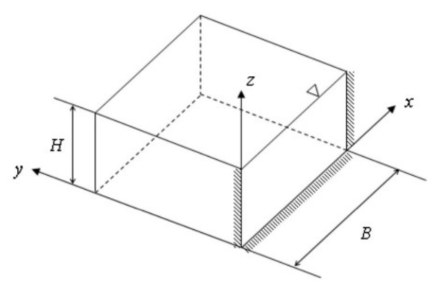

b) Cartesian coordinate system. B as the width and H as the height of the channel.

Figure 2.27: Reference system in Balens's LES model

For the boundary condition, where the free-slip condition is being applied, a horizontal, impermeable rigid lid is used to handle the free surface. (Balen et.al, 2010). This approach of treating free surface is often used in straight open channel flow as well as curved open channel flow. In spite of that, continuity error might occur in this approach. However according to (Demuren and Rodi, 1986), the error will remain small with the free surface's superelevation less than 10% of the channel depth, hence more likely to be the case in Balen's experiment. Implementation of Fictitious bed topography was done to minimize the continuity error. Wall function approach is used to tread the solid walls. Standard law of the wall method is used for the hydraulically smooth vertical site wall, in which the mathematical expression for viscous layer, buffer layer, and logarithm layer are shown as the equation 2.10 below respectively:

$$v_n^+ = z_n^+ \quad \text{if} \quad z_n^+ \leq 5$$

$$v_n^+ = 5.0 \ln z_n^+ - 3.05 \quad \text{if} \quad 5 < z_n^+ < 30 \qquad (2.10)$$

$$v_n^+ = 2.5 \ln z_n^+ + 5.5 \quad \text{if} \quad z_n^+ \geq 30$$

Wall normal velocity is represented by v_n^+, while z_n^+ represent the coordinate. On the other hand, when dealing with hydraulic rough bed, another equation is used which is the modified log law according to (Vardy, 1990). The mathematical expression are shown as equation 2.11 below:

$$v_n^+ = 2.5 \ln \frac{z_n^+}{k_s} + 8.5 \qquad (2.11)$$

Whereby k_s represent roughness height. Before the real simulation was run, another LES run was done separately as straight open channel over the inflow topography, in order to specify inflow boundary condition. Two additional simulation runs were conducted to investigate the sensitivity from the effect of the roughness height on the simulation result. The only difference for these runs is the roughness height value. Whereby the k_s in run A, run B, and run C are 0.037m, linearly varying from 0.006 to 0.037 and 0.006 respectively. Other than that, hydraulic condition remains the same as shown in Table 2.6. The flow rate, average velocity, mean water depth, width of the channel, roughness height, and Reynold number are represented by Q, V_{av}, H, B, k_s, and Re respectively.

Table 2.6: Hydraulic Condition of Three Simulation Run

RUN	Q (ls^{-1})	Vav (ms^{-1})	H (m)	B (m)	k_s (m)	Re
A	89	0.49	0.141	1.3	0.037	68000
B	89	0.49	0.141	1.3	$0.006 - 0.037$	68000
C	89	0.49	0.141	1.3	0.006	68000

Among all the runs aforementioned, numbers of the computational grid cell are the same which is 1248 ×192×72. With total 72 cells, distribute vertically over total high that is 0.4293m, resulting in a regular grid resolution of 6mm. However, according to (Balen et.al,2010) the resolution of it are still not refine enough for direct representation of the ripples. Since regular grid are used, there is a problem of handling non-grid confirming bed. Therefore, a modified version of the immerse boundary technique is used in Balen's simulation which was proposed by Balaras. Briefly, the concept of Balaras is subdivide into the entire computational domain into fluid region and solid region. Whereby, the bed region is solid region while the area above the bed is fluid region. At least one velocity point that is located at the fluid region adjacent to the bed region are marked as boundary points (Balaras, 2004).

In order for the flow characteristic in the bend to be shown, snapshot of the cross-section of run A's streamwise velocity were taken at the bend 0°, 21°, 43°, 64°, 86°, 107°, 129°, 150°, 172°, and 193 snapshots of which are taken. Overall view of the snapshots are shown in Figure 2.28 below. The asterisk at the entrance part shown in Figure 2.28 represent particles that are released and their trajectories are shown by the line. On the other hand, flow direction is shown by the arrow.

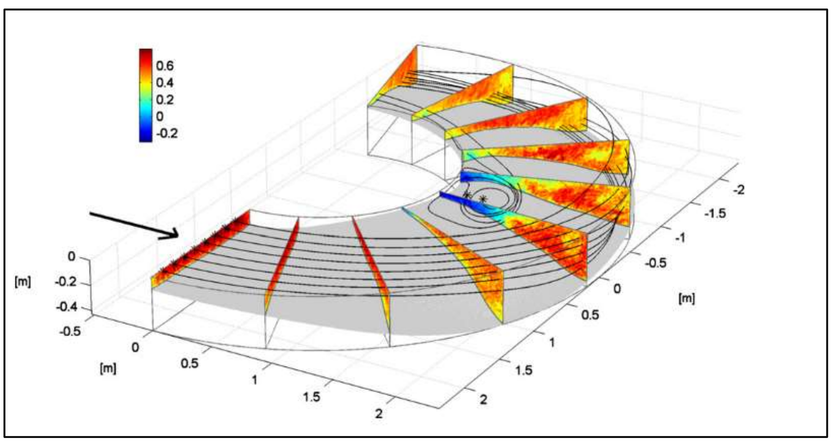

Figure 2.28: Snapshot of RUN A's Turbulent Streamwise Velocity from at Several Cross Section

By observing the particles trajectories from Figure 2.28, it is clear that there is a horizontal recirculating zone near the inner bank at the cross section region of 90°. In addition, back flow could be seen in this area, which suggest that it is associated with the recirculation zone. These phenomena quite coincide with Blanckaert's experiment, which was mentioned at section 2.4.1. As for the streamwise velocity, it is skewed toward the inner bank at the bend entry. According to (Balen et.al,2010), it is due to the favourable longitudinal pressure gradient caused by discontinuity in curvature. Flow decelerates at the upstream part of the bend due to the increase of depth. However, due to the influence of the recirculation flow and the curvature induced effects, flow recover in the downstream part of the bend which is after about 110°of cross section

Furthermore, in order to have deeper understanding regarding the flow characteristic around the bend, several Figures were illustrated including Figure 2.29 and Figure 2.30. Figure 2.29 was depicted showing the streamwise velocity's pattern at cross section of 30°, 60°, 90°, 120°,150°, and 180°, while Figure 2.30 shows vorticity and two - dimensional divergence for RUN A.

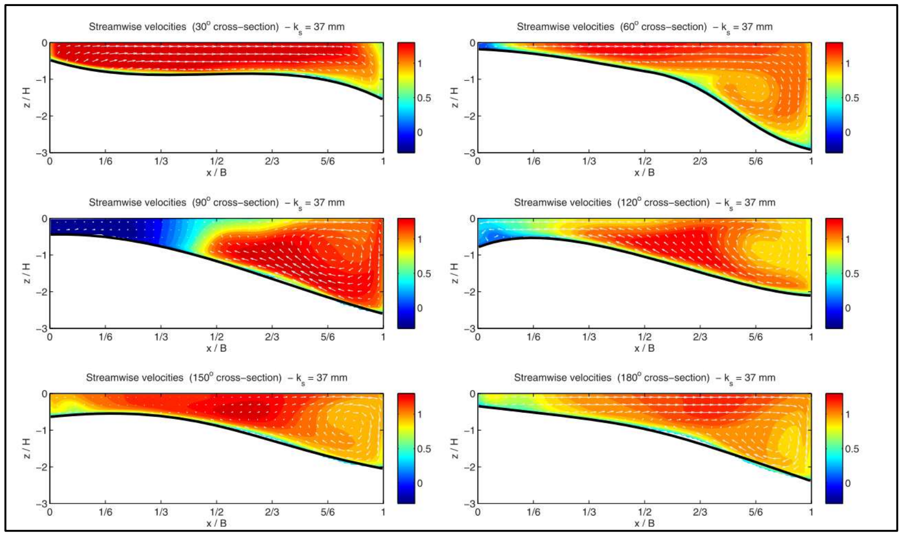

Figure 2.29: Streamwise Velocity Pattern at 30°, 60°, 90°, 120°,150°, and 180°

At the background of each cross section from Figure 2.29 above, velocity vector was represented by the inserted arrow in a ratio of one out of five grid cells. Streamwise velocity's value were made dimensionless with the bulk velocity V_{av}. According to Figure 2.28 above, recirculation zone could be seen at 90° cross section. Strong spatial flow development is shown in the cross section of 30° and 60° while at bend's downstream part, mild flow evolution develops at cross section of 120°, 150°, and 180°.

Moreover, vorticity ω_z and two-dimensional divergence D_z are shown as Figure 2.30 below. Both the values are determined by equation 2.12 below, mean water depth H and bulk velocity V_{av} are used to nondimensionalize both the vorticity ω_z and two-dimensional divergence D_z.

$$\omega_{z=}\frac{1}{r}\frac{\partial U}{\partial \theta}-\frac{1}{\mathrm{r}}\frac{\partial V_r}{\partial r} \quad , \quad D_z=\frac{1}{r}\frac{\partial U_r}{\partial r}+\frac{1}{\mathrm{r}}\frac{\partial V}{\partial \theta} \qquad (2.12)$$

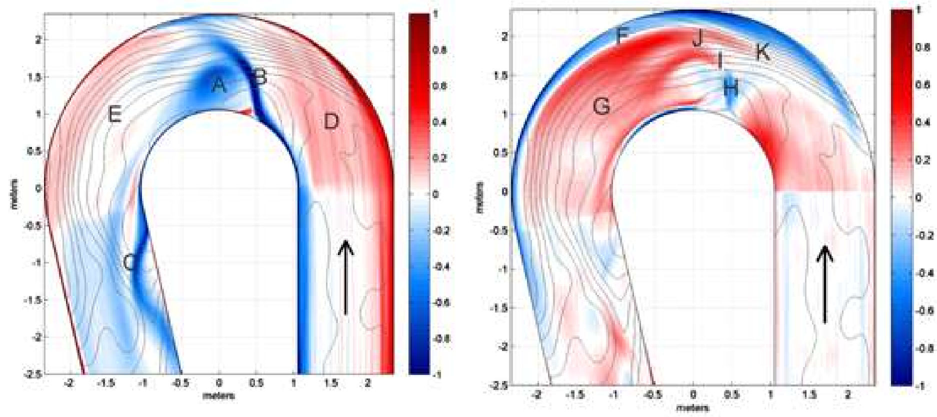

a. Vertical vorticity b. Two-dimensional divergence

Figure 2.30: Time - averaged Velocity Field from RUN A at the Free Surface

While movement at the free surface are elaborated by means of the value of ω_z, upwelling or down welling movement could be represented by two-dimensional divergence value D_z . From Figure 2.30, it is obvious that discontinuity is reflected at both panels of the Figure in both the entrance of the curvature and the exit of the curvature. This is due to the additional cylindrical term, which suggests that rather than numerical artifact, this is a physical phenomenon. Alphabet from letter A to letter G is used among two panels to denote flow development and characteristic of each region. In the left panel of Figure 2.30, letter A is marked to show the recirculation zone. The region could be identified as counter clockwise rotating fluid circular zone with a diameter around 0.5m at free surface. In addition, boundary layer could be seen at the straight inflow reach at left panel of Figure 2.30. The boundary layer detached at the region of the highest part of the point bar. Curvature of the main flow caused the mixing layer (which mark as letter B) to be developed spatially in this region. From the Figure 2.23b, the mixing region are denoted by letter H, J., and I beside region B, flow separation could be seen as well at point C, which is 0.5 downstream from bend exit. However, associated recirculation zone in this region is seemingly very weak. In region D, flow are shown to be strong spatially adapted to the curvature of the bend. With the value of vertical vorticity $\omega_z > 0$, flow of the free surface in region D is suggested to rotate in clockwise direction. Meanwhile by contrast, flow in region E seem to be more still since the value of ω_z is almost zero.

Furthermore, in Figure 2.23b, upwelling motion are express by $D_z > 0$, while $D_z < 0$ is the downwelling motion. In region F, the downwelling motion occur near outer bank where the flow dives toward to bottom as expected. Whereas, large region of upwelling movement occurs in region G. Moreover, three dimensional flow behaviour are perfectly presented at the recirculation zone where both downwelling and upwelling happen. This could be interoperated by superimpose of both the secondary flow in horizontal plane and cross-sectional plane which is induced by centripetal force. While downwelling motion is present in region H, upwelling motion is occurring in the region including I,J, and K.

Components of the velocity vector including streamwise velocity, transverse velocity, and vertical velocity in cross section of 90° are compared between simulation outcome of RUN A and experimental result. All of the values of the streamwise velocity are nondimensionalized using the bulk velocity

V_{av}.The comparison are shown as Figure 2.31 below. Experiment result is shown in the left panel of Figure 2.31, while right panel shows the simulation result. Streawise velocities, transverse velocities, and vertical velocities are shown accordingly from top to bottom. However, it should be noted that in conducting of the laboratory experiment, due to the fact that the depth of the region at x/B<1/3 was too shallow, measurement of ADVP might not be accurate. Regarding to the top panel from Figure 2.31 which is the streamwise velocities, it reveals that maximum of the streamwise velocities is 1.3 V_{av} which is found at 90° cross section around the pool region near the bottom. The result from the Figure 2.31 shows the similarity of the streamwise velocity between experiment and simulation are seemingly high.

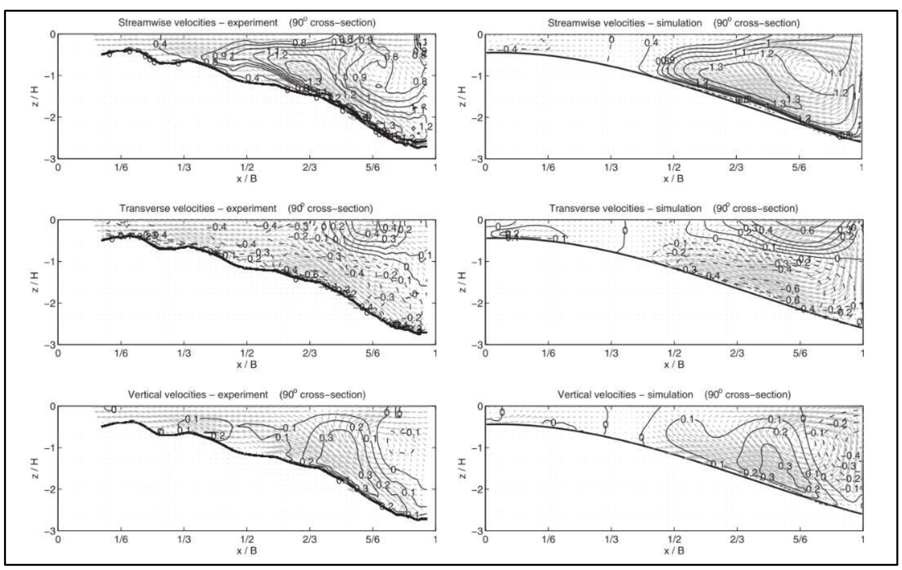

Figure 2.31: Three Velocity Components which are Streamwise Velocities, Transverse Velocities, and Vertical Velocities are Being Compared at Cross Section of 90°

Despite the similarity, there are still some disagreements. In the bottom panel, which shows vertical velocity at Figure 2.31 above, differences could be observed at the outer bank region. Simulation result shows a stronger down welling motion, which is about 0.4 V_{av} while experimental result shows 0.1 V_{av}. In addition, value of the streamwise velocity at the outer bank in the experiment is 0.8 V_{av} whereas in the simulation, the value is 1.1 V_{av}. According to (Balen et.al,2010), there is still some kind of spatial lag between experiment and simulation. In addition, the spatial lag which is only present in experiment might be caused by the bed ripples, seems to cause the development of flow throughout the bend to be delayed. Although the bed ripples do not appear in the simulation, bed topography could reflect on the flow development and could be observed in Figure 2.31. In the right-hand side of middle panel from Figure 2.31, which shows the transverse velocity, outward directed flow and inward directed flow was seemingly separated by a line. As a matter of fact, the line could be described as being in correspondence with the location where the ending of the point bars, and the starting of the pool.

Besides the comparison between simulation and experiment, numeric method, which is the RANS method, is being compared as shown as Figure 2.32 below. The results from the RANS method which are used for comparison are taken from (Zeng *et al.*, 2008). In Figure 2.32, results from experiment, LES, and RANS are being compared by means of sreamwise velocities and transverse velocities at the cross section of 30°,60°,120°, and 180°. They are represented by circle dot, solid lines, and dashed lines respectively.

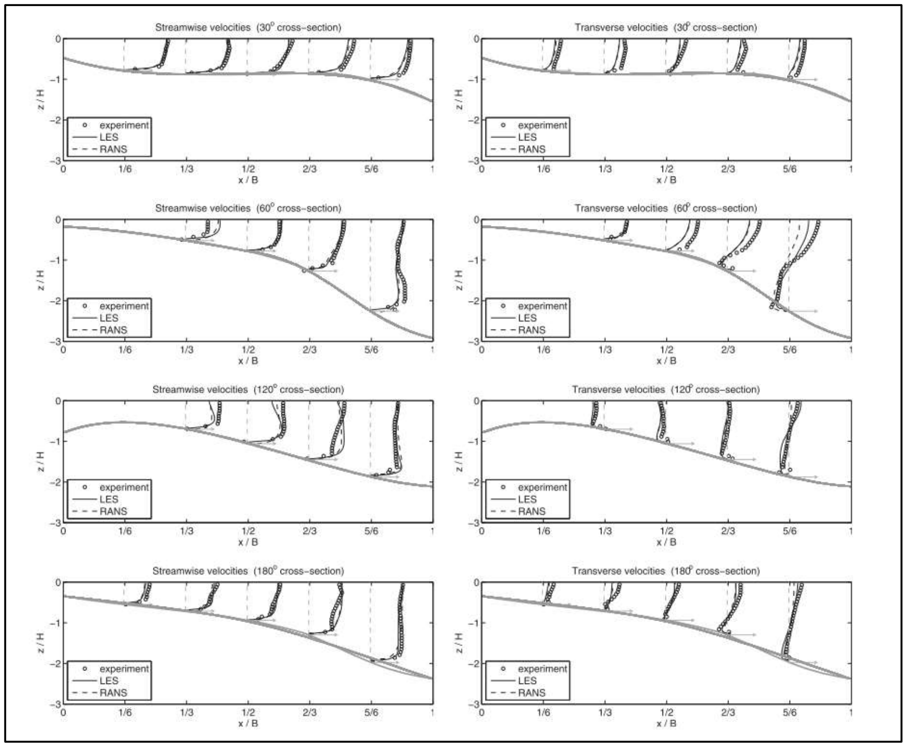

Figure 2.32: Comparison of the Result from LES, RANS, and Experiment at Cross Section of 30°, 60°, 120°, and 180°

From Figure 2.232 above, it could have seen that similarity between LES result and experiment result varies. In some location they coincide perfectly, whereas in other location they might be discrepancy. Despite the moderate quantity agreement, qualitative agreement between result of LES and experiment is rather good. Likewise, comparison between LES and RANS is almost the same case. Overall, the concurrence between LES and RANS is quite well. However, the only location where three approaches diverge is from the transverse velocities profile at cross section of 60° and could be seen at the region x/B=5/6. Furthermore, missing of RANS result at $x/B = 1/2$, and $x/B =$

2/3 is due to the collapsed of the approach in this region. As speculated by (Balen et.al,2010), the reason of the divergence might be due to existence of small-scale dunes. Despite the dense measuring grid, both the LES and RANS still not able to resolve the small-scale dunes sufficiently. As a result, the causing the flow development to be spatially delaying by the small-scale dune might not be well represented for these two approaches.

As mentioned in the previous content, in order to determine the degree of influence of roughness height to the overall result, three parallel simulation runs have been conducted with different roughness height. The hydraulic conditions are mentioned previously in table 2.5. After the results of these RUN been obtained, they have been illustrated in Figure 2.34 below by means of streamwise vorticity, which is nondimensionalize by the bulk velocity V_{av} and the mean water depth H. In Figure 2.34, streamwise vorticity profile of Run A, B, and C are shown accordingly from top to bottom, moreover their location is at the cross-section of 90°. In addition. Figure 2.33 shows the result from experiment, which is used to compare the simulation result.

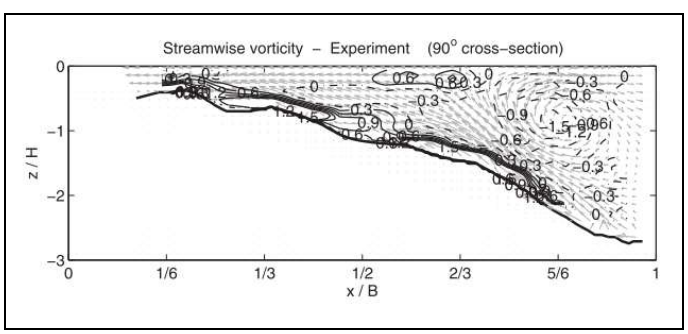

Figure 2.33: Result from Experiment at Cross Section of 90°

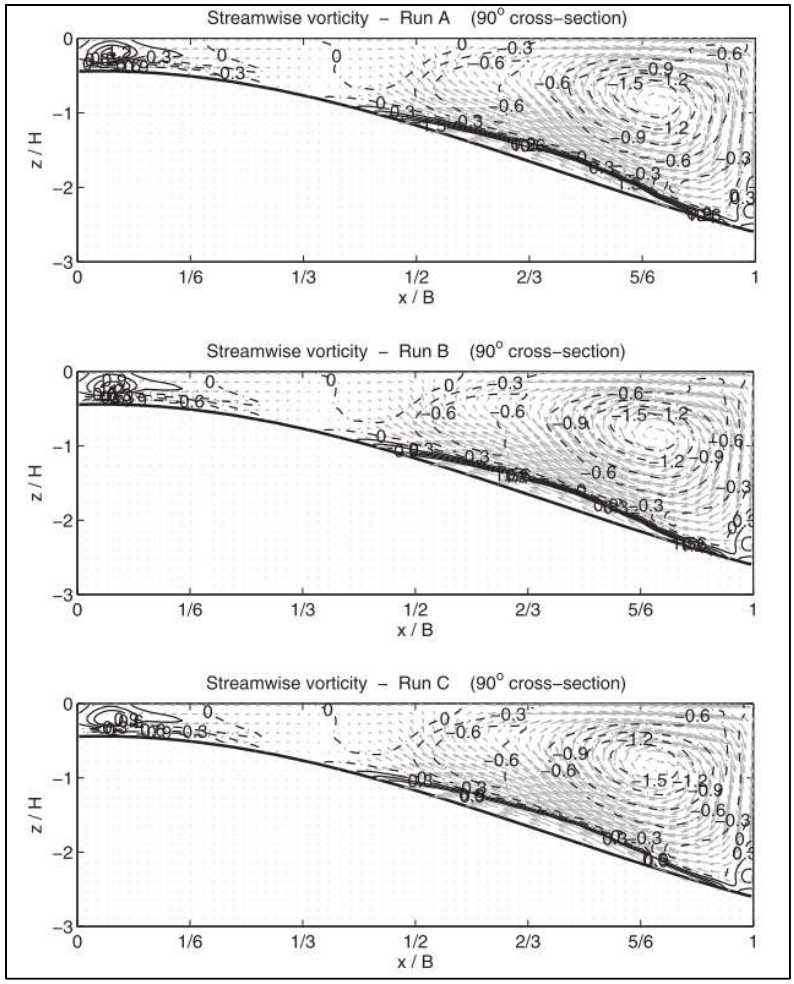

Figure 2.34: Result from Simulation run A, B, and C at Cross Section of 90°

In Figure 2.34, clear minimum value of -1.5 from the experiment could be observed in Run A and Run B, however in Run C it has been seen to be less significant. In addition, the tendency of the minimum value moves a little to interbank with decrease bed roughness is noticeable. There is a disagreement regarding to cross-sectional flow's rotational structure between the experimental result and simulation result, located near inner bank. In this location from the experiment, the flow is pointed toward inner bank, while flow is pointed toward outer bank in all simulation runs. Therefore, the sign of streamwise vorticity is the opposite. Since the 90° cross section is located near centre of the recirculation zone, this discrepancy can be understood, small streamwise oriented changes in the location can easily cause changes to the secondary flow (Balen et.al,2010). Furthermore, difference of recirculation zone size can also be observed among three simulation run. Whereby, Run C has the largest recirculation zone that is around 10% larger than Run C. Therefore, it could be concluded that increment of the recirculation zone is likely to be caused by decreasing roughness of the bed.

Besides that, the strength of the secondary flow has also been investigated and is shown in Figure 2.35 below. The secondary flow is resembled by equation of stream function ψ, which is shown as equation 2.13 below.

$$\psi = \frac{1}{2}\int_{r_i}^{r} Wrdr + \frac{1}{2}\int_{z_b}^{z} -Urdz \qquad (2.13)$$

Time-averaged transverse and vertical velocities are described by U and W respectively from equation 2.13 above. While the vertical coordinate of the bottom and the curvature radius at the inner bank are represented by z_b and r_i accordingly.

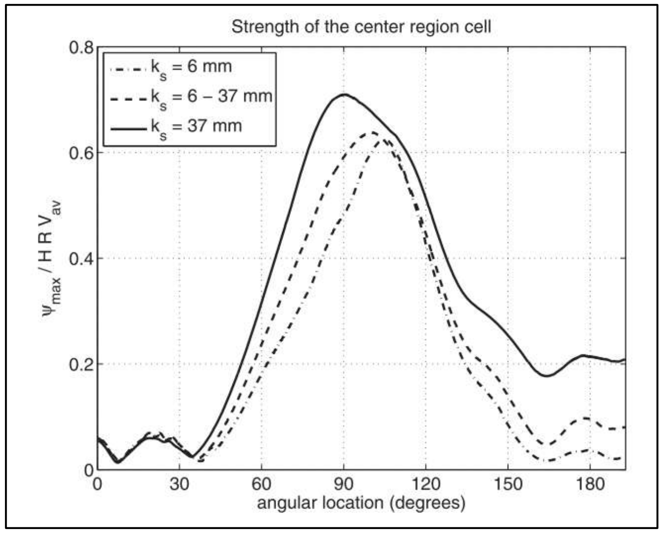

Figure 2.35: Strength of the Secondary Flow from Simulation run A, B, and C

It could be observed that Run A with roughness height value of k_S=37mm, has the highest value of max ψ. In contrary, Run C with value of k_S =6mm has the lowest value of max ψ. Therefore, conclusion can be made that strength of secondary flow increases along with the increase of roughness height value k_S. Moreover, strength of secondary flow from all simulation run increases monotonically from 35° and reaches the peak at somewhere around half the bend. In addition, the peak has the tendency to move downstream along with the decrease of roughness height k_S. This could be explained that roughness height k_S decrease along with the increase of the dimension of the recirculation zone However, (Balen et.al,2010) emphasize that value of ψ is sensitive and have enlarged effect during integration process. Therefore, the difference value of ψ for three simulation run should not be overstated.

2.7 KULES method

The LES method used in this report is the KULES method, which is developed by the faculty and student of Civil Engineering Department of Kobe University. Although there are currently commercial or even open source CFD software packages available in the market, a well-developed LES has yet to been seen. This is due to the methods that are suitable for LES are not always the same; moreover, results are dependent on grid, numerical methods, and the interpretation (Nakayama, 2012) . In order to develop a LES simulation methodology to solve problem of group of flows encounter by civil engineers in natural streams, constructed channel, and coastal region, efforts had been put forward by Civil Engineering Department of Kobe University over several years (Nakayama, 2012). The distinguishing features of KULES is that it is adaptive to various flow situation with the construction of rectangular mesh. There are pro and cons of fix rectangular meshing system and will be discussed in the following sub-session titled with validation of the simulation results.

2.7.1 Validation of the Simulation Result with Benchmark

There are several cases of validation, which have been done in order to verify the KULES method. The validation is done through comparison with other researcher's simulation and experimental works. First of all, in order to determine the effect of different grid spacing of KULES method, comparison with an experimental case has been done by (Nakayama, 2000). Two different grid setting was used to compare with the experimental cases. The first case contain 50x40x30 grid in streamwise, lateral, and vertical directions respectively, while the near wall grid spacing is as large as 35 wall units. On the other hand, the grid spacing for second case is finer, that is 66x64x112 with near wall grid resolved to 3.0 wall unit. Result of the comparison are shown in different way as shown as Figure 2.36 below.

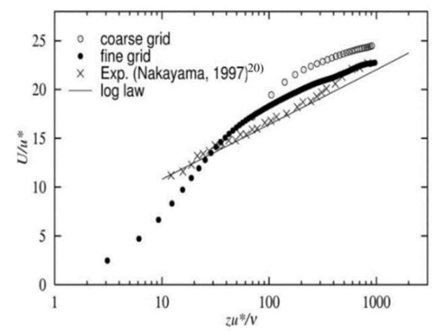

a) Mean velocity distribution in wall coordinates

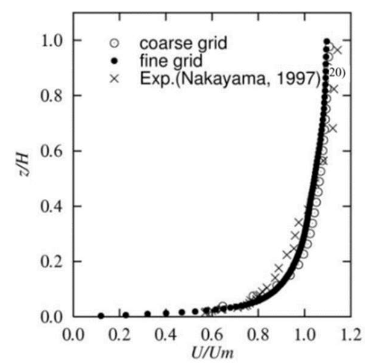

b) Mean Velocity distribution in linear scale

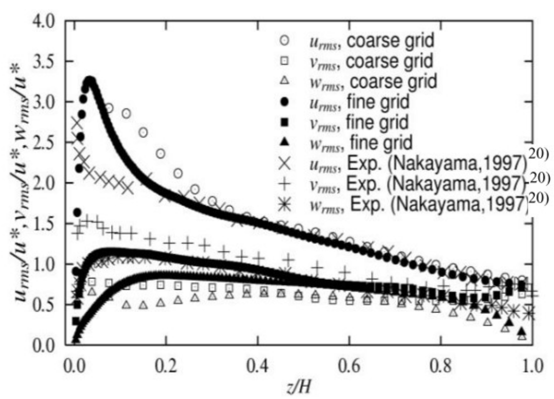

c) Turbulent intensity distributions

Figure 2.36: Comparison of Mean Velocity and Turbulence Intensity between KULES Method Experimental Case

From Figure 2.36a, it shows that velocity of both KULES in the logarithmic layer distributed above the standard log law and experimental data. Moreover, result from the finer grid is seemingly closer to both the standard log law and experimental data. Results in Figure 2.36b, which is the linear scale, do not show much different. Therefore, conclusion could be made that even though grid from the KULES method is not sufficient to resolve the near wall region, and the wall shear stress might be under predicted, the overall calculation of velocity profile is fairly well (Nakayama, 2012). On the other hand, results that are shown in Figure 2.36c are the turbulent intensities that are normalized by the friction velocity. From Figure 2.36c, some discrepancy could be seen in the result of streamwise intensity, transverse intensity, and spanwise intensity. Whereby the streamwise intensity with the peak position farther away the wall is over predicted, while transverse and streamwise intensities are under predicted. Likewise the result from Figure 2.36a, the results from finer grid is once again closer to experiment result.

In order to validate the implementation of side boundaries, second validation cases was done. The case which is used for comparison is done by (Joung and Choi, 2009) which simulate the flow in a square channel with side walls and rigid free surface as upper boundary through Direct Numerical Simulation (DNS) method. Moreover, the generation of the secondary flow, which is influenced by boundary condition, could be examined and compared as shown as Figure 2.37 below. In Figure 2.37 below, the DNS method is compared with KULES with different Reynold numbers, which are 10 times, and 100 times of DNS case respectively. Contour value in Figure 2.37 below are mean velocity, which is normalized by the bulk average velocity.

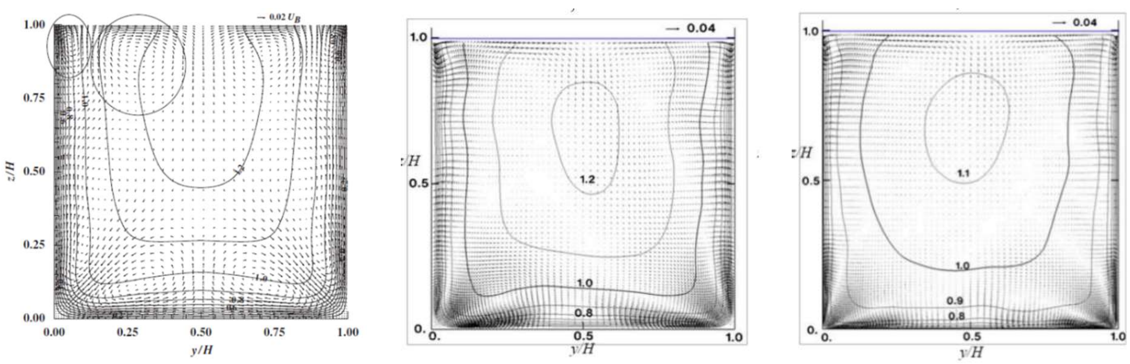

a) DNS (Joung and Choi) Re=1.0✕104 ; Fr=0 b) KU LES Re=1.0✕105 ; Fr= 0.30 c) KULES Re=1.0✕106 ; Fr= 0.39

Figure 2.37: Comparison of Mean Primary and Secondary Flows of DNS and KULES

From Figure 2.37 above, besides of the lack of smoothness of the distribution in KULES method compared to DNS, which might due to different Reynold number and insufficient average time, the secondary circulation directed towards the bottom corner is reproduced. Moreover, near the surface, both inner and outer circulations are reproduced correctly with smaller horizontal context. In addition, comparison of Reynold shear stress component $\overline{u'v'}$ in relation with velocity gradient in horizontal direction y are also been down as shown as Figure 2.38 below, in which value of the Reynold shear stress components are normalized by the average shear stress τ_w . This is done in order to validate the calculated Reynold stress. In Figure 2.38 below, the results of KULES are consistent with DNS result of lower Reynold numbers.

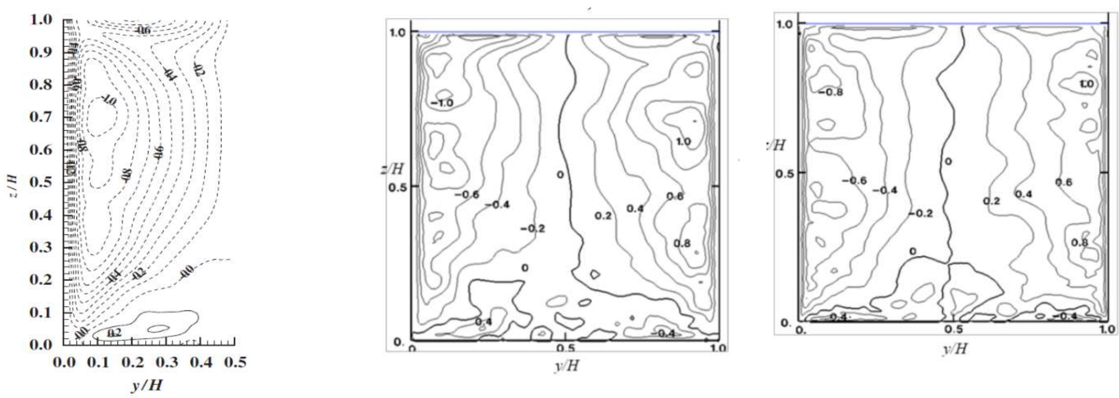

a) DNS (Joung and Choi)
Re=1.0×104 ; Fr=0

b) KULES
Re=1.0×105 ; Fr= 0.30

c) KULES
Re=1.0×106 ; Fr= 0.39

Figure 2.38: Comparison of Reynold Shear Stress Component $\overline{u'v'}$

As mentioned at the earlier section, usage of the rectangular mesh might bring issues in some context. Therefore, validation is done so that sensitivity of near wall and accuracy of the overall flow results could be examined during the case when rectangular mesh is used to represent curved boundaries. Blanckeart's experiment (Blanckaert, 2010) as mentioned at section 2.4.1 previously, was used for comparison. Whereby the simulation work aforementioned compute the flow using boundary-fitted curved coordinates. Setting of the KULES on the other hand are a bit different from Blanckaert's experiment since extra modification of the code is needed for the case more than 180° bend. Therefore, instead of 193°, the bend is set to be 135° in KULES while other parameter is the same so that comparison could be made. On the other hand, setting of the grid size for KULES is 222×192×70 with equally-space mesh in the horizontal direction with the spacing of 0.03m. While in vertical direction, the grid spacing is variable with minimum value of 0.5mm near bottom. The comparison of the results are shown as Figure 2.39 below. Both the distribution of velocity vector on the free surface, and the depth average velocity are normalized by the bulk average velocity Uav. Apparently, from Figure 2.39 below, depth average velocity of KULES agrees with both LES case from Inokuma and experiment case from Blanckeart. However, it seems that the flow appears to be accelerating more compared to both Inokuma's LES case and Bleanckeart's experiment case.

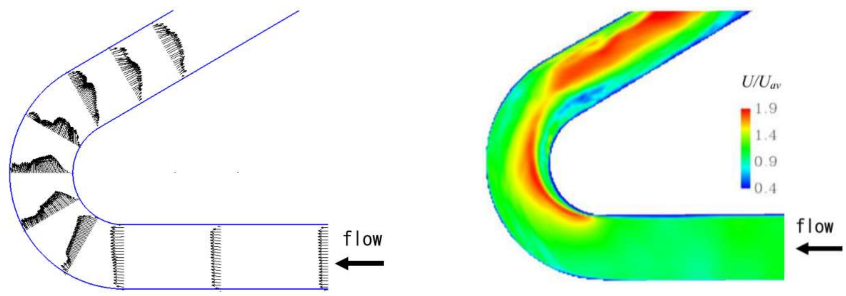

a) Surface velocity distribution in KULES

b) Depth-average velocity distribution in KULES

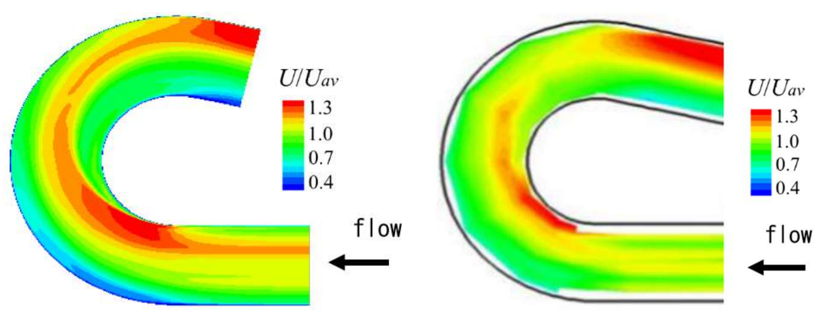

c) Depth-average distribution in LES of Inokuma case

d) Depth-average distribution in Blanckeart's experinment

Figure 2.39: Comparison of Flow Result with KULES and Other Researchers' Work

2.7.2 Application of KULES on River Flow

The river that is chosen for the KULES application is located in western Japan, which is the Ibogawa River. Two situations of the river are being considered that is the dry seasons and the flood seasons. Aerial photo during dry season and flood season in Ibogawa River are as shown in Figure 2.40a and Figure 2.40c respectively. While Figure 2.40b and Figure 2.40d show KULES result roughly corresponding to Figure 2.40a and Figure 2.40c.

As for the setting of KULES, 274×280×73 grid points are used as computational grid. Among all of the grids, horizontal directions is resolved in terms of 2m×2m while vertical direction is resolved in 0.15m. Moreover, periodic recycling boundary condition is applied. Whereby, upstream 100m was extended in order to have turbulent development. A fix flow rate of 100m3/s is set as initial condition, whereas calculation was continued to settle at a steady state. In addition, both hydrograph and the known depth-discharge relation are applied at upstream and downstream section respectively.

For the KULES simulation during dry season, a fix rate 100m3/s was applied and this is slightly larger than the normal dry season. KULES was computed for 200 seconds of real time. Then the discharge is reduced following a typical receding curve. Results obtained during the flow rate of 80m3/s are shown in Figure 2.40b. Figure 2.40d on the other hand, shows KULES result which is obtained during the flow rate maintained at 900m3/s. In which the flow rate is increased at a rate of 40m3/s every 60 seconds until it reaches 900m3/s during the process.

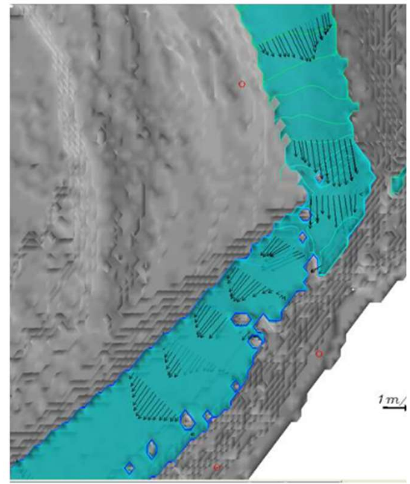

a) Aerial Photo of Ibogawa River During Dry Season with Discharge is 50m3/s

b) KULES Result of Instantaneous Flow when Discharge is 80m3/s

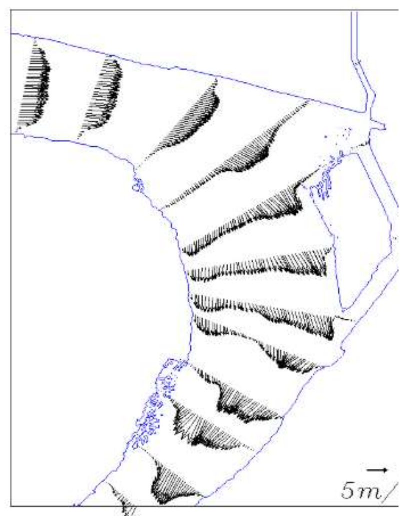

c) Aerial Photo of Ibogawa River During Flood with Discharge about 600m3/s

d) KULES Result of Averaged Flow when Discharge is 900m3/s

Figure 2.40: Comparison of Photo of Dry Season and Flood Season with Simulation Result

The process is done in order to simulate the flood which occurred during 10th of August in the year of 2009 as shown as Figure 2.40c. Photo of Figure 2.40c was taken when the discharge dropped at about 600m3/s from the peak which is

1600m3/s. The edge of the inundated region indicates the extent of the area, which was submerged under water.

CHAPTER 3

RESEARCH METHODOLOGY

The present research involves a number of different methods from the development of the models, execution of the simulation calculation, post-processing. The computed results, gathering the river and river flow data, analysing the flow and sediment data and comparing and validating with the simulation results. They are divided into two activities of the numerical simulation and the field survey.

The first step of the process of simulation is to collect the topography data of Perak River in Teluk Intan in order to create the river bed and the land model. The topography data were provided by the Department of Irrigation and Drainage (JPS) of Perak state. With the topography data, river bed bathymetry was constructed for the LES flow simulation and a graphic visualization was done. After that 2 simulation models could be run which 3a) cases without vegetation and 3b) cases with vegetation as shown as Figure 3.1 below. The result which are obtained from the simulation will be visualized using software MicroAVS.

In the field survey, three measurements were made. The flow velocity and the depth were measured by an Acoustic Doppler Current Profiler (ADCP) toed by a boat. The size of the bedload sediment, the concentration of suspended load were obtained by the sediment and water sampling. A drone was deployed to observed the water surface and turbidity from the air about 50m above ground. Multi parameter test are done on suspended solid which include PH value, salinity, total dissolve solid and etc. While sieve analysis test was done on sedimentation in order to determine the particle size distribution of the sedimentation. The characteristic of the suspended solid and sedimentation will provide more understanding regarding to river flow characteristic. The result of the velocity profile measurement by the ADCP are used to compare and validate with LES simulation result. The sediment size measurement result is used to evaluate the simulation result.

The process flow of simulation is shown in left hand side of Figure 3.1 while site survey process is shown in the right-hand side. Both result from simulation and site measurement are used for comparison.

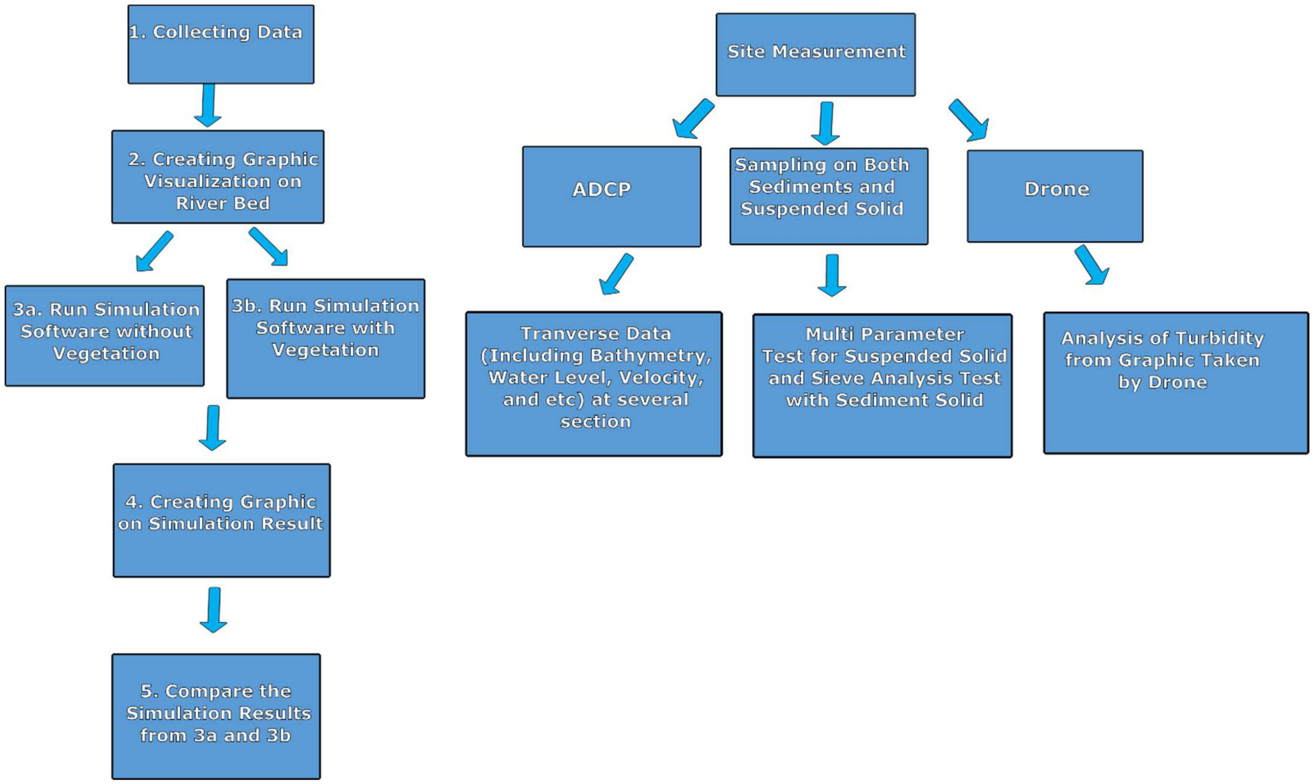

Figure 3.1 Schematic of Overall Methodology

3.1 Data Collection and bathymetry model

The bathymetry profile of Perak River in Teluk Intan were requested from Department of Irrigation and Drainage (JPS). The data that contain river depth information was provided by JPS as shown in Figure 3.2 below. Several site visitation was done in order to investigate the river conditions, types of vegetation around the river bank, and etc. In addition, photos have been taken for reference and to gain more understanding in order to create the simulation model.

Figure 3.2: One of the Data Provided by JPS

3.1.1 Creating Bathymetry model for Perak River in Teluk Intan

In order to create a bathymetry model for both calculation and visualization, grids were inserted on a map as shown as Figure 3.3. Intersection of the grid lines were converted to coordinate, and the coordinates started as (0,0) at the bottom coroner at left hand side. Data of depth of the bathymetry are key in to an excel file accordingly to the coordinates by using the data provided by JPS which is shown in Figure 3.4 below. Moreover, depth in some of the areas where the data provided by JPS did not cover, assumption was made base on the observation during site visitation.

Figure 3.3 Grid Lines Inserted in the Simulated Area of the River

CZ62 fx 2

	A	B	C	D	E	F	G	H	I	J	K	L	M	N	O	P	Q	R	S	T	U	V	W	X
1																								
2		y																						
3	x	0	0.5	1	1.5	2	2.5	3	3.5	4	4.5	5	5.5	6	6.5	7	7.5	8	8.5	9	9.5	10	10.5	11
4	0	2.00	2.00	2.00	2.00	2.00	2.00	2.00	2.00	2.00	2.00	2.00	2.00	2.00	2.00	2.00	2.00	2.00	2.00	2.00	2.00	2.00	2.00	2.00
5	0.5	2.00	2.00	2.00	2.00	2.00	2.00	2.00	2.00	2.00	2.00	2.00	2.00	2.00	2.00	2.00	2.00	2.00	2.00	2.00	2.00	2.00	2.00	2.00
6	1	2.00	2.00	2.00	2.00	2.00	2.00	2.00	2.00	2.00	2.00	2.00	2.00	2.00	2.00	2.00	2.00	2.00	2.00	2.00	2.00	2.00	2.00	2.00
7	1.5	2.00	2.00	2.00	2.00	2.00	2.00	2.00	2.00	2.00	2.00	2.00	2.00	2.00	2.00	2.00	2.00	2.00	2.00	2.00	2.00	2.00	2.00	2.00
8	2	2.00	2.00	2.00	2.00	2.00	2.00	2.00	2.00	2.00	2.00	2.00	2.00	2.00	2.00	2.00	2.00	2.00	2.00	2.00	2.00	2.00	2.00	2.00
9	2.5	2.00	2.00	2.00	2.00	2.00	2.00	2.00	2.00	2.00	2.00	2.00	2.00	2.00	2.00	2.00	2.00	2.00	2.00	2.00	2.00	2.00	2.00	2.00
10	3	2.00	2.00	2.00	2.00	2.00	2.00	2.00	2.00	2.00	2.00	2.00	2.00	2.00	2.00	2.00	2.00	2.00	2.00	2.00	2.00	2.00	2.00	2.00
11	3.5	2.00	2.00	2.00	2.00	2.00	2.00	2.00	2.00	2.00	2.00	2.00	2.00	2.00	2.00	2.00	2.00	2.00	2.00	2.00	-2.59	-7.17	-6.37	-5.57
12	4	2.00	2.00	2.00	2.00	2.00	2.00	2.00	2.00	2.00	2.00	2.00	2.00	2.00	2.00	2.00	2.00	2.00	2.00	2.00	-7.17	-16.34	-14.74	-13.14
13	4.5	2.00	2.00	2.00	2.00	2.00	2.00	2.00	2.00	2.00	2.00	2.00	2.00	2.00	2.00	2.00	-0.80	-3.60	-3.90	-4.20	-6.72	-9.24	-8.43	-7.62
14	5	2.00	2.00	2.00	2.00	2.00	2.00	2.00	2.00	2.00	2.00	2.00	2.00	2.00	2.00	2.00	-3.60	-9.20	-9.80	-10.40	-6.27	-2.13	-2.12	-2.10
15	5.5	2.00	2.00	2.00	2.00	2.00	2.00	2.00	2.00	2.00	2.00	2.00	2.00	2.00	-0.51	-3.01	-5.38	-7.76	-7.71	-7.67	-4.41	-1.16	-1.02	-0.89
16	6	2.00	2.00	2.00	2.00	2.00	2.00	2.00	2.00	2.00	2.00	2.00	2.00	2.00	-3.01	-8.02	-7.17	-6.31	-5.62	-4.93	-2.56	-0.18	0.08	0.33
17	6.5	2.00	2.00	2.00	2.00	2.00	2.00	2.00	2.00	2.00	2.00	2.00	-0.45	-2.89	-5.16	-7.42	-6.53	-5.63	-4.16	-2.70	-1.25	0.19	0.44	0.69
18	7	2.00	2.00	2.00	2.00	2.00	2.00	2.00	2.00	2.00	2.00	2.00	-2.89	-7.78	-7.30	-6.82	-5.89	-4.95	-2.71	-0.46	0.05	0.56	0.80	1.04
19	7.5	2.00	2.00	2.00	2.00	2.00	2.00	2.00	2.00	2.00	-0.47	-2.95	-4.93	-6.91	-6.64	-6.38	-5.30	-4.23	-2.20	-0.18	0.12	0.41	0.48	0.55
20	8	2.00	2.00	2.00	2.00	2.00	2.00	2.00	2.00	2.00	-2.95	-7.89	-6.97	-6.04	-5.99	-5.93	-4.72	-3.50	-1.70	0.11	0.18	0.25	0.15	0.05
21	8.5	2.00	2.00	2.00	2.00	2.00	2.00	2.00	-0.93	-3.87	-5.42	-6.97	-6.44	-5.92	-5.61	-5.31	-4.60	-3.90	-2.36	-0.83	-0.72	-0.62	-0.72	-0.83
22	9	2.00	2.00	2.00	2.00	2.00	2.00	2.00	-3.87	-9.73	-7.89	-6.04	-5.92	-5.79	-5.24	-4.68	-4.49	-4.30	-3.03	-1.76	-1.62	-1.48	-1.59	-1.70
23	9.5	2.00	2.00	2.00	2.00	2.00	-0.51	-3.02	-5.90	-8.79	-7.00	-5.22	-5.24	-5.27	-5.06	-4.86	-4.13	-3.40	-2.44	-1.48	-1.50	-1.52	-1.55	-1.58
24	10	2.00	2.00	2.00	2.00	2.00	-3.02	-8.04	-7.94	-7.84	-6.12	-4.39	-4.57	-4.75	-4.89	-5.03	-3.77	-2.50	-1.85	-1.19	-1.38	-1.56	-1.51	-1.46
25	10.5	2.00	2.00	2.00	2.00	2.00	-2.77	-7.54	-7.36	-7.19	-6.14	-5.09	-4.84	-4.60	-4.43	-4.26	-3.33	-2.40	-2.10	-1.81	-1.62	-1.43	-1.31	-1.19
26	11	2.00	2.00	2.00	2.00	2.00	-2.52	-7.03	-6.79	-6.54	-6.16	-5.78	-5.11	-4.44	-3.97	-3.49	-2.90	-2.30	-2.36	-2.42	-1.86	-1.30	-1.11	-0.92
27	11.5	2.00	2.00	2.00	1.25	0.49	-2.69	-5.87	-5.72	-5.58	-5.09	-4.61	-4.26	-3.91	-3.47	-3.04	-2.62	-2.21	-2.33	-2.46	-2.05	-1.65	-0.56	0.54
28	12	2.00	2.00	2.00	0.49	-1.02	-2.86	-4.70	-4.66	-4.62	-4.03	-3.43	-3.40	-3.37	-2.98	-2.58	-2.35	-2.12	-2.31	-2.49	-2.25	-2.00	0.00	2.00
29	12.5	2.00	2.00	2.00	0.21	-1.58	-3.35	-5.12	-4.95	-4.77	-4.44	-4.11	-3.89	-3.67	-3.06	-2.45	-2.38	-2.32	-1.92	-1.53	-0.77	0.00	1.00	2.00
30	13	2.00	2.00	2.00	-0.06	-2.13	-3.84	-5.54	-5.23	-4.92	-4.86	-4.79	-4.38	-3.97	-3.15	-2.32	-2.42	-2.51	-1.54	-0.57	0.72	2.00	2.00	2.00
31	13.5	2.00	2.00	2.00	-0.17	-2.33	-4.10	-5.87	-5.45	-5.04	-4.46	-3.89	-3.57	-3.25	-2.74	-2.22	-1.83	-1.44	-0.36	0.72	1.36	2.00	2.00	2.00

Figure 3.4: Data Inserted in Excel Table

3.2 Numerical Model for LES simulation

KULES method is used in this LES simulation, which is developed by faculty and student of Civil Engineering Department of Kobe University. The KULES method has been mentioned previously in section 2.7. This section will mainly cover the numerical model for KULES.

3.2.1 Boundary condition and Calculation Grid for LES

Free surface is treated as freely moving boundary and motion of air above the surface is ignored. In other words, on the free surface, while pressure and normal viscous stress are constant, the shear stress components vanish. Since the eddy-viscosity model aforementioned is used for the sub-grid stresses, zero shear deformation condition assures that both viscous and sub-grid shear stresses vanish. Effect of the surface tensions and the sub-grid fluctuation of the free surface are denoted by the following equation, which is equation 3.1.

$$p + \sigma K = 0 \tag{3.1}$$

From equation 3.1 above, coefficient of surface tension is denoted by σ, while radius of free surface curvature is denoted by K. In which, positive value of K represents convex free surface.

In the case of the river reach, which has clear inflow and outflow section, the flow is assumed to be subcritical for both inflow and outflow section. During some condition, standard logarithmic profile is assumed which is for fully developed two-dimensional channel flow, when the total flow discharge is known but the detail distribution of it is unclear. Furthermore, in order to produce the effect of turbulent fluctuation, fluctuating velocity components are needed to be included in the boundary. The turbulent fluctuation are taken some distance downstream at the inflow section, it is afterward superimposed on the prescribed mean-velocity at the corresponding position since it will only appear after some time and some distance of travel.

In the cases of flood, prescribed discharge hydrograph is used. The equation is shown as following equation 3.2. In which, the velocity is modified so that discharge approaches desire value within a relaxation time *T*i.

$$\frac{\partial \mathrm{u}}{\partial \mathrm{t}} = \frac{u}{T_i} \frac{Q(t) - \int_{S_i}^{t} u_n dS}{Q_i(t)} \tag{3.2}$$

From equation 3.2 above, time of t during the discharge is represented by Q(t)area of the inflow section in represented by Si and time constant is represented by Ti, and is normally given value to 50 times computational time step. Instead of prescribed, inflow section's free surface elevation is computed is computed in the solution process. However, there are several cases to be considered for outflow condition. First method is free outflow condition, which streamwise gradient of velocity component is set to be zero. In the second method, water level is prescribed while pressure distribution is assumed hydrostatic. Open-boundary condition as the third method, which is often use for coastal flow calculation. The final method, power relation is used to represent the depth-discharge relation. The equation is shown as equation 3.3 below.

$$\mathrm{H} = \mathrm{C_Q} Q_o^r + H_o \tag{3.3}$$

From equation 3.3 above, at the deepest point of outflow section, mean water surface elevation is denoted by H, in which the value of H is set to be constant across the outflow section, total flow rate at the outflow section is denoted by Q_o. Other parameter C_Q, r, and Ho is treated as constant and is used to fit the existing data.

Different kinds of grid are used for computational purpose in LES depending to the situation and usage. The usage of grid are also mentioned previously in section. Rectangular grid is used in KULES method based on finite difference method. Although there are several known disadvantages of using rectangular grid comparing other method such as unstructured grid, boundary following mesh system, mesh free method etc., however the prominent advantages of rectangular grid should not be underestimated. Advantages of rectangular grid are reflected in some situation such as river flood breeching levees and waves running up coasts. Whereas it is harder for boundary-fitted grid since redefinition is needed for the advances and retreat of waterfront. Furthermore, some development in terms of finite difference could be done directly by using rectangular mesh without worrying much about partial differential equation. However, there are a few adverse effects in rectangular mesh, which is needed to be put into consideration. When the flow region only occupies a little portion of the enclosing rectangular region, it is ineffective to use rectangular mesh. Nevertheless, the problem might not be severe when the memory space of the computer is big enough. Besides that, there might be some problem for rectangular mesh to represent curve boundaries, since the staggered position might not be coinciding with the real boundary. Due to this reason, sensitivity of the near wall and overall flow result is determined and will be discussed in the following section.

Figure 3.5 below shows how the variables are positioned in the rectangular grid in two condition including region of finite depth and near wetting front.

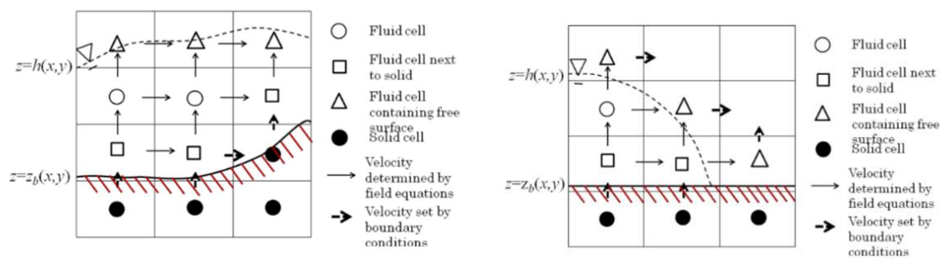

a) Region of finite depth b) Near wetting front

Figure 3.5: Variable Arrangement and Grid Cell Classification

Referring to Figure 3.5 above, pressure is calculated and defined at the centre of the cell while the velocity components are calculated centres of the cell surface, which is normal to the direction of the components. On the other hand, conservation of mass is formulated in the respective cell while conservation momentum is formulated different cubes cantered around the respective velocity components. Elevation of the solid surface and free surface are denoted by zb(x,y) and h(x,y) respectively. Meanwhile, flow region is bounded between these two surfaces. Fractional step method is used as a basic scheme. While momentum equations are advanced in an explicit way, pressure is determined and velocity is corrected in order to satisfy the continuity equation. Whereas the time-advanced velocity component in x direction which is u^* is obtained through Adams-Bashforth scheme as shown as equation 3.4 below.

$$\mathbf{u}^* = \boldsymbol{u}^{n-1} + \Delta \boldsymbol{t}\left(\boldsymbol{\delta}_x \boldsymbol{p}^{n-1} + \frac{2}{3}(\boldsymbol{f}_c^{n-1} + \boldsymbol{f}_v^{n-1}) - \frac{1}{2}(\boldsymbol{f}_c^{n-2} + \boldsymbol{f}_v^{n-2})\right) \quad (3.4)$$

From equation 3.4 above, time step is denoted by superscript, difference form of the derivative in direction of x is denoted by δ_x, difference form of the convective terms is denoted by f_c, divergence of the viscous and sub-grid scale stresses is denoted by f_v . The value of corrected velocity component u^n at the time $t = t^{n+1} = t^n + \Delta\mathrm{t}$ and the pressure p^n is obtained by the Highly Simplified MAC (HSMAC) iteration scheme (Hirt and Cook, 1972). In which, the corrected velocity component and pressure are determine through correcting u and p iteratively which are shown as following equation 3.5 and 3.6.

$$p^n = p^n + \delta p \ , \ \delta p = -\Omega \frac{D^*}{2\Delta t W} \tag{3.5}$$

$$u^n = u^n + \Delta t \delta p / \Delta x h \tag{3.6}$$

From equation above, Ω denotes the acceleration parameter, while W is determined through equation 3.7 below. In which, $\Delta\mathrm{x}_\mathrm{h}, \Delta y_h, and\ \Delta z_h$ are the distance between centre of the cell and centre of neighbouring cell in respective direction.

$$\mathrm{W} = 1/\Delta\mathrm{x}_\mathrm{h}^2 + 1/\Delta\mathrm{y}_\mathrm{h}^2 + 1/\Delta\mathrm{z}_\mathrm{h}^2 \tag{3.7}$$

On the other hand, for cell containing free surface, which is shown with triangle shape in Figure 3.5a, instead of using equation 3.5, and 3.6 for the pressure and velocity component correction, the pressure is prescribed by the free surface pressure condition. The divergence *D** in respect of the cell is used to move the position of the free surface when the sub-grid terms are not included. It is shown as following equation 3.8.

$$\mathrm{h}^{\mathrm{n}} = h^{n-1} - D^{*}\Delta z \Delta t \tag{3.8}$$

Whereas following equation 3.9 is used when sub-grid terms are included. From equation 3.9 below, $\delta_x^2 \ and \ \delta_y^2$ are the difference form of the second derivations in the direction of x and y respectively.

$$\mathrm{h}^{\mathrm{n}} = h^{n-1} - \left[D^{*}\Delta z - \gamma_{sgs}\left(\delta_x^2 h + \delta_y^2 h\right)\right]\Delta t \tag{3.9}$$

On the other hand, when dealing with the situation which the cell contains wetting front, it is needed to be treated separately. As shown by the thinner arrows in Figure 3.5b, the horizontal velocity component at the vertical surface which is the surface bordering cell indicate by square and indicate by triangle of the cell containing the wetting front are computed according to the equation of motion. As a result, pressure next to the cell that contain wetting front must be set to ensure the horizontal pressure gradient is evaluated. This is done by setting the pressure to atmospheric zero at the centre of the cell, which is outside of the front containing cell by using boundary condition.

3.2.2 Basic Governing Equation of LES

The filtered equation of motion and the continuity equation are used for KULES method, which are shown in equation 3.10 and 3.11 below. In the rectangular coordinate, spatially filtered velocity component is denoted by (u, v, w). On the other hand, (x, y, z) in the rectangular coordinate are used for filtered pressure. From equation 3.10 below, time, density and kinematic viscosity of water, are shown by t,ρ and v respectively. On the other hand, gravitational acceleration, and effective stress components are represented by g and τ respectively.

$$\frac{\partial u}{\partial t}+\frac{\partial u^2}{\partial x}+\frac{\partial uv}{\partial y}+\frac{\partial uw}{\partial z}=-\frac{1}{\rho}\frac{\partial \rho}{\partial x}+\frac{\partial}{\partial x}\left(v\frac{\partial u}{\partial x}+\tau_{xx}\right)$$
$$+\frac{\partial}{\partial y}\left(v\frac{\partial u}{\partial u}+\tau_{yx}\right)+\frac{\partial}{\partial z}\left(v\frac{\partial u}{\partial z}+\tau_{zx}\right)$$

$$\frac{\partial v}{\partial t}+\frac{\partial uv}{\partial x}+\frac{\partial v^2}{\partial y}+\frac{\partial vw}{\partial z}=-\frac{1}{\rho}\frac{\partial \rho}{\partial y}+\frac{\partial}{\partial x}\left(v\frac{\partial v}{\partial x}+\tau_{xy}\right)$$
$$+\frac{\partial}{\partial y}\left(v\frac{\partial v}{\partial y}+\tau_{yy}\right)+\frac{\partial}{\partial z}\left(v\frac{\partial v}{\partial z}+\tau_{zy}\right) \qquad (3.10)$$

$$\frac{\partial w}{\partial t}+\frac{\partial uw}{\partial x}+\frac{\partial vw}{\partial y}+\frac{\partial w^2}{\partial z}=-\frac{1}{\rho}\frac{\partial \rho}{\partial x}-g+\frac{\partial}{\partial x}\left(v\frac{\partial w}{\partial x}+\tau_{xz}\right)$$
$$+\frac{\partial}{\partial y}\left(v\frac{\partial w}{\partial y}+\tau_{yz}\right)+\frac{\partial}{\partial z}\left(v\frac{\partial w}{\partial z}+\tau_{zz}\right)$$

$$\frac{\partial u}{\partial x}+\frac{\partial v}{\partial y}+\frac{\partial w}{\partial z}=0 \qquad (3.11)$$

The movement of the water surface is resembled by solving spatially average kinematic equation for the elevation h of the frittered water surface along with the velocity field as shown as equation 3.12 below.

$$\frac{\partial h}{\partial t}+\frac{2u_s h}{\partial x}+\frac{2v_s h}{\partial y}=w_s+\frac{\partial}{\partial x}\tau_{hx}+\frac{\partial}{\partial y}\tau_{hy} \tag{3.12}$$

From equation above, u_s, v_s, w_s are the filtered velocity components at the water surface, while τ_{hx}, τ_{hy} are the sub-grid scale free surface fluctuation term. In some of the cases where variation of density are pronounce in some certain way, Boussinesq approximation might be used. In which, gravity term from equation 3.10 will be replace by equation 3.13 below.

$$\left(-1+\frac{\Delta\rho}{\rho_0}\right)g \tag{3.13}$$

From equation 3.13 above, ρ_0 is the reference density which is used to replace ρ in the rest of the equation, while $\Delta\rho$ is the deviation from it. Additional equation is needed for some cases depend on the changes on density. Whereby, in the case of the mix fluid which density is decided with small concentration of different density, equation 3.14 below is used. From the equation, while *D* is the coefficient of molecular diffusion, $\gamma_x, \gamma_y, \gamma_z$ is the sub-grid transport in direction of x, y, and z respectively.

$$\frac{\partial c}{\partial t}+\frac{\partial uc}{\partial x}+\frac{\partial vc}{\partial y}+\frac{\partial wc}{\partial z}=\frac{\partial}{\partial x}\left(\mathbf{D}\frac{\partial c}{\partial x}+\gamma_x\right)+\frac{\partial}{\partial y}\left(\mathbf{D}\frac{\partial c}{\partial y}+\boldsymbol{\gamma}_{\mathbf{y}}\right)$$

$$+\frac{\partial}{\partial z}\left(\mathbf{D}\frac{\partial c}{\partial z}+\boldsymbol{\gamma}_{\mathbf{z}}\right) \tag{3.14}$$

On the other hand, for the sub-grid model, there has been varies of model being propose throughout the decades. After several attempts, eddy viscosity model with effective kinematics viscosity v_{sgs} are seemingly suitable in which is less complex during implementation, numerically efficient, and mathematically simple. (Nakayama, 2012). The model is shown as equation 3.15 below while the evaluation of effective kinematics v_{sgs} value is shown as equation 3.16.

$$\begin{gathered}
\tau_{xx}=2v_{sgs}\frac{\partial u}{\partial x},\tau_{xy}=v_{sgs}\left(\frac{\partial u}{\partial y}+\frac{\partial v}{\partial x}\right),\tau_{xz}=v_{sgs}\left(\frac{\partial u}{\partial z}+\frac{\partial w}{\partial x}\right)\\
\tau_{yx}=v_{sgs}\left(\frac{\partial v}{\partial x}+\frac{\partial u}{\partial y}\right),\tau_{yy}=2v_{sgs}\frac{\partial v}{\partial y},\tau_{yz}=v_{sgs}\left(\frac{\partial v}{\partial z}+\frac{\partial w}{\partial y}\right)\\
\tau_{zx}=v_{sgs}\left(\frac{\partial w}{\partial x}+\frac{\partial u}{\partial z}\right),\tau_{zy}=v_{sgs}\left(\frac{\partial w}{\partial y}+\frac{\partial v}{\partial z}\right),\tau_{zz}=2v_{sgs}\frac{\partial w}{\partial z}
\end{gathered} \tag{3.15}$$

$$V_{sgs}=C_s\Delta^2\begin{bmatrix}4\left(\frac{\partial u}{\partial x}\right)^2+4\left(\frac{\partial v}{\partial y}\right)^2+4\left(\frac{\partial w}{\partial z}\right)^2+2\left(\frac{\partial u}{\partial y}+\frac{\partial v}{\partial x}\right)^2+\\ \left(\frac{\partial u}{\partial z}+\frac{\partial w}{\partial x}\right)^2+\qquad 2\left(\frac{\partial v}{\partial z}+\frac{\partial w}{\partial y}\right)^2\end{bmatrix}^{\frac{1}{2}} \tag{3.16}$$

From equation 3.16 above, Δ is the geometric average of the grid spacing while Cs is the Smagorinksy constant that the value is typically taken as 0.13. However, when it come to a near solid surface situation, the numerical grid is not assumed to resolve the situation. Therefore, the method of the near wall flow treatment is needed. One of the profound characteristic of the near wall flow is it give rises to resistant through the generation of turbulent (Nakayama, 2012). Furthermore, it is also agreed by (Robinson, 1991) that large resistance could be seen in the near wall region due to the eddies comparing others flow such as the non-turbulent laminar flows. Since the classical method, which proposed by Schumann and improved by few others do not seem to fit well with instantaneous flow data (Nakayama, Noda and Maeda, 2004), another method which follow empirical relation is used and it seemingly well (Nakayama, 2012). The equation of the method is shown in equation 3.17 below. In which, the Cartesian shear stress component of the wall are written in terms of the velocity. The velocity component which are calculated at points closes to a solid wall are denoted by (u_1, v_1, w_1)

$$\begin{aligned} \tau_{\mathrm{xy}} &= C_d \rho V_1 v_1 \,, \tau_{xz} = C_d \rho V_1 w_1 \\ \tau_{\mathrm{yx}} &= C_d \rho V_1 u_1 \,, \tau_{yz} = C_d \rho V_1 w_1 \\ \tau_{\mathrm{zx}} &= C_d \rho V_1 u_1, \tau_{zy} = C_d \rho V_1 v_1 \end{aligned} \tag{3.17}$$

Since the friction law for fluctuating flow is unknown, equation 3.18 below is used in order to relate the mean velocity and the mean wall stress.

$$C_d = \left[A \ln \frac{z_1 u_\tau}{v} + B\right]^{-2}, \frac{k u_\tau}{v} \leq 100 \; and \; \frac{Z_1 u_\tau}{v} > 10,$$

$$C_d = \left[\frac{z_1 u_\tau}{v}\right]^{-2}, \; \frac{k u_\tau}{v} \leq 100 \; and \; \frac{Z_1 u_\tau}{v} \leq 10, \tag{3.18}$$

$$C_d = \left[A \ln \frac{z_1}{k} + C\right]^{-2}, \; \frac{k u_\tau}{v} > 100$$

From the equation 3.18 above, value of A, B, and C are constant which is 2.5, 5.2, and 8.5 respectively. u_τ is the friction velocity which is defined by total wall stress τ_w. The wall stress τ_w are determine from equation 3.17 above. The roughness height is represented by k and z_i is the distance to the solid surface. Effect of the roughness height could be reflected in the boundary geometry when the roughness height k is larger than grid height and the elements can be resolved by grid.

While as for the terms τ_{hx} and τ_{hy} in the equation for free surface elevation, gradient model was used as shown as equation 3.19 below. In which, γ_{sgs} is taken to be corresponding to V_{sgs} (Hodges and Street, 1999).

$$\tau_{hx} = -\gamma_{sgs} \frac{\partial h}{\partial x}, \; \tau_{hy} = -\gamma_{sgs} \frac{\partial h}{\partial y}, \quad \gamma_{sgs} = \partial V_{sgs} \tag{3.19}$$

3.2.3 Vegetation Effect

According to (Wilson and Shaw,1977), spatial averaged effects are considered a common way of modelling, which is also suitable for method based on LES. The effect of vegetation on the river flow has been investigated by many researchers which are discussed at previously. In KULES method, vegetation effects are represented by inflow resistance D, as shown as equation 3.20 below. Figure 3.6 below shows some detail regarding to equation

$$\boldsymbol{D} = -\frac{1}{2} C_{Dv}(z) \Lambda V_f \boldsymbol{V_f} \tag{3.20}$$

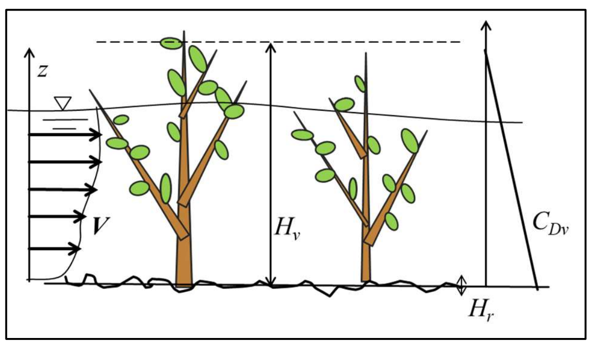

Figure 3.6: Inflow Resistant which Describes Vegetation Effect

From equation 3.20, drag coefficient is denoted by *CDv* which is used for different type of vegetation. As shown as Figure 3.6, the value of *CDv* vary linearly from bottom to the top with highest value at the bottom and gradually decreasing until the top. *Λ d*enote the leave-area density while the local flow velocity (*u,v,w*) is shown by *Vf* . In addition, the region of the vegetation of the simulation is shown in Figure 3.7b below by drag coefficient value *CDv.* The value of *CDv* is based on assumption during observation from several site visitation. Whereby, region which covered by high density of vegetation will be defined with higher value of drag coefficient, whereas lower *CDv* was set where vegetation is sparely distributed.

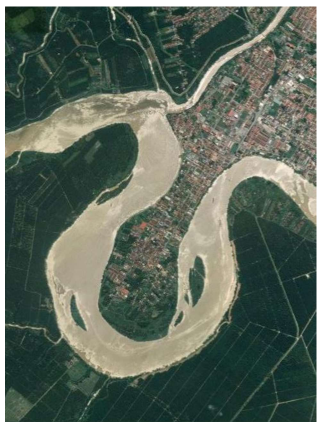

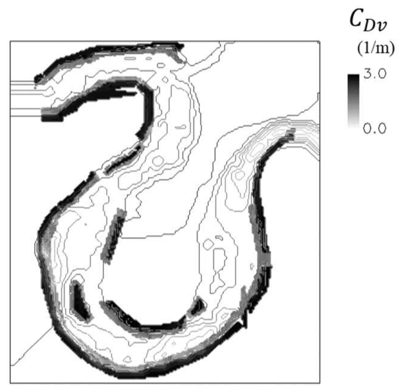

a. Perak River in Teluk Intan

b. Vegetation region showed by drag coefficient value C_{Dv}

Figure 3.7: Comparison between Real Map and Simulation Model

3.3 Data Visualization

Data is visualized after calculated by computer using KULES method. Visualization software such as MicroAVS, Gnuplots and fieldview were used during the process.

Microavs was used to visualize the bathometry of the selected part as shown as Figure 3.8 below. Before the software is used, all the data in excel form were transform into text file so the format can be recognized by Microavs.

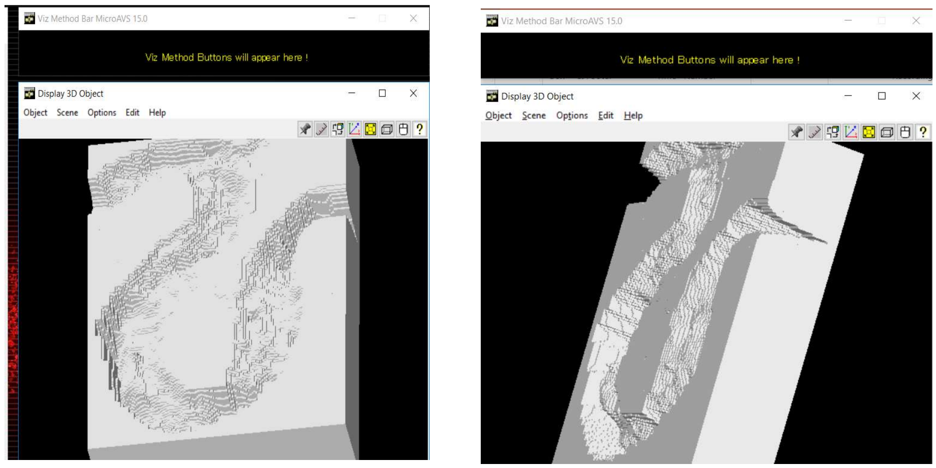

Figure 3.8: Visualization of Bathymetry of Perak River in Teluk Intan Using MicroAVS

The simulation software was run to calculate the data for the selected river including velocity, water level, vortex and etc. The Graphics software MicroAVS was also used for showing the result including hydrograph, velocity and vector as shown as Figure 3.10 and Figure 3.11 below.

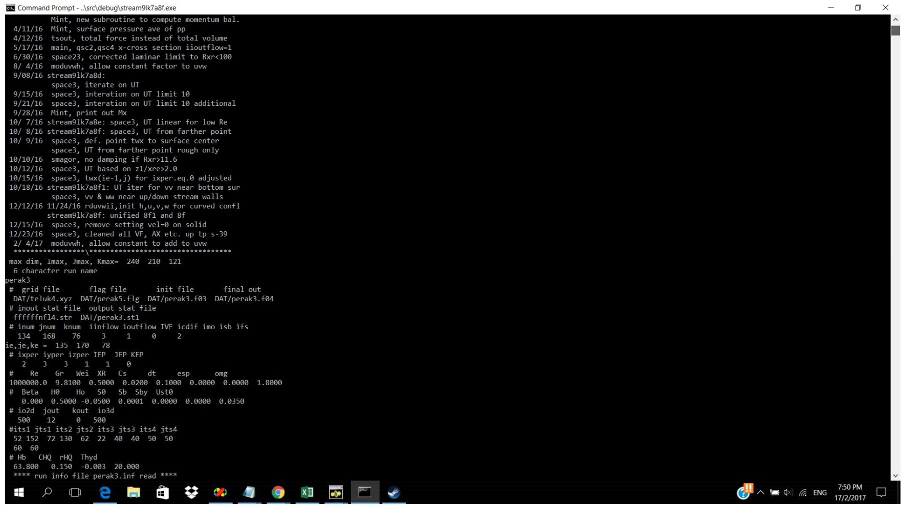

Figure 3.9: Running the Simulation Software

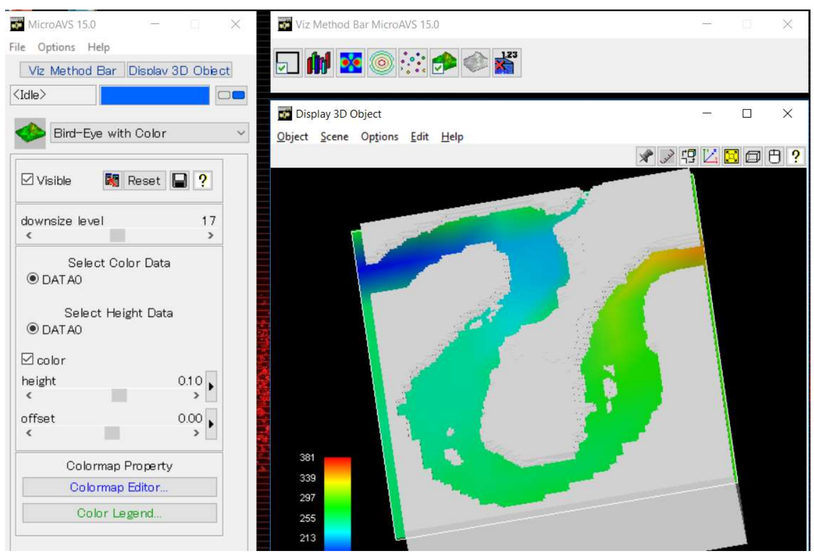

Figure 3.10: Using Microavs to Show Hydrograph of the Selected Area

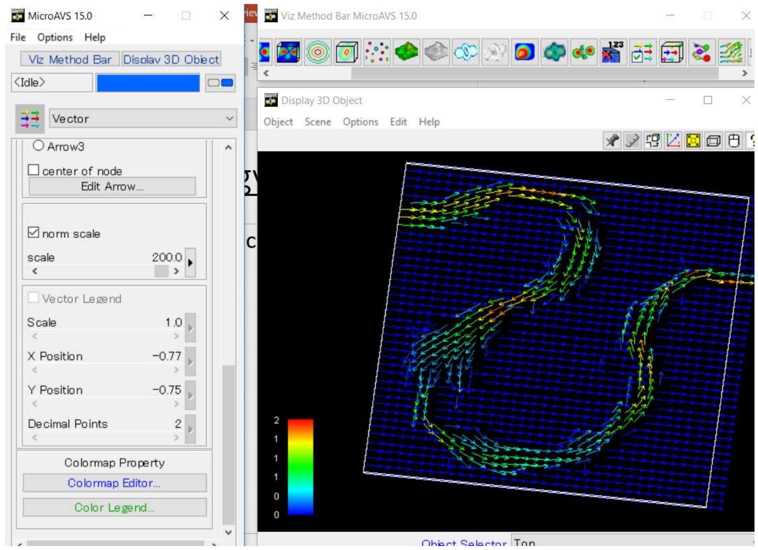

Figure 3.11: Using Microavs to Show Vector and Velocity of the Selected Area

3.4 Site Survey

On the other hand, site measurement includes ADCP, suspended solid sampling, sediment sampling, and observation using drone. Some result which are obtained from ADCP such as transverse velocity profile, water level, bathometry profile could be used to make comparison with simulation result. Multi parameter test are done on suspended solid which include PH value, salinity, total dissolve solid and etc. While sieve analysis test were done on sedimentation in order to determine the particle size distribution of the sedimentation. The characteristic of the suspended solid and sedimentation will provide more understanding regarding to river flow characteristic.

The field survey was conducted by the Acoustic Doppler Current Profiler (ADCP) to obtain the flow velocity distribution and the bed bathymetry, by the sediment sampler to obtain the characteristics of the suspended and bed sediment distributions and the water level gauge to obtain the changes of the water elevation and the surface slope. The ADCP measurement is conducted according to standard method ISO 2458:2021.

Equipment was being set up and testing has been done for ADCP measurement on the first day of the fieldwork, which is 15 July 2019. Figure 3.12 below shows some photos of setting up ADCP as well as test run. Figure 3.12a shows the mounting of ADCP and GPS on a small boat, while Figure 3.12b shows the preparation of data synchronizing between laptop before the release of ADCP into the river. After the setting up, the ADCP is then released into river as shown in Figure 3.12c below.

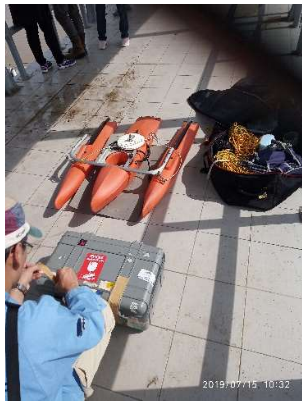

a) Setting up ADCP

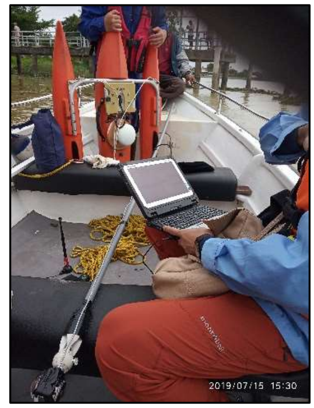

b) Synchronizing of ADCP

c) Releasing ADCP

d) Test run of ADCP

Figure 3.12: Setting Up and Test Run of ADCP Measurement

Figure 3.13 on the other hand, shows the measuring path of the ADCP. ADCP measurement started on the second day, which is on 16 July, the path of the ADCP measurement is shown in Figure 3.13a above. Furthermore, the measurement path is done in a manner of zigzag started from downstream to somewhere middle in upstream.

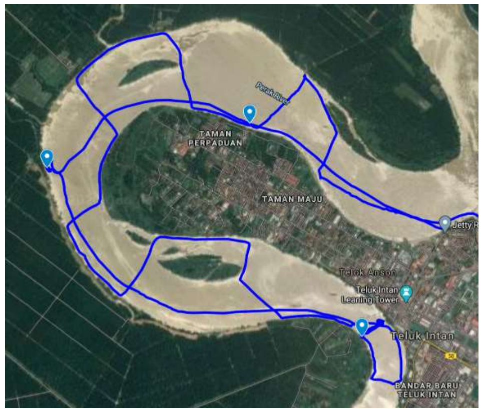

a) ADCP measurement path during 16 July 2019

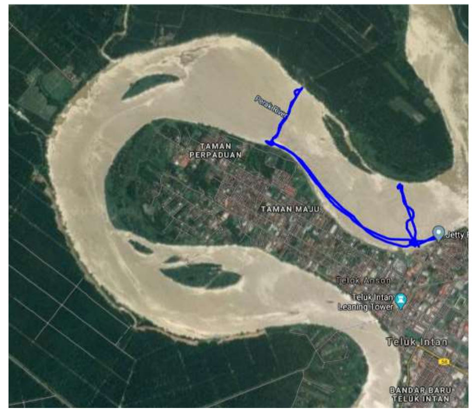

b) ADCP measuring path during 17 July 2019

c) ADCP measurement path during 18 July 2019

Figure 3.13: Measurement Path of ADCP on Different Date.

CHAPTER 4

RESULTS AND DISCUSSION

As described in the methodology chapter, the present work consists of two different efforts of obtaining the field data and to carry out the numerical simulation. The field data is needed to prepare the simulation run conditions and to verify the simulation results. The field survey results are described in section 4.1 while the numerical simulation results are given in section 4.2.

4.1 Result of the Fieldwork in Teluk Intan

The preliminary and vegetation survey were conducted in several trips to the main study area in Teluk Intan, Perak. The main river flow and the sediment survey were conducted from 15 July 2019 until 18 July 2019. During this onsite survey two boats in addition to a drone were used to carry out various tasks of surveying the flow and the sediment. Figure 4.1 shows the locations of the measurements and sampling locations. The flow velocity profiles and the depth have been measured by an Acoustic Doppler Current Profiler (ADCP). ADCP measurement are conducted along cross sections indicated as L1 to L7. At 3 points, the middle and near the left and right banks of these cross section, samples of bed sediments and suspended solid are taken at all 3 depths. Blueshades regions near L2 and L3 with drone icons are the area where the areal observation of the water surface by a drone with a still and movie cameras is conducted. The drone and ADCP survey are done at the same time so that the river flow conditions are visualized during the flow velocity measurement.

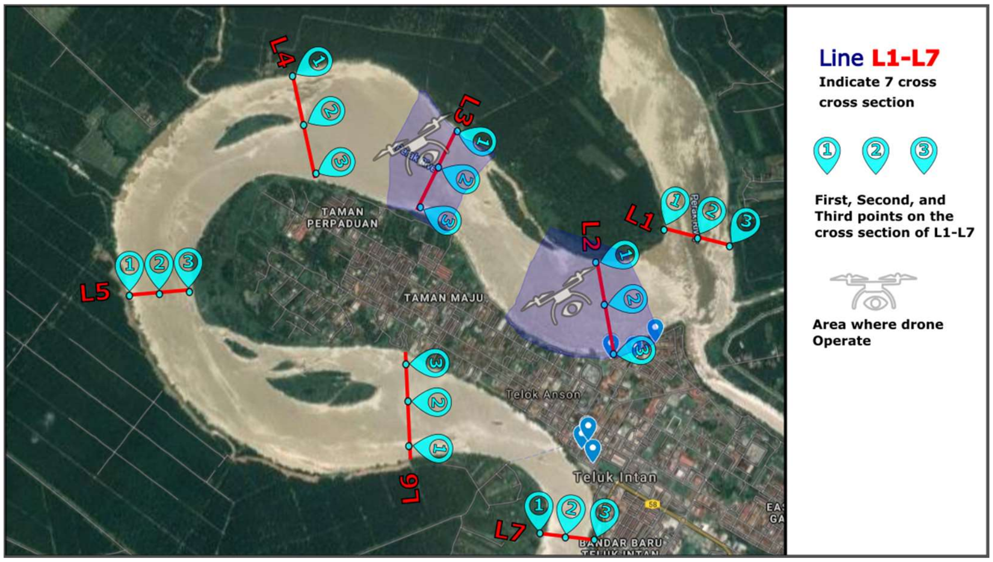

Figure 4.1: Location of Different Task that Were Carried Out

4.1.1 ADCP survey result

The ADCP results obtained during 16, 17, and 18 July 2019 are shown in Figure 4.2, Figure 4.3 and Figure 4.4, respectively.

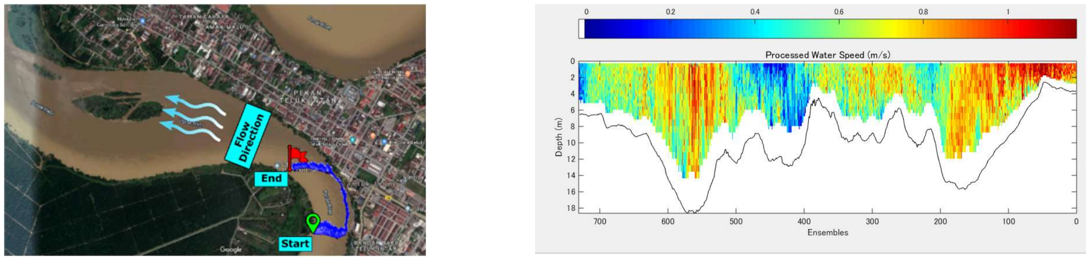

a) The Measurement is Taken at the Time 16:11

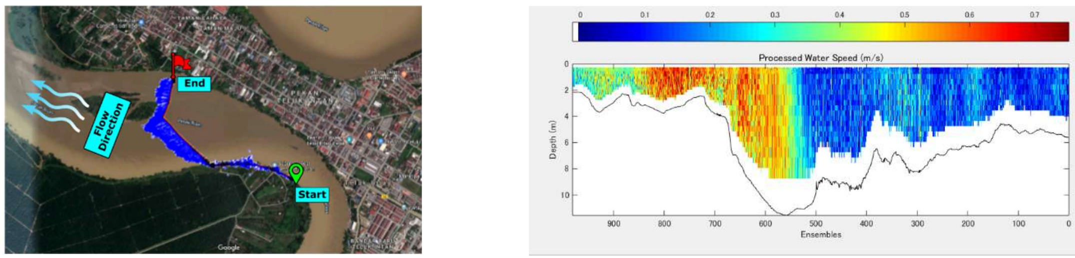

b) The Measurement is Taken at the Time 16:20

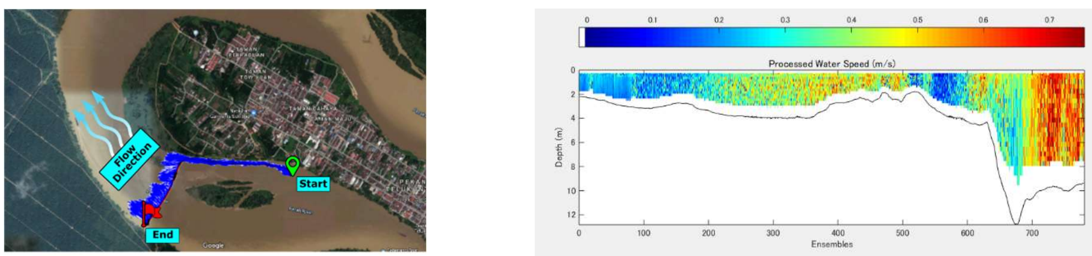

c) The Measurement is Taken at the Time 16:31

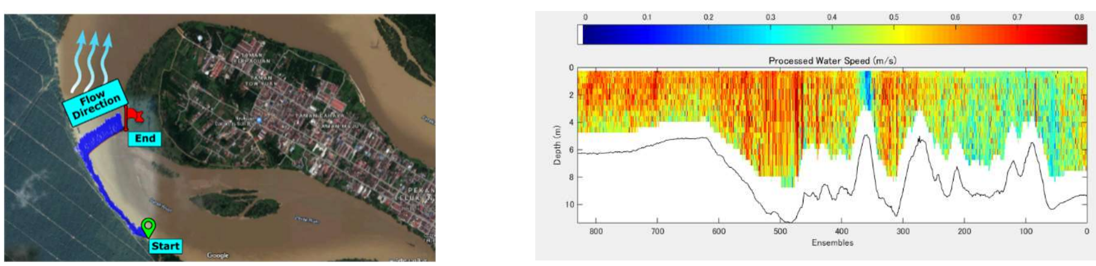

d) The Measurement is Taken at the Time 16:41

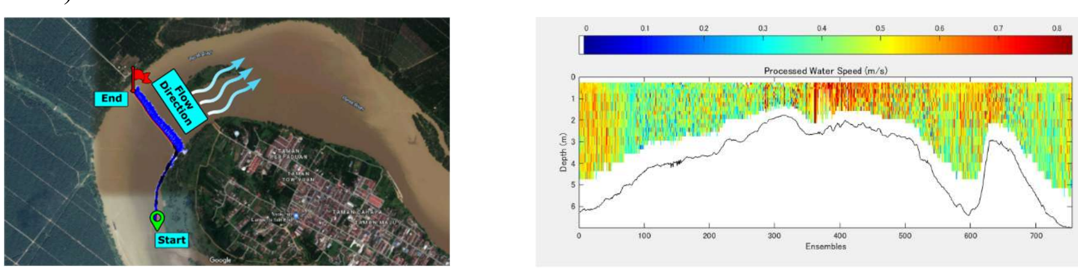

e) The Measurement is Taken at the Time 16:51

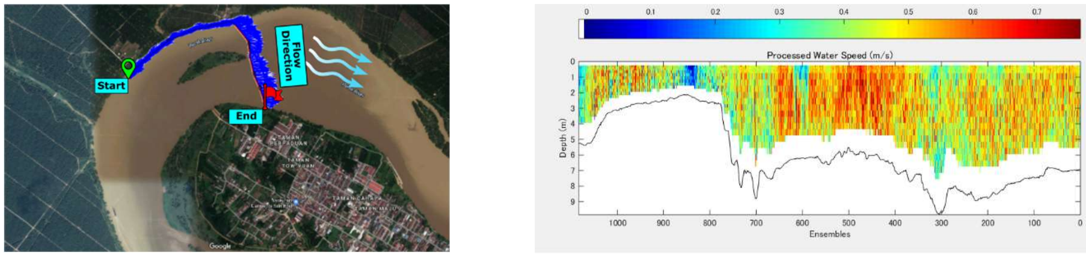

f) The Measurement is Taken at the Time 17:00

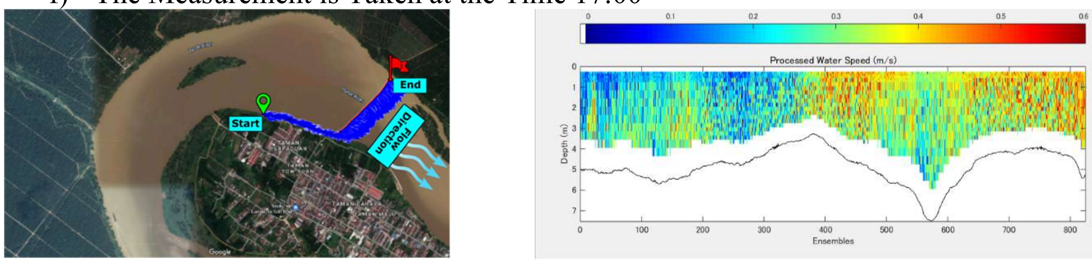

g) The Measurement is Taken at the Time 17:13

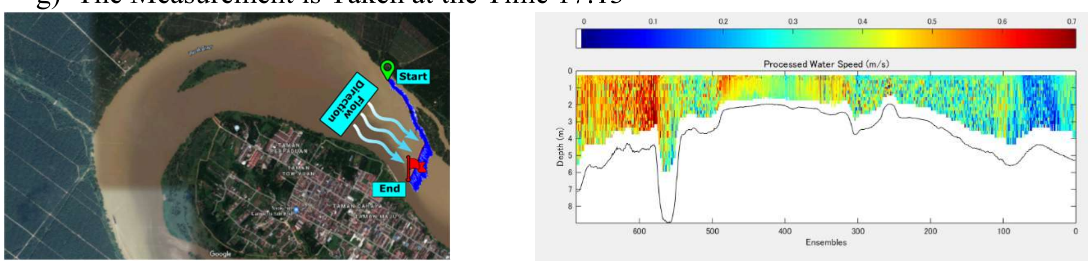

h) The Measurement is Taken at the Time 17:24

Figure 4.2: ADCP results during 16 July 2019

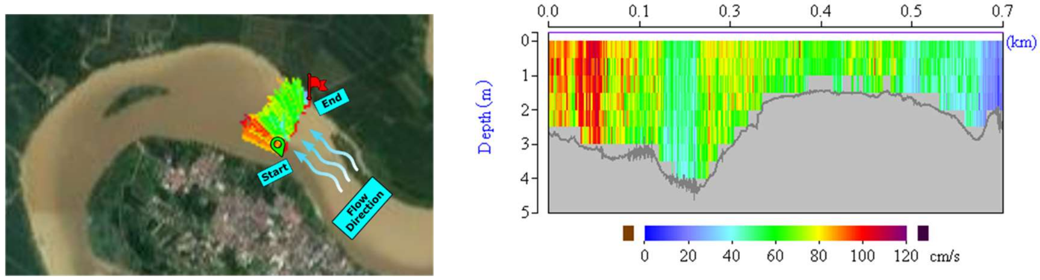

a) The Measurement is Taken at the Time 13:21 (forward flow)

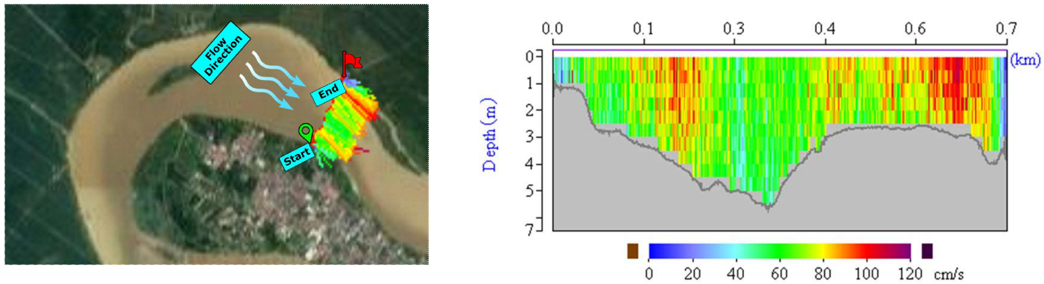

b) The Measurement is Taken at the Time 16:09 (backward flow)

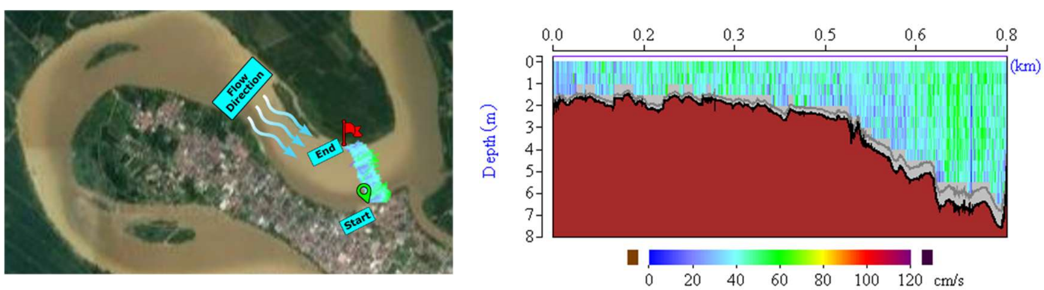

c) The Measurement is Taken at the Time 18:21 (backward flow)

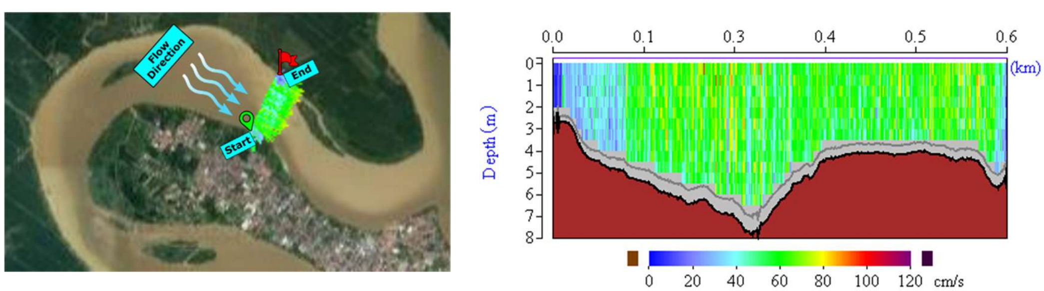

d) The Measurement is Taken at the Time 18:39 (backward flow)

Figure 4.3: ADCP results during 17 July 2019

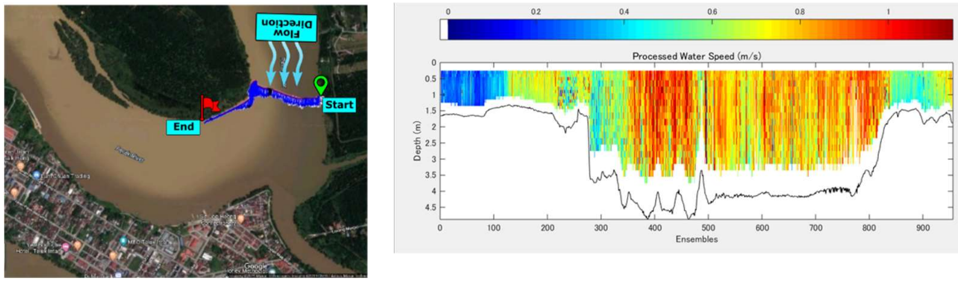

a) The Measurement is Taken at the Time 10:13

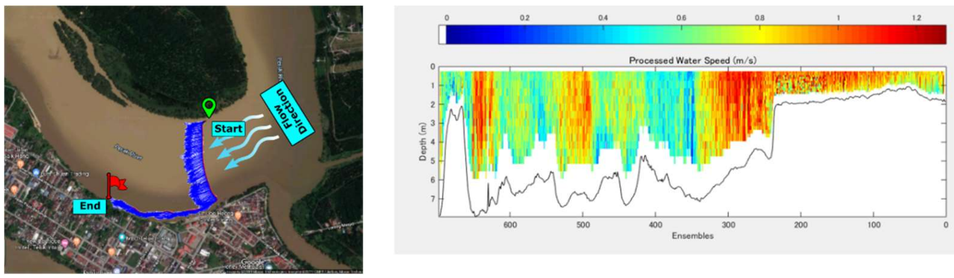

b) The Measurement is Taken at the Time 10:24

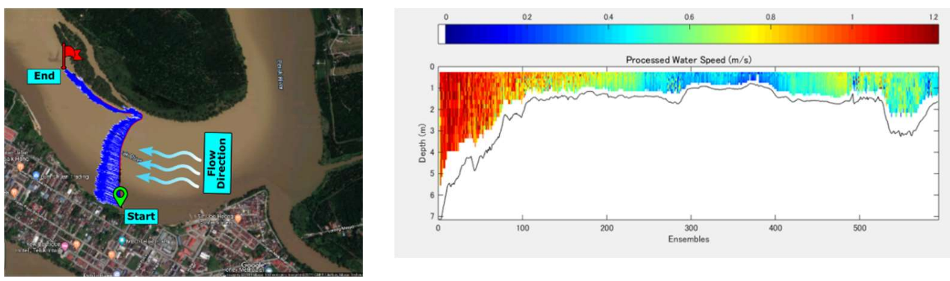

c) The Measurement is Taken at the Time 10:32

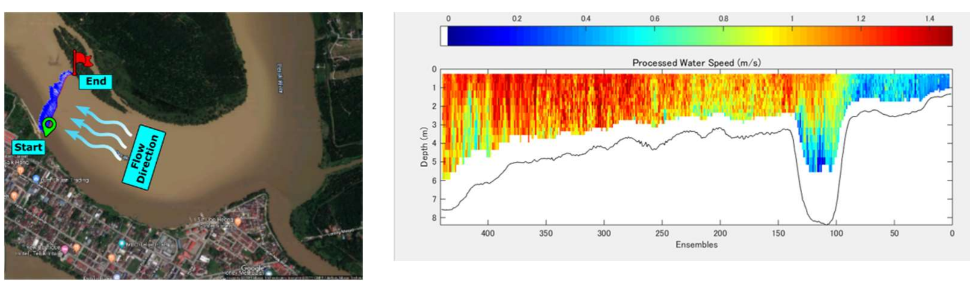

d) The Measurement is Taken at the Time 10:39

Figure 4.4: ADCP results during 18 July 2019

4.1.2 Suspended Solid Sampling and Analysis

As mentioned previously, samples of suspended solid were taken from L2 and L3 at different time. Moreover, the sample are taken 3 times with different depth at the deepest part of L2 and L3. Suspended solid sample was taken by the device shown in Figure 4.5. The device is heavy enough to submerge into the river in order to obtain suspended solid sample from different depth.

Figure 4.5: Suspended Solid Sampling Device

The suspended solid was tested by Multi Parameter Analyser, which are shown by Figure 4.6 below. The model is also shown by Figure 4.6 c. The results of these analyses are shown as Table 4.1 below. The table shows the Total Dissolved Solid (TDS), salinity, Dissolved Oxygen (OD). pH, and conductivity of each sample.

a. Probe of the Multi Parameter Analyser

b. User interface of Multi parameter Analyser

c. Model of the Multi Parameter Analyser

Figure 4.6: Multi Parameter Analyser

Table 4.1: Result of the Suspended Solid

Time Session (Batch)	Sample Name		Taken Time	TDS (ppm)	Salinity (ppm)	DO (mg/L)	pH	Oxidation reduction potential (mV)	Resistance (kn)	Conductivity (us)	Remarks
13:00	L2	1	13:04	79.12	47.21	4.27 (46.10%)	6.4	31.9	6.333	74.34	24.5
		2	13:10	79.16	45.35	3.90 (41.70%)	6.47	38.1	6.56	1.96	24.2
		3	13:15	79.28	48.27	3.24 (32.80%)	6.28	24.8	6.195	72.9	25.6
	L3	1	13:23	72.94	43.89	3.71 (41.9%)	6.48	26.3	6.841	68.51	25.3
		2	13:25	71.66	42.95	3.24 (36.80%)	6.58	11.4	6.978	67.98	25.4
		3	13:27	72.17	43.27	3.34 (39.20%)	6.48	18.2	6.904	67.71	25.1
15:30	L2	1	15:47	82.21	49.05	3.17 (35.20%)	6.37	35.7	6.097	77.68	25.5
		2	15:54	84.38	50.04	3.16 (34.20%)	6.5	29	5.918	79.12	25.3
		3	16:01	83.26	49.31	3.46(37.30%)	6.43	35.6	6.011	78.7	25.1
	L3	1	16:17	80.22	47.78	3.30 (36.5%)	6.5	25.4	6.228	75.83	24.4
		2	16:19	79.08	47.29	3.23 (35.3%)	6.88	12.8	6.322	75.01	24.5
		3	16:20	82.13	48.67	3.48 (38.6%)	6.57	18.7	6.107	77.5	24.4
18:00	L2	1	18:23	83.65	49.39	3.12 (35.2%)	6.5	27.3	5.989	79.39	25
		2	18:25	83.34	49.22	2.84(34.3%)	6.51	27.2	6	78.66	24.9
		3	18:27	83.25	49.93	3.28 (36.9%)	6.63	20.9	6.004	78.84	24.8
	L3	1	18:49	81.06	48.13	3.80 (41.2%)	5.95	55.3	6.191	76.45	24.6
		2	18:54	80.02	47.52	3.61 (41.4%)	6.67	18.7	6.225	74.81	25.3
		3	18:57	79.99	47.29	4.24 (46.8%)	6.58	15.3	6.266	75.97	24.1

4.1.3 Sediment sampling and sieve analysis

Samples of the sediment were obtained at 3 points within L1 to L7 from Figure 4.1. Sand dragger, which is heavy enough to sink on the riverbed, was used to obtain the bed sediment sample. Sieve analysis was done in order to obtain the particle sizes distribution of the sediment. The sieve analysis is performed according to standard method ASTM D422.

After the particle size distribution was conducted, the value of D50 and D90 were calculated. The results are shown as table 4.2 and Figure 4.7 below.

Table 4.2: D50 and D90 Value at Each Location

Location		D90	D50
L1	1	1.193	0.268
	2	1.597	0.614
	3	1.133	0.380
L2	1	1.813	0.816
	2	1.142	0.544
	3	1.682	0.800
L3	1	0.533	0.121
	2	0.542	0.223
	3	1.595	0.442
L4	1	2.051	1.009
	2	N/A	N/A
	3	2.243	1.265
L5	1	0.670	0.294
	2	0.662	0.293
	3	0.843	0.289
L6	1	0.227	0.123
	2	0.330	0.121
	3	0.794	0.372
L7	1	1.813	0.856
	2	1.206	0.383
	3	N/A	N/A

a) D50 b) D90

Figure 4.7: Particle Size Distribution

4.1.4 Measurement of Water Level

Several water level gauges were installed during site survey in order to observe the water levels at several position's along Perak River including the surveyed region. The positions of the water level gauges are shown as Figure 4.8 below. The water level gauges are installed L1L_W3, L3L_W1, L4R_W4, and L6-7R_W2 respectively. The names of the water level gauges are corresponded to site measurement from Figure 4.1. L1L_W3 and L3L_W1 are at the left-hand side near river bank at L1 and L3 respectively, while L4R_W4 and L6-7R_W2 are at the right-hand side near river bank. L4R_W4 is located in L4, on the other hand, L6-7R_W2 is located in between L6 and L7.

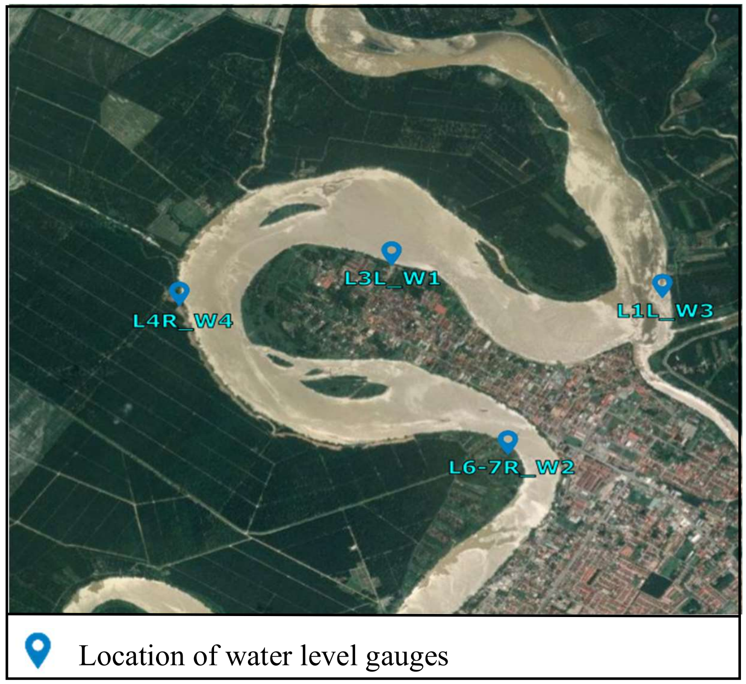

Figure 4.8: Location of Water Level Gauge

Figure 4.9a below shows the water level gauge. After setting up the water level gauge, it was then sunk into the river. Some floating bottles and ribbon were tied to the water level gauge as shown as Figure 4.9b below. Furthermore, GPS location was recorded to ensure that it could be easily retrieve in the future.

a) Water Level Guage b) Location of Water Level Gauge

Figure 4.9: Installation of Water Level Gauge

The water level gauges will record data including date and time when data being recorded, pressure, temperature, and depth. The data are recorded every 1 minute. Data for a long period of time could be stored in these devices which would provide some understanding for the river flow characteristic. Result of water level gauge are obtained during the site measurement which are shown as Figure 4.10 below. Some patterns of cycles between highest water level and lowest water level could be observed from the water level gauge results.

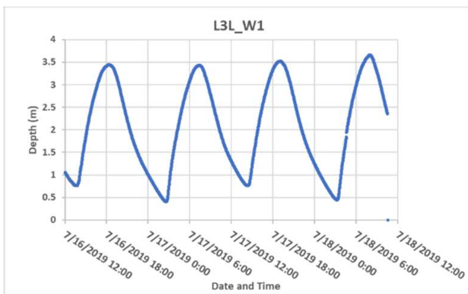

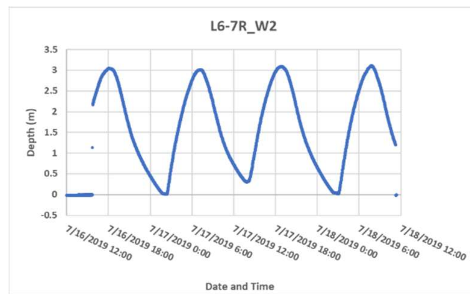

a. Result for L3L_W1 water level gauge b. Result for L3L_W1 water level gauge

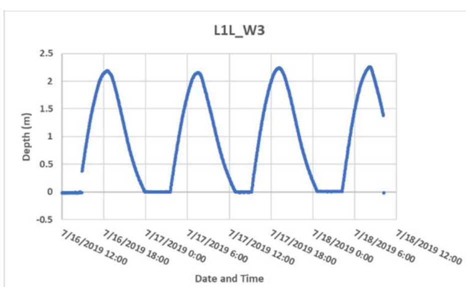

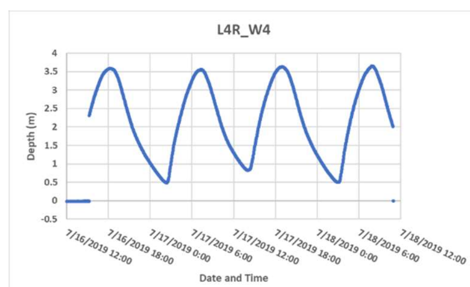

c. Result for L3L_W3 water level gauge d. Result for L4R_W4 water level gauge

Figure 4.10: Result of Water Level Gauge During the Site Measurement

Results of the water level gauge indicate the tidal effects. Figure 4.11 below shows the comparison of the tidal level in Bagan Datuk and the water levels in the surveyed reach of Perak River on 17 July 2019. Bagan Datuk is a town located near the river mouth which is at downstream of Perak River. Distance between Bagan Datuk and Teluk Intan along Perak River is about 60Km, the location of Bagan Datuk is shown in Figure 4.12 below.

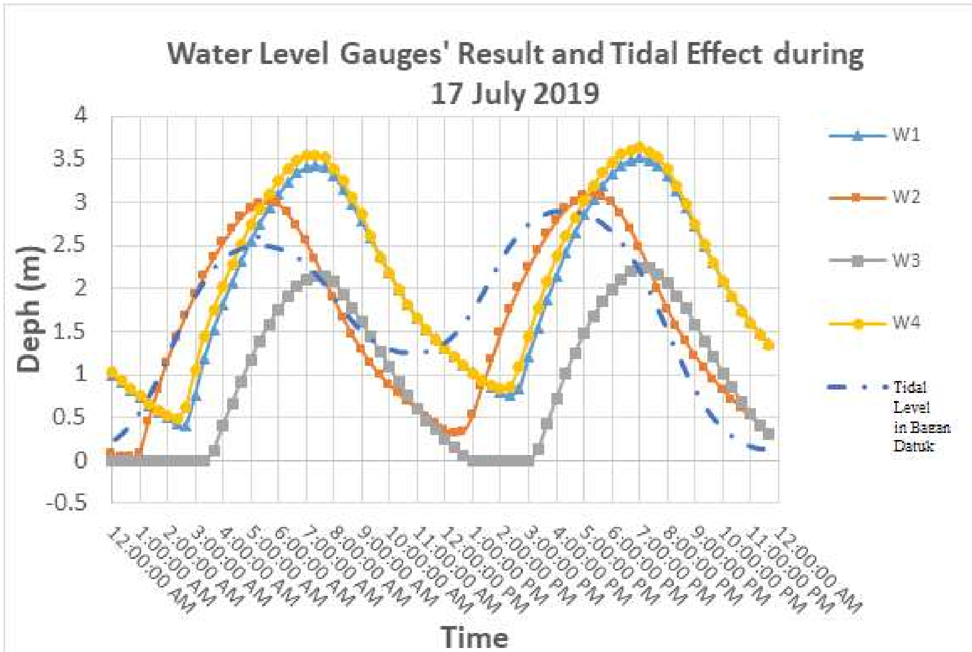

Figure 4.11: Comparison of Water Level Gauge's Result and Tidal Effect in Bagan Datuk

Figure 4.12: Location of Water Level Gauges and Tidal Effects in Bagan Datuk

Results obtained by water level gauges show about 1.4 hours lag from the tidal stage at Bagan Datuk. Figure 4.11 indicates two cycles, such pattern can also be found in all of the water level gauges marked as W1, W2, W3, and W4. The water level of the most downstream gauge W2 reaches its peak first. While water level gauges W1 and W4 reach the peak at around the same time, W3 which is the located most upstream is found slightly delay comparing to W1 and W4.

Water surface slope can be calculated using the result from water level gauges. Figure 4.13a below shows the location of two calculated water surface slope while Figure 4.13b shows the changes of water surface slope with time. Slope 1 is the increment of water elevation in downward direction which is the difference of water elevation at W4 and W1. Similarly, Slope 2 is the deference of water elevation at W2 and W4.

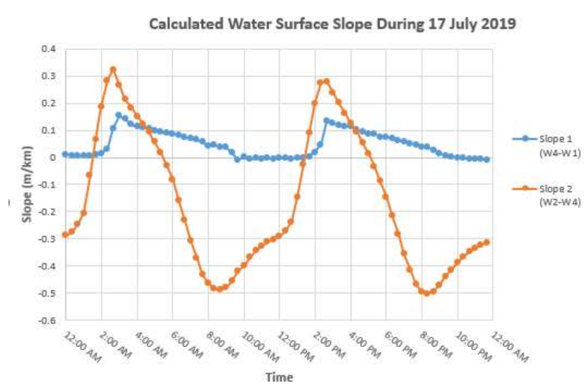

a. Location of Water Surface Slope

b. Calculated Water Surface Slope

Figure 4.13: Calculated Water Surface Slope and its' corresponding location

Furthermore, comparison between the water surface slope and ADCP measurement of the flow velocity were made. Figure 4.14 shows the calculated water surface slope during the ADCP measurements. In order to observe changes of flow characteristics and the results, the ADCP measurement were conducted three times at the same location on 17th July 2019.The ADCP measurement path, time and the results is shown in Figure 4.15 below. Figure 4.14 and Figure 4.15 show correlation between the flow direction and water surface slope. It is found that river flow in the downstream direction when the water surface slope is increasing. On the other hand, the river flow direction is reversed when the water surface slope is decreasing which can be observed in Figure 4.14, Figure 4.15b and Figure 4.15c. The difference in the river flow direction also affects the velocity profile. Such difference could be seen also in Figure 4.15a and Figure 4.15b whereby when the river is flowing downstream, core or high velocity appears at the left river bank which is shown in Figure 4.15a. Whereas core of high velocity is found at the right river bank as shown as Figure 4.15b. This could be explained by the meander effect whereby core of high velocity tends to move towards outer bank direction.

In conclusion, the results from the water level gauge not only shows the correlation between tidal effect and water surface elevation, meanwhile river flow direction could also be reflected by the surface flow direction and ADCP measurement.

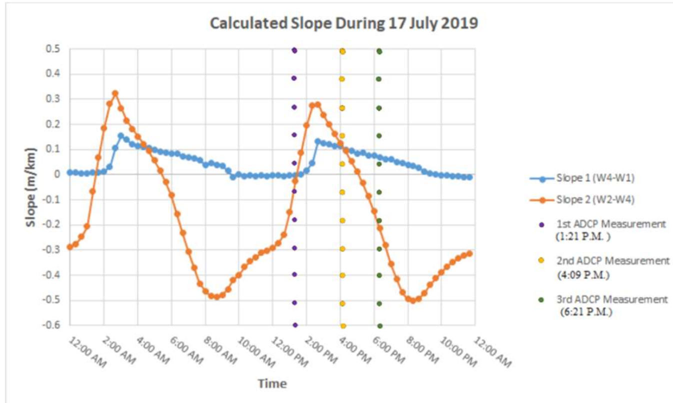

Figure 4.14: Calculated Water Surface Slope and the Time During ADCP Measurement were Conducted

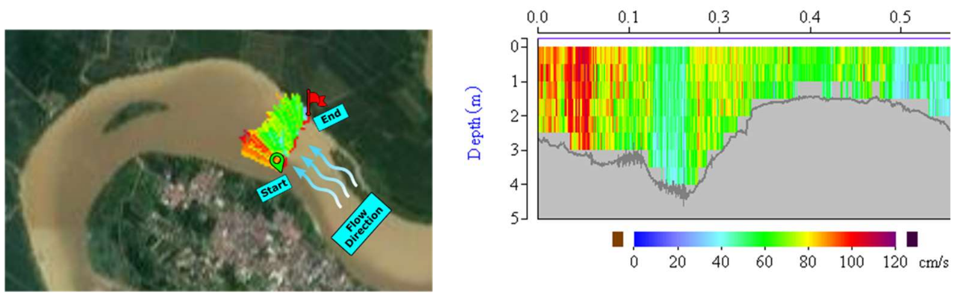

a. First ADCO Measurement on 17 July 2019 at the time of 13:21

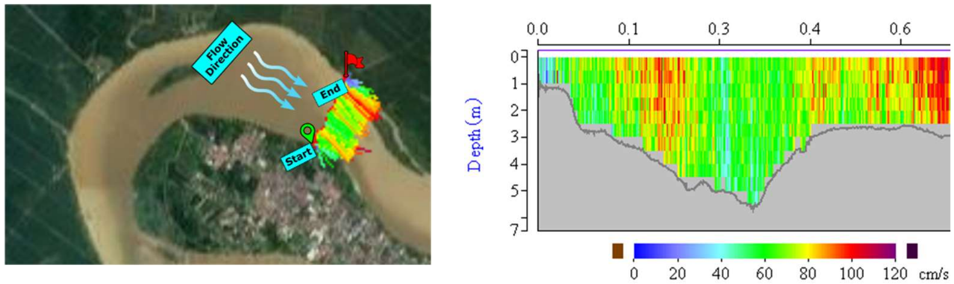

b. Second ADCP Measurement on 17 July 2019 at the time of 16:09

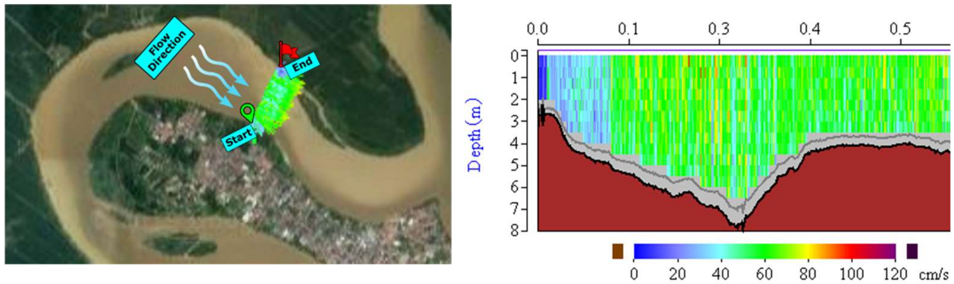

c. Third ADCO Measurement on 17 July 2019 at the time of 18:39

Figure 4.15: ADCP Measurement Location and Responding Velocity profile

4.2 Simulation Results

In order to represent resemble the realistic conditions of the river flow of the river reach, several different simulation cases were conducted. They include cases with vegetation, cases without vegetation, and cases with different hydrographs to simulate the realistic condition of the river flow. Results such as velocity profile, bed shear stress, movement of floating particles, and etc are calculated by KULES simulation software and the data is stored numerically. These data are then further visualized using software MicroAVS and GNU plots. Figure 4.16 below shows the visualized result visualized by MicroAVS and GNU plots. Moreover, simulation results by KULES is used to compare with results from field survey and other studies reported by other researchers. Results of different simulation case and their comparison will be discussed in following subsections.

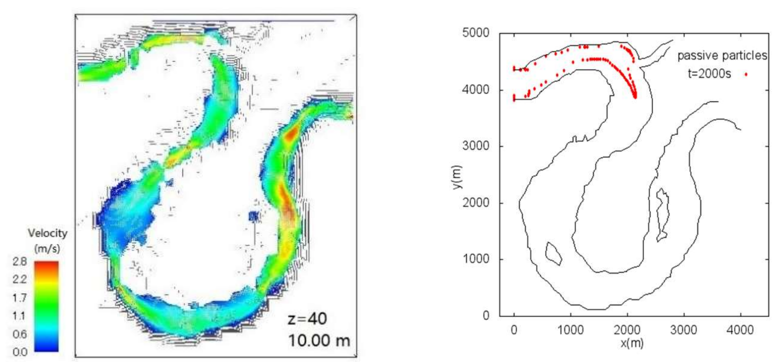

a) Horizontal velocity profile visualized using MicroAVS

b. Plotting of Floating object by using GNU plots

Figure 4.16: Results Visualized by Using MicroAVS and GNU Plots

4.2.1 LES Simulation Results of Cases with and without Vegetation

Vegetation plays an important role in the flow evolution in the meandering bend. There are, there are several studies that are done on the river with meandering river in order to study how the vegetation effect the flow distribution such as (Termini, 2017) and (Nepf,1999). Therefore, both LES simulation cases with and without vegetation were conducted in order to investigate whether the vegetation effect could be well reproduced by LES simulation. Table 4.3 shows the condition including the flow rate, the bed roughness, the average slope of the river, and grid properties for both the simulation runs. The results of the LES simulation run without vegetation are shown in Figure 4.17 and 4.18, while results of run with vegetation are shown in Figure 4.19 and 4.20. In Figure 4.17 and 4.19, Z is the number of grids in vertical direction. The height of each grid is 0.25m, therefore the elevation is determined by multiplying the numbers of grid Z and the grid's height 0.25m. Whereby Z=0 is chosen to be just below the lowest point of the river bed.

Table 4.3 Simulation Condition for Both Simulation Runs

Condition	Description
Flow rate	1000m3/s.
Floating object	110
Bed roughness	0.02 m
Average slope of the river	1/2000
Grid shape	Fixed rectangular mesh

Grid points	200 x 200 x 60
Grid spacing	20 m x 4m x 0.25

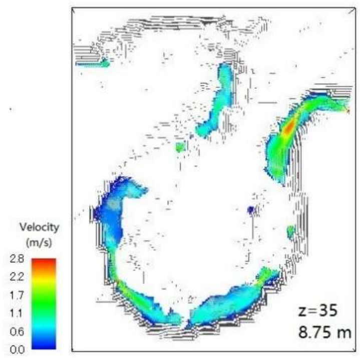

a) Velocity distribution at Z=35

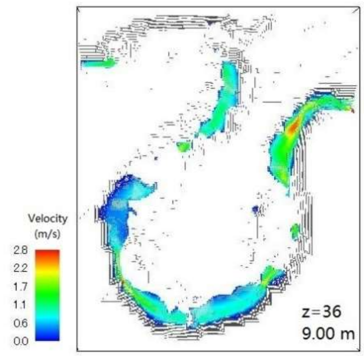

b) Velocity distribution at Z=36

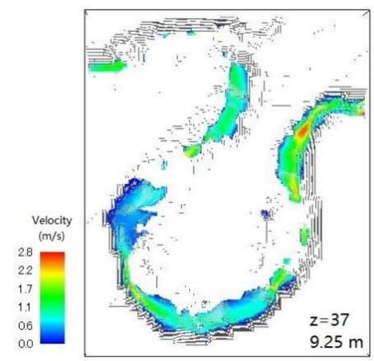

c) Velocity distribution at Z=37

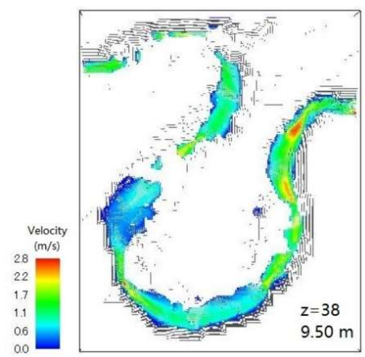

d) Velocity distribution at Z=38

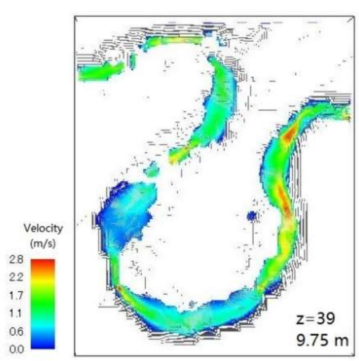

e) Velocity distribution at Z=39

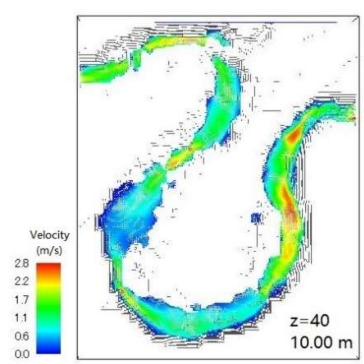

f) Velocity distribution at Z=40

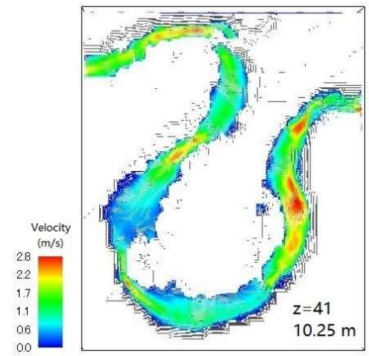

g) Velocity distribution at Z=41

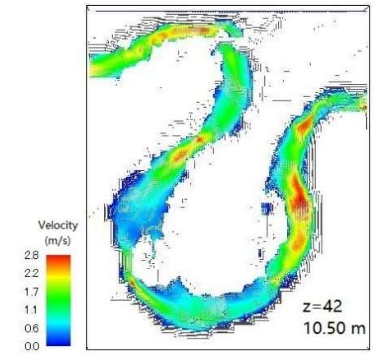

h) Velocity distribution at Z=42

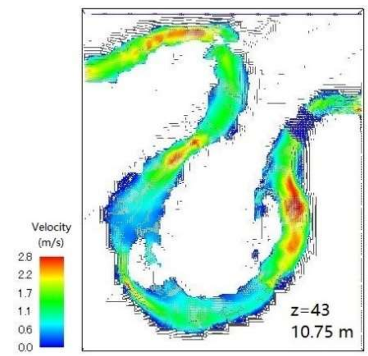

i) Velocity distribution at Z=43

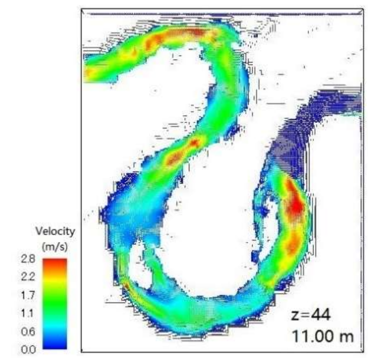

j) Velocity distribution at Z=44

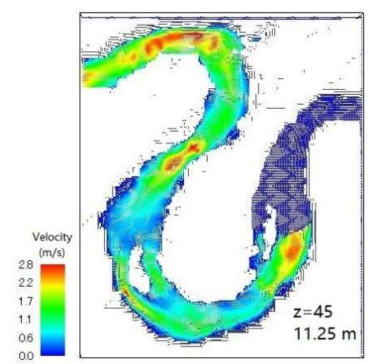

k) Velocity distribution at Z=45

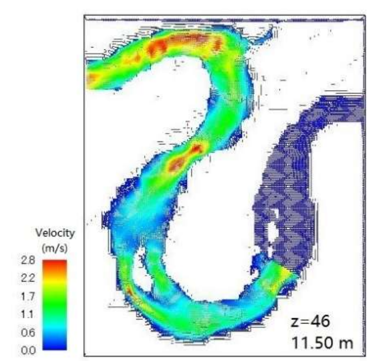

l) Velocity distribution at Z=46

Figure 4.17: Velocity Profile of LES Simulation Run without Vegetation in Different Elevation

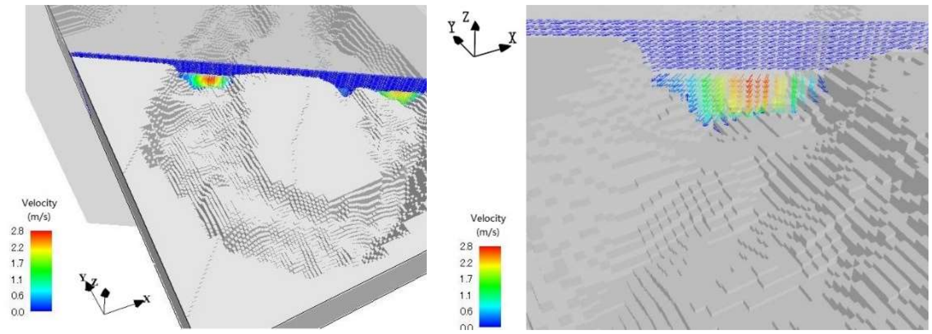

a. Plane View b. Cross Section

Figure 4.18: Cross Section Velocity Profile of LES Simulation Run without Vegetation

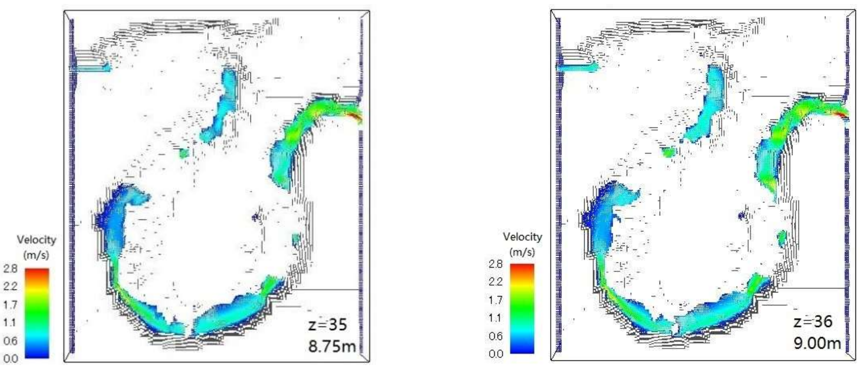

Velocity distribution at Z=35 Velocity distribution at Z=36

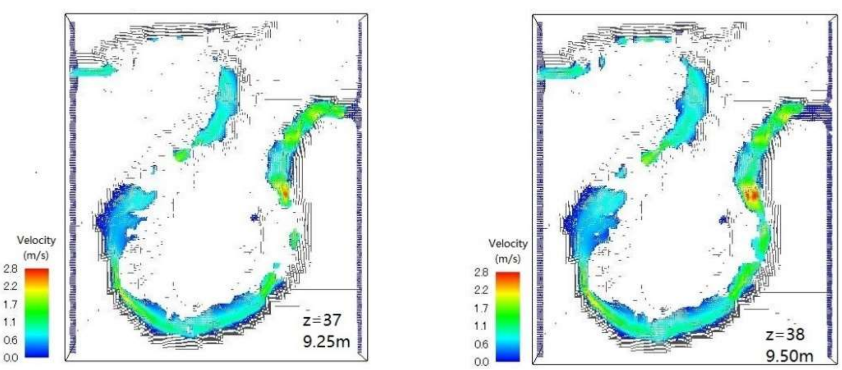

Velocity distribution at Z=37 Velocity distribution at Z=38

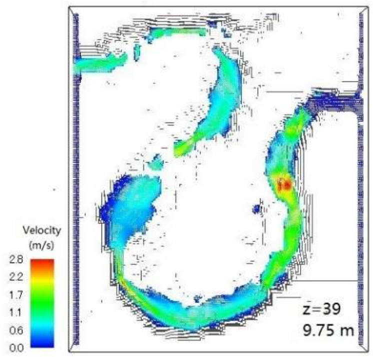

Velocity distribution at Z=39

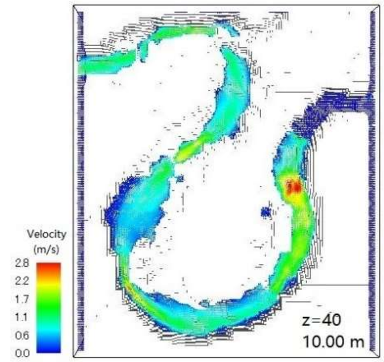

Velocity distribution at Z=40

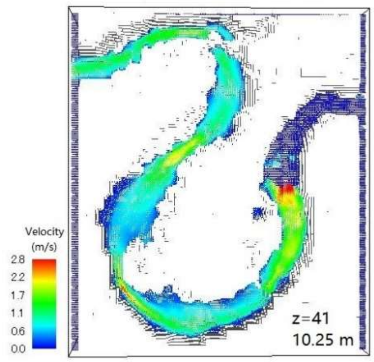

Velocity distribution at Z=41

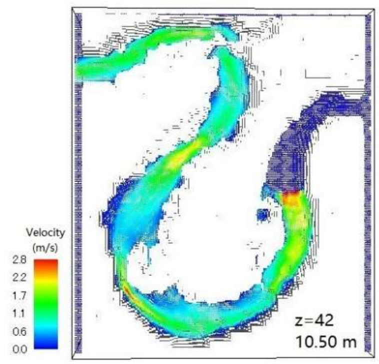

Velocity distribution at Z=42

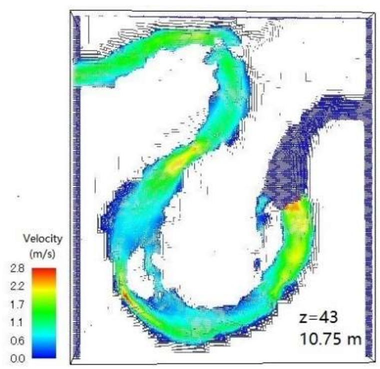

Velocity distribution at Z=43

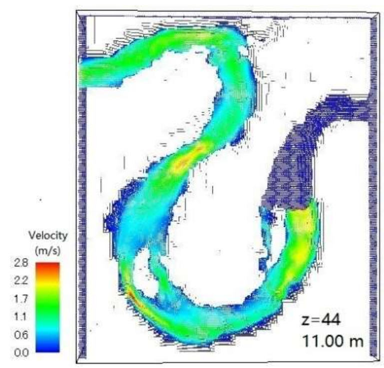

Velocity distribution at Z=44

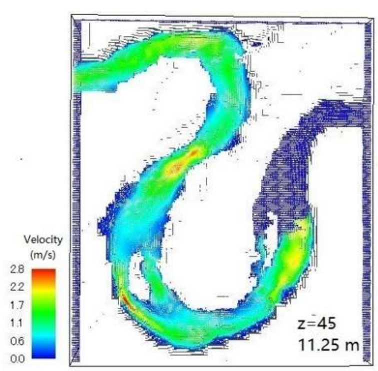

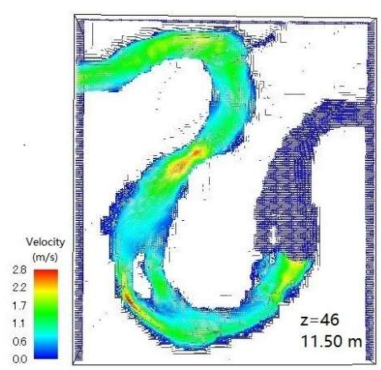

Velocity distribution at Z=45 Velocity distribution at Z=46

Figure 4.19: Velocity Profile of LES Simulation Run with vegetation in Different Elevation

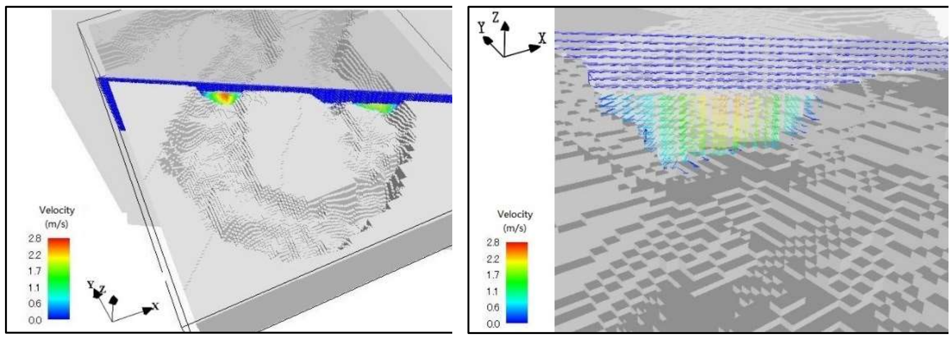

a) Plane View b. Cross Section

Figure 4.20: Velocity Distribution of LES simulation Run with Vegetation

Difference in the highest velocities could be observed between both simulations run. Highest velocities occur at z=43 and z=44 for the case without vegetation, while for cases with vegetation, highest velocities seem to occur at z=39, z=40. Figure 4.21 shows the comparison of these two runs during the highest velocity.

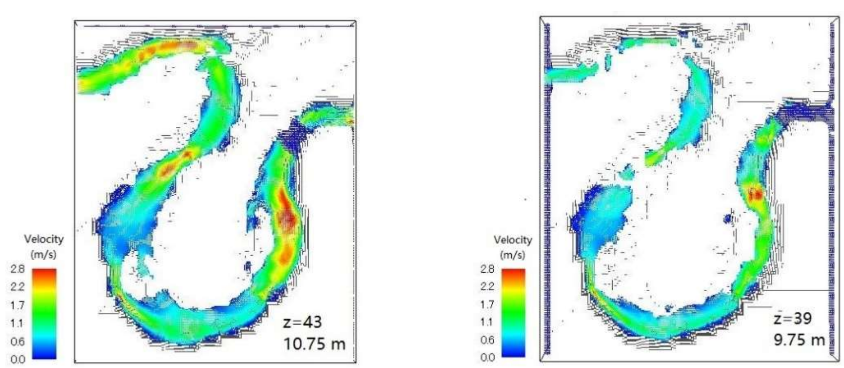

a) Case without vegetation (z=43)   b) Case with vegetation (z=39)

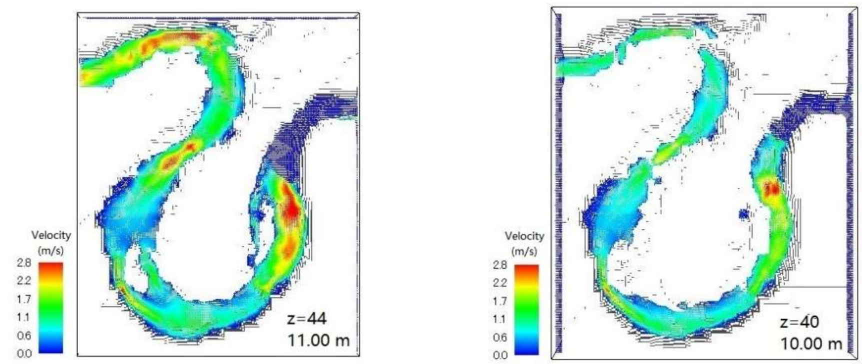

c) Case without vegetation (z=44)   d) Case with Vegetation (z=40)

Figure 4.21: Comparison of Velocity Distribution of Cases with and without Vegetation

From Figure 4.21, it could be seen that the velocity increases after each curve as shown in the red circle. Furthermore, the high velocity from the cases with vegetation which is shown in Figure 4.21b and Figure 4.21d is reduced compare to cases without vegetation. The results coincide with statements from (Termini, 2017) and (Nepf,1999) that the present of vegetation will affects the downstream flow development.

Further details of the flow distribution are shown in the cross-section velocity profile shown in Figure 4.18 and Figure 4.20. Figure 4.21 shows the comparison between KULES simulation and Termini’s experiment, whereby Figure 4.21a and Figure 4.21b are results from KULES and can be related to Termini’s laboratory experiment in Figure 4.21c due to their similar in morphology. Since the morphology of the Perak River are similar to the laboratory experiment from (Termini, 2017), the similarities and difference of the outcome for both the KULES simulation and laboratory experiment would be significant.

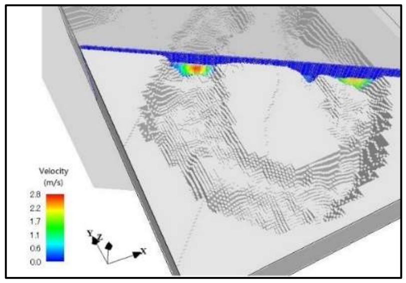

a) KULES simulation result

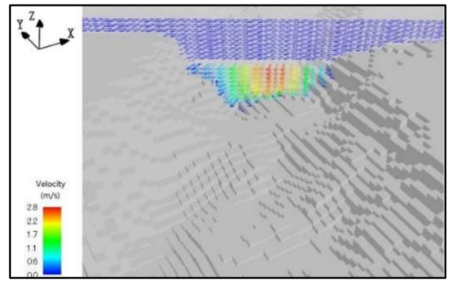

b) Cross section of Velocity Profile from KULES simulation result
(Area with red circle)

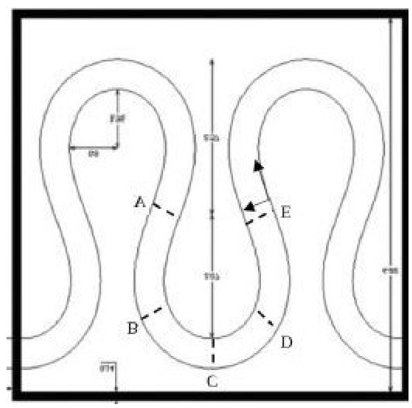

c) Termini's Laboratory Experiment

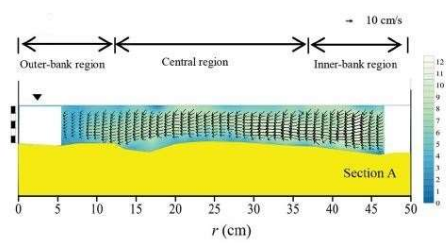

d. Cross section of Velocity Profile from Termini laboratory experiment
(Section A)

Figure 4.22: Comparison of Present KULES Result and Termini's Laboratory Experiment

The comparison of cases with and without vegetation from both KULES and Termini's experiment are shown in Figure 4.23. From the Figure, the results are seemingly consistence with Termini's experiment in many ways. First of all, the convective flow motion prevails over cross circulation in both cases with and without vegetation in KULES. In addition, core of high

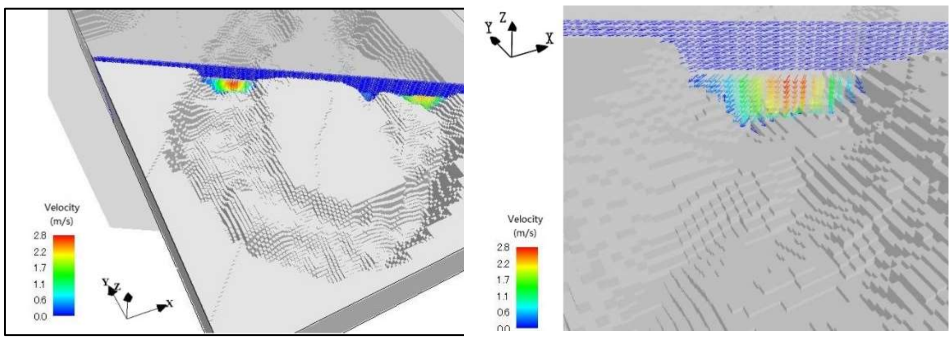

a) Case without Vegetation from KULES (Plane View)

b) Case without Vegetation from KULES (Cross-section)

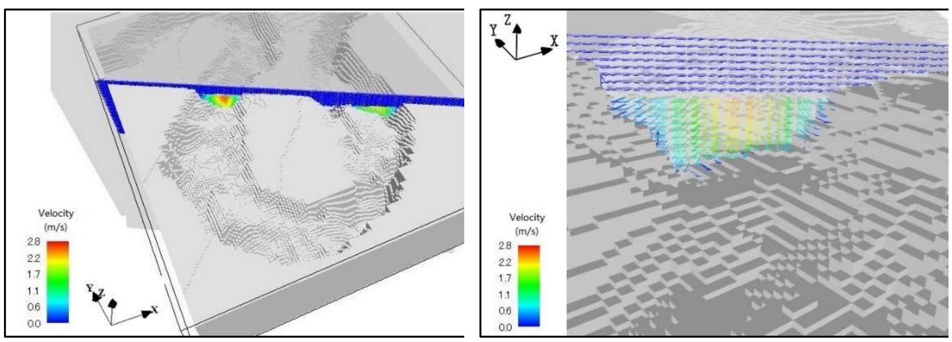

c) Case with Vegetation from KULES (Plane View)

d) Case with Vegetation From KULES (Cross-section)

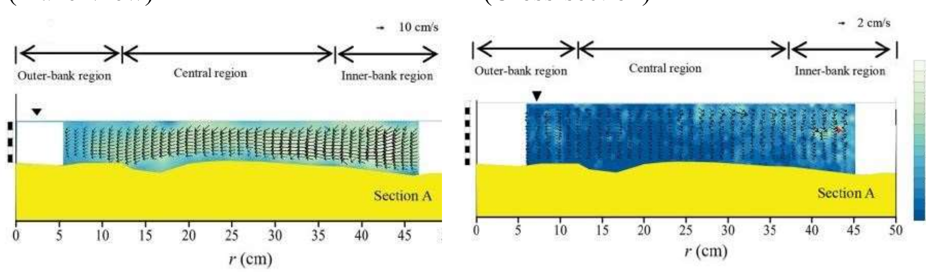

e) Case with Vegetation from Termini' experiment in Section A (Cross-section)

f) Case without Vegetation from Termini's experiment in Section A (Cross-section)

Figure 4.23: Cases with Vegetation and without Vegetation of Both KULES and Termini's Experiment

velocities which are in case with vegetation seems to shift a little bit to the inner bank. Whereby, the red zone in Figure 4.23c (case with vegetation) seems to be closer to inner bank when comparing to Figure 4.23a. (case without vegetation). Such an incident occurs in Termini's experiment as well which can be seen in Figure 4.24. The inhibition at the central region can be clearly observed in Figure 4.18d due to the present of vegetation.

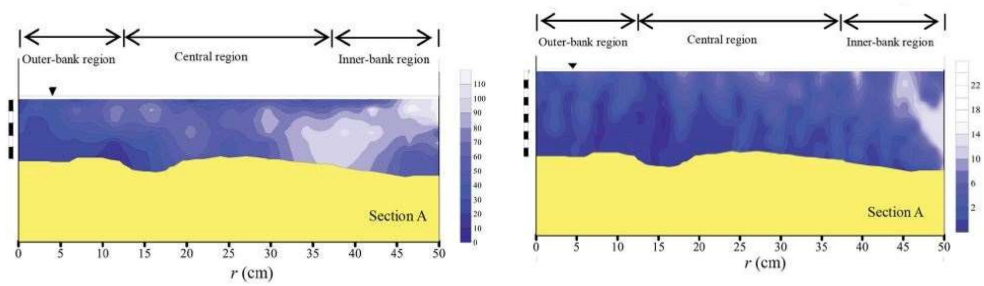

a) Core of high velocity in case without Vegetation

b) Core of high velocity in case with vegetation

Figure 4.24: Core of High Velocity in Cases with and without Vegetation from Termini's Experiment

4.2.2 Simulation of Floating Particles

Besides of the vegetation effects that are simulated by KULES which mentioned in previous section, 110 floating particles with negligible mass are introduced into both simulation cases which are case with vegetation and case without vegetation. Simulation condition remained the same as shown in table 4.3. Size of the floating object are small and their mass are negligible therefore they have very less effect on the flow characteristic. The main purpose of the introduction of floating object is to further describe the flow characteristic by their movement and distribution pattern. Floating object are released at the inflow section which is x=0. The initial position of the floating object is shown in figure 4.25 while the distribution pattern of floating object for both with and without vegetation cases are shown in Figure 4.26.

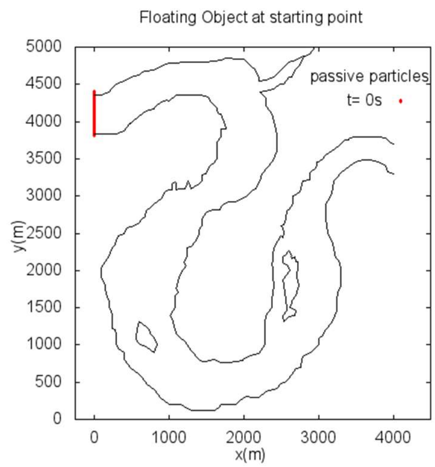

Figure 4.25: Floating Object's Starting Position

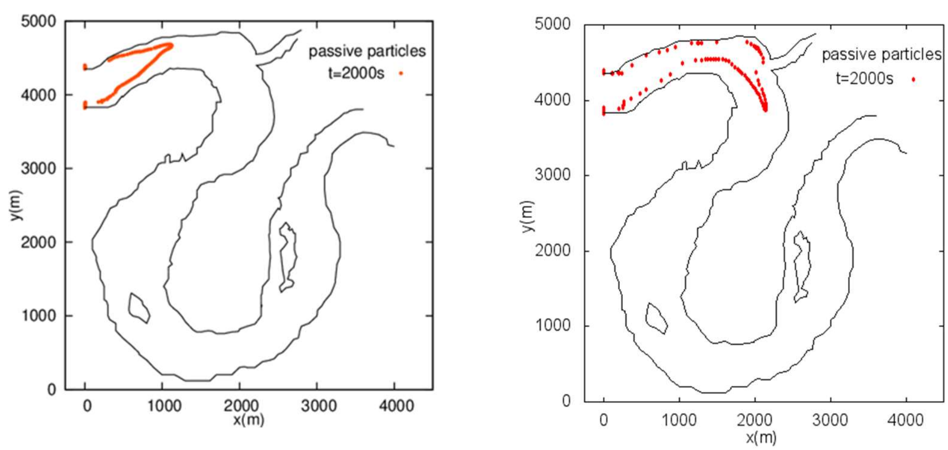

a) t= 2000s, without vegetation b) t=2000s, with vegetation

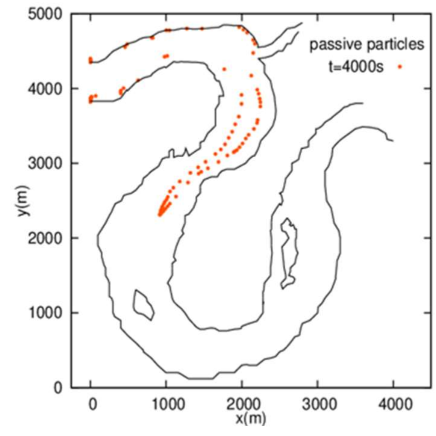

c) t= 4000s, without vegetation

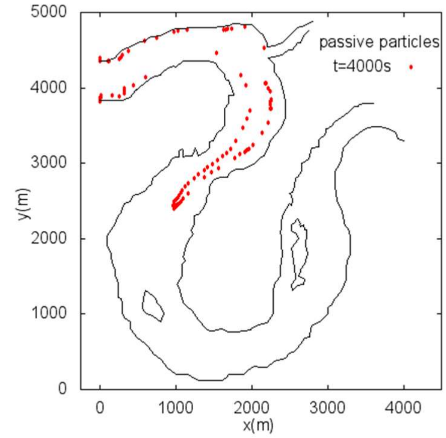

d) t= 4000s, with vegetation

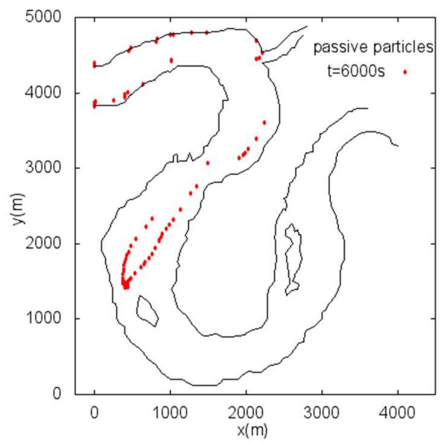

e) t= 6000s, without vegetation

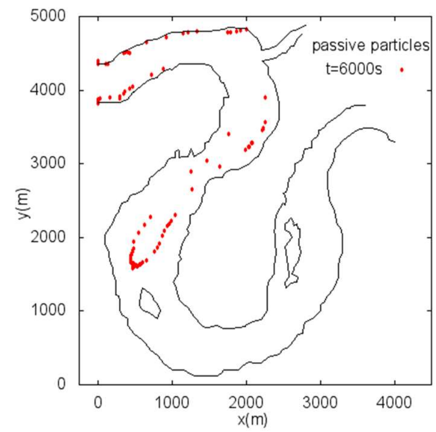

f) t= 6000s, with vegetation

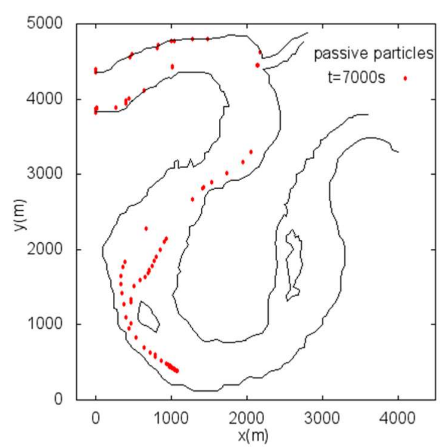

g) t= 7000s, without vegetation

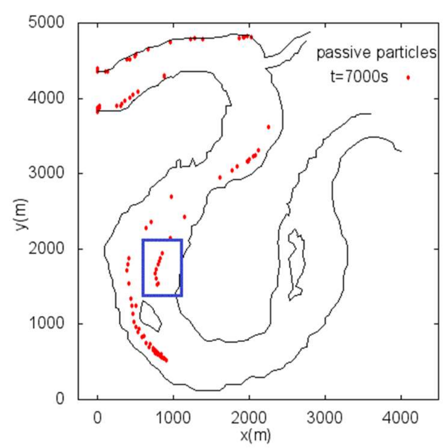

h) t= 7000s, with vegetation

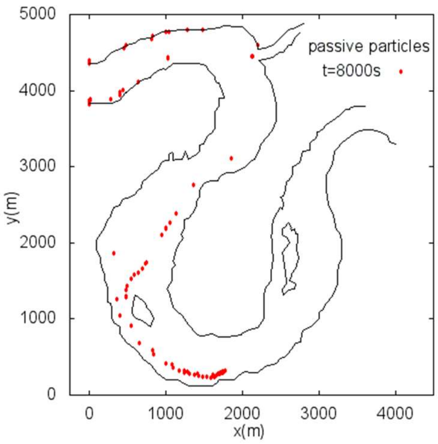

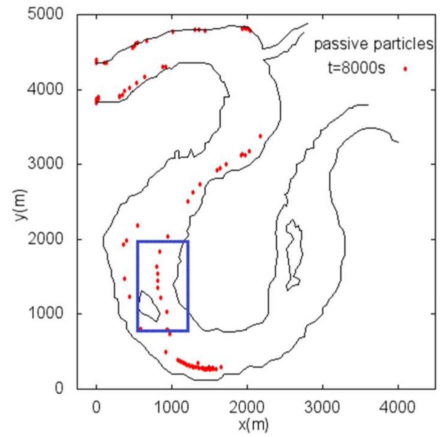

i) t=8000s, without vegetation j) t= 8000s, with vegetation

Figure 4.26: Distribution Pattern of Floating Object in Both Cases of with Vegetation and without Vegetation in Different Time Step

In Figure 4.26, distribution pattern for both cases are almost the same at the time t=4000s until t=4000s which are shown in Figure 4.26 a, 4.26 b, 4.26 c and 4.26 d. However, the pattern of the distribution start to vary after t=6000s. In Figure 4.26 e, the distribution pattern is more likely to be a sharper “V” shape while on the other hand, Figure 4.26 f, the shape is less sharp and seems to be more retarded. At the time after t=7000s, obvious difference of the distribution pattern is formed, which can be seen by the blue square region in figure 4.26 h and Figure 4.26 j whereby the particles from the case with vegetation start to cling to inner bank as shown in figure. This phenomenon can further explain and support the statement in previous section which is core of high velocity tend to shift toward to inner bank when there is present of vegetation.

LES simulation runs with different hydrograph are also being conducted. Similar to the comparison of cases with and without vegetation aforemention, floating object are introduced into the river during the simulation run. The hydrographs for both run which are Run 1 and Run 2 are shown as Table 4.4. Run 1 has a constant flow rate of 1000 m^3/s while flow rate in Run 2 gradually increased 50 m^3/s every 1800 seconds.

Table 4.4: LES Simulation Runs with Different Hydrograph

Time (s)	**Run 1 (m3/s)**	**Run 2 (m3/s)**
0	1000	400
1800	1000	450
3600	1000	500
5400	1000	550
7200	1000	600
9000	1000	650
10800	1000	700
12600	1000	750

Figure 4.27 below shows the comparison of floating objects' distribution pattern between Run 1 and Run 2 at the time of 2000s, 4000s, 6000s, and 6500s. Difference in the patterns between these two runs start to developed during t= 4000s. During this time, floating objects in RUN 2 (Increasing) start to form distance among themselves while floating objects in RUN 1 (Constant) have more tendency to cling together. From Figure 4.27, there are several differences in the distribution pattern, at the time of 6000s, formation of "V" shape can be seen among the floating objects in RUN 2(Increase) case in Figure 4.27g. While,

floating object still remain gathered in RUN 1(Constant) which is in Figure 4.27 c.

Run 1 (Constant Hydrograph)

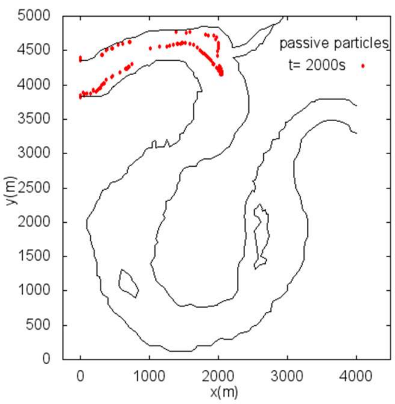

a) Run 1 at t=2000 s

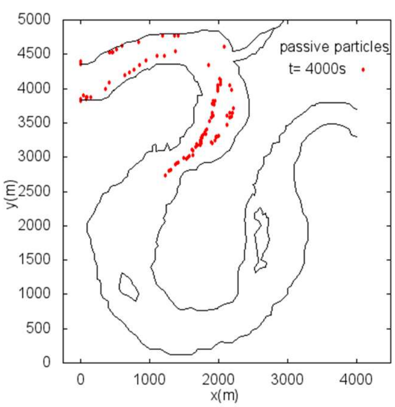

b) Run 1 at t=4000 s

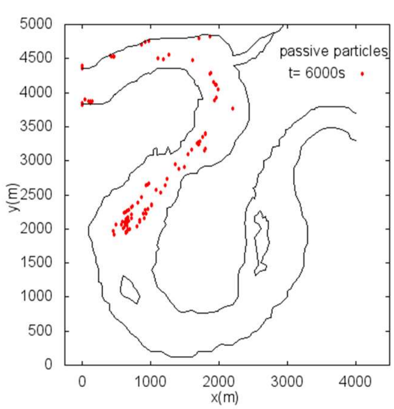

c) Run 1 at t=6000 s

Run 2 (Increase Hydrograph)

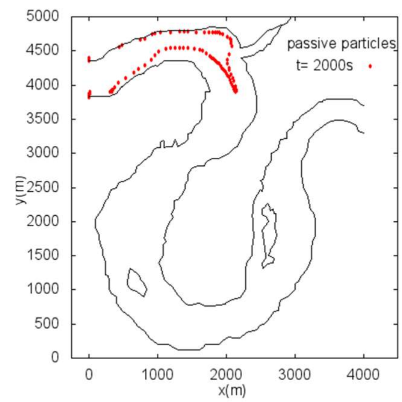

e) Run 2 at t= 2000s

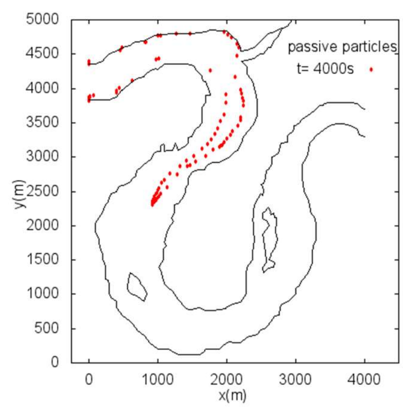

f) Run 2 at t= 4000s

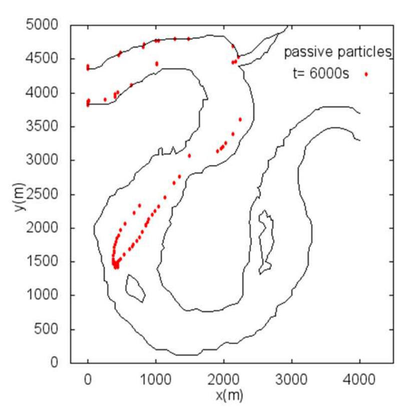

g) Run 2 at t=6000s

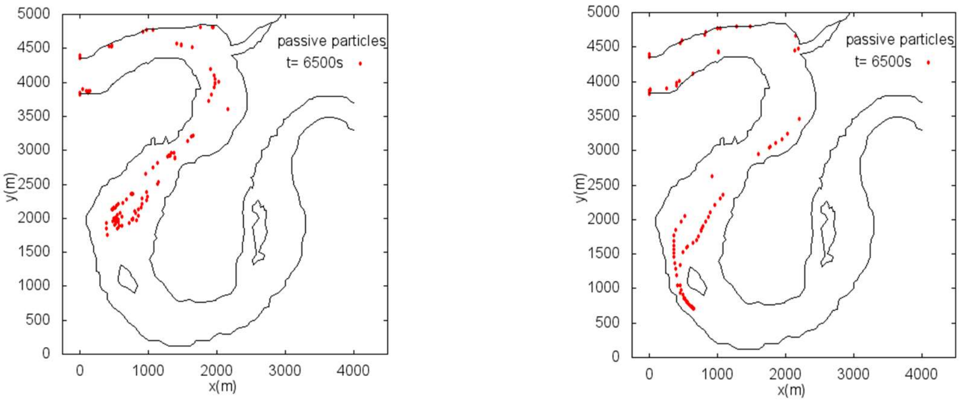

d) Run 1 at t=6500 s h) Run 2 at t=6500 s

Figure 4.27: Comparison of Floating Objects' Distribution Pattern between Run 1 and Run 2

4.2.3 Comparison of LES Simulation Results with ADCP Results

As mentioned in section 1.2 problem statement, despite of the fact that calculation of sediment transportation is not included in present LES, results of bed shear stress is obtained and is shown in Figure 4.28. The value of bed shear stress is directly related to sediment transport.

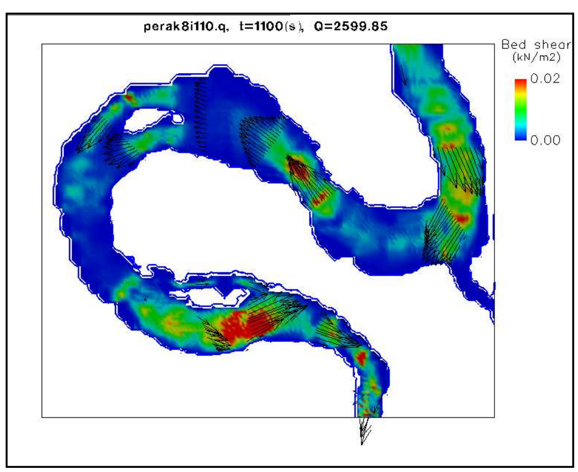

Figure 4.28: Bed Shear Stress Calculate from LES Simulation

Particle size of the sediment transportation could be determined by entrainment function as shown as equation 4.1 below. From the equation, θ_s is the shield entrainment function, τ_0 is the bed shear stress, ρ_s is the density of sediment, and D is the diameter of the particle size.

$$\theta_s = \frac{\tau_0}{(\rho_s - \rho)gD} \tag{4.1}$$

Critical shear stress θ_{CR} is normally estimated to be 0.05 in rough bed condition. According to (Shields,1936), when the entrainment function θ_S is less than the critical shear stress θ_{CR} there will be no sediment transportation occur. Therefore, based on equation 4.1 above, critical particle size D could be determined using the value of bed shear stress. Since increase of particle size in a fix shear stress condition will result in decrease of entrainment function θ_S, it is safe to conclude that sediment that has size larger than critical particle size D will be retained while sediment size that are smaller than the value will be transported downstream. Figure 4.29 below shows the area with different particle size which are calculated using value of bed shear stress from simulation result. Comparison could be made with particle size distribution result obtain from field survey which is shown as figure 4.30 below

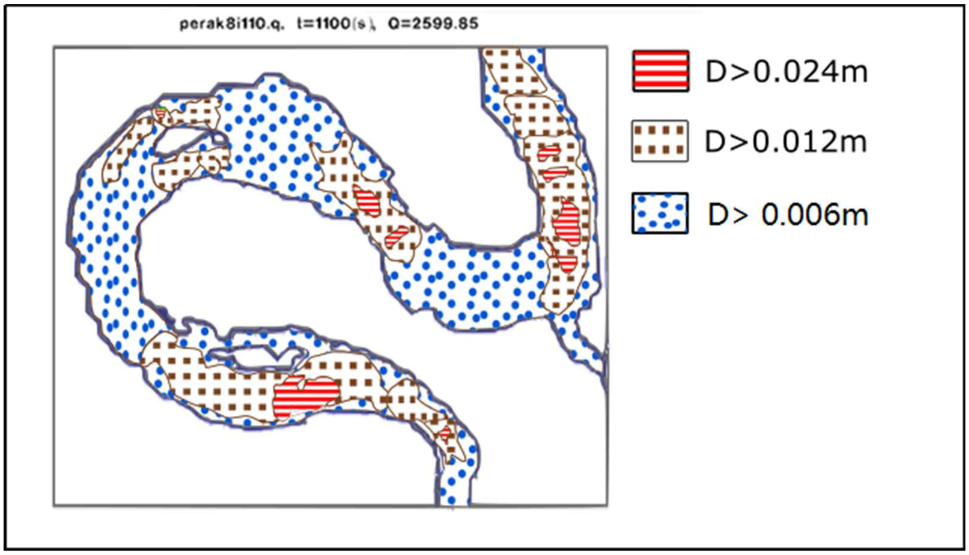

Figure 4.29: Distribution of Different Particle Size

Figure 4.30: Particle Size Distribution (D90)

It is worth mentioning that some of the results from field survey is coincide with figure 4.29. At L1, moderate size of particle size could be found in figure 4.30 which is also shown in figure 4.29 that it is the area with moderate size particles. However, there is some disagreement in L3 area where particle are found to have smaller size which according to Figure 4.29 that the area should have larger particle size. At the area of L4, the particles size distribution are found larger, this could be explained in figure 4.29 that since larger sediment can be transported to downstream from L3 area. Nevertheless, because the bed shear stress in L4 area is weak, and according to figure 4.29, sediment that are larger than 0.006m could not be transported. As a result, larger sediment which are transported from L3 could not be carried away when reaches L4.

Overall, most of the phenomena could be explained in the comparison. However, the simulation result could not be fully consistent with the real situation due to the complex environment. Such as during tidal effect, flow of river might be reversed and the sediment transportation may vary which is the case that is not included in the calculation of simulation.

ADCP result can be used for comparison with LES simulation. ADCP measurement during 17 July 2019. Figure 4.31a below show the path of an ADCP measurement, while Figure 4.32b is the velocity profile from the measurement. Result calculated by LES simulation is shown in Figure 4.32b. Some difference could be observed after comparing Figure 4.31 and Figure 4.32 The highest velocity is found in the left side near the river bank in ADCP result, while the highest velocity from LES simulation seems to be slightly away from the left side of the river bank and much near to the centre. The result from ADCP seems to be different with Simulation results, this might be due to the measuring path of ADCP did not fully reach the bank in the left hand side as shown as Figure 4.31a.

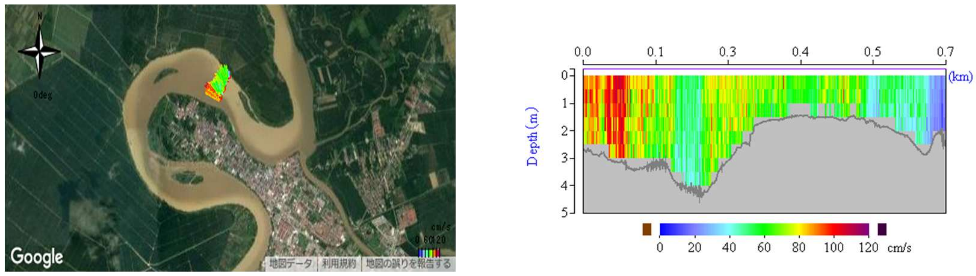

a) Path way of ADCP measurement

b) Velocity profile for ADCP measurement

Figure 4.31: ADCP Measurement's During 17 July 2019

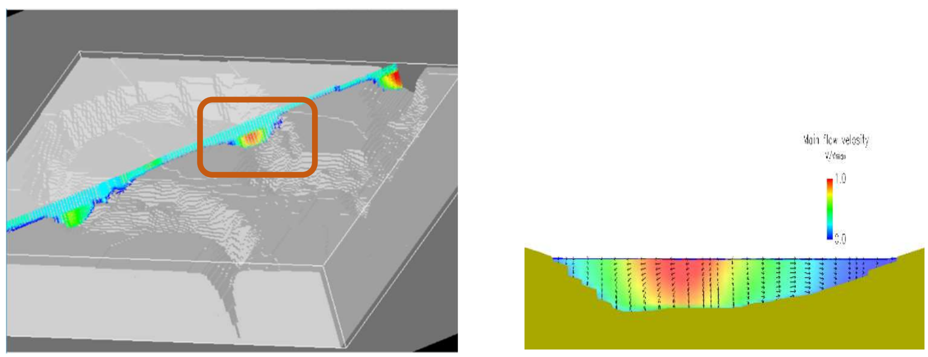

a) Region of ADCP measurement during 17 July 2019

b). Velocity profile calculated by LES simulation

Figure 4.32: Simulation Result in same Region of ADCP Measurement During 17 July 2019

CHAPTER 5

CONCLUSION AND RECOMMENDATION

5.1 Conclusion

Large Eddy Simulation (LES) has been successfully conducted to examine the flow and bed sediment characteristics of the meandering river reach of Perak River in Teluk Intan, Perak. The simulation is done for the area enclosed by about 5km by 5km with acute bends and thick vegetation growth. This part of the river is about 25km from the river mouth and is subjected to the tidal effects. The simulation focused on the flow characteristics when the flow is constant and when the discharge is constantly increasing but in the direction towards the sea. The LES results gave quite detained in spatial and temporal distributions that could be examined for different aspects of the flow and the river.

At the same time as the simulation is conducted, the flow and sediment survey of the simulated part of the river has been conducted. The data also contain detailed flow and sediment characteristics and were examined and used to evaluate the simulation results. The following are the main conclusions derived from the simulation and the field survey.

The flow in the meandering reach with the vegetation effects can by simulated effectively with the LES method used. The results provide the detailed spatial and temporal distribution of the flow and the bed characteristics that can be used to examine various river maintenance works. The results could be examined in several different ways. The surface flow, secondary flows, the bed shear stress distribution and the trajectories of floating objects are some of the results. They showed the distinct curved flow characteristics and the areas of sediment erosion and deposition. The movement and accumulation of floating plants and objects were clarified. The simulation was also conducted to examine the effects of the vegetation on the flow characteristics.

These results could be verified by the field survey conducted over 3 days and the flow data collected over longer period. The surveyed flow characteristics in the real river are quite complex influenced strongly by the tidal effects but the results in the forward flow phase do show the trend of the simulation. The sediment size distribution obtained by sampling indicated the areas of sediment deposition and erosion indicated by the bed shear force predicted by the simulation.

5.2 Recommendation

The field survey indicated the strong tide effects which were not anticipated in the LES simulation. Therefore, the recommendation for the future work is to include the tidal effects. Since the LES simulation must resolve the three-dimensional turbulent motion with sufficiently small spatial resolution, it will increase the computational loads for workstation type computers to cover the time period of one tidal cycle. The long time and longer reach simulation can be done easier by using the existing one-dimensional analysis method or depth-averaged 2-dimensional methods. But the three-dimensional analysis focusing on the specific areas such as the acute bend and with the strong effects of vegetation. As the present dissertation is written, the discharge of Perak River also increased during December 2021 flooding reaching a warning level at the outer bank of the downstream bend in the simulation region. A simulation corresponding to the expected high discharge will be useful to evaluate the flow characteristics and possible counter measures.

REFERENCES

Anderson, J.D. and Wendt, J., 1995. *Computational fluid dynamics* (Vol. 206, p. 332). New York: McGraw-Hill.

Estrada, M.A.R., Koutronas, E., Tahir, M. and Mansor, N., 2017. Hydrological hazard assessment: THE 2014–15 Malaysia floods. *International journal of disaster risk reduction*, *24*, pp.264-270.

Balaras, E., 2004. Modeling complex boundaries using an external force field on fixed Cartesian grids in large-eddy simulations. *Computers & Fluids*, 33(3), pp. 375–404.

Van Balen, W., Uijttewaal, W.S. and Blanckaert, K., 2010. Large-eddy simulation of a curved open-channel flow over topography. *Physics of Fluids*, *22*(7), p.075108.

Blanckaert, K., 2010. Topographic steering, flow recirculation, velocity redistribution, and bed topography in sharp meander bends, *Water Resources Research*, 46(9), pp. 1–23.

Blanckaert, K. and Graf, W.H., 2004. Momentum transport in sharp open-channel bends. *Journal of Hydraulic Engineering*, *130*(3), pp.186-198.

Chan, N. W., 2015. Resilience and Recovery in Asian Disasters. *Resilience and Recovery in Asian Disasters*, pp. 239–265.

Demuren, A. O. and Rodi, W., 1986. Calculation of flow and pollutant dispersion in meandering channels. *Journal of Fluid Mechanics*, 172(1), p. 63.

Department of Irrigation and Drainage. (2012) *Government of Malaysia Department of Irrigation and Drainage Urban Stormwater Management Manual for Malaysia MSMA 2 nd Edition*.

DID (2000) *Urban Storm Water Management Manual For Malaysia*. Percetakan Nasional Malaysia Berhad.

EM-DAT, C.R.E.D., 2015. Centre for Research on the Epidemiology of Disasters. *The International Disaster Database.* Available online: www. emdat. be

Gibert, J., Danielopol, D. and Stanford, J.A., 1994. Groundwater ecology. Academic Press.

Gleick, P.H., 1993. *Water in Crisis* (Vol. 100). New York: Oxford University Press.

Hamid, H.E., MSaad, N.J.A., Mat Razali, N.A., Khairuddin, M.A., Ismail, M.N., Ramli, S., Wook, M., Ishak, K.K., Ishak, Z., Hasbullah, N.A. and Wahab, N., 2019, November. Disaster management support model for Malaysia. In

International Visual Informatics Conference (pp. 570-581). Springer, Cham.

Hirt, C. W. and Cook, J. L., 1972. Calculating three-dimensional flows around structures and over rough terrain. *Journal of Computational Physics*, 10(2), pp. 324–340.

Hodges, B. R. and Street, R. L., 1999. On Simulation of Turbulent Nonlinear Free-Surface Flows. *Journal of Computational Physics*, 151(2), pp. 425–457.

International Energy Agency (2021), *Hydropower*, IEA, Paris https://www.iea.org/reports/hydropower

Maxwell, J.C., 1856. Theory of the perception of colors. *Trans. R. Scottish Soc. Arts*, *4*, pp.394-400.

Joung, Y. and Choi, S.U., 2010. Direct numerical simulation of low Reynolds number flows in an open-channel with sidewalls. *International journal for numerical methods in fluids*, *62*(8), pp.854-874.

Kruse, J. *et al.,* 2011. The Upper Mississippi and Illinois Rivers as Grain Transport Arteries: A Spatial Equilibrium Analysis. *Journal of the Transportation Research Forum*, 47.

LEE, S. and Choi, S.U., 2017. Impact of Inner-bank Vegetation on the Mean Flow and Turbulence Statistics in a Curved Channel. *IAHR World Congress Proceeding,* 37, pp. 282-286

Lemmin, U. and Rolland, T., 1997. Acoustic velocity profiler for laboratory and field studies. *Journal of Hydraulic Engineering*, *123*(12), pp.1089-1098.

Liu, X. and Zeng, Y., 2017. Drag coefficient for rigid vegetation in subcritical open-channel flow. *Environmental Fluid Mechanics*, *17*(5), pp.1035-1050.

Mohd Taib, Z., Jaharuddin, N. S. and Mansor, Z., 2016. A Review of Flood Disaster and Disaster Management in Malaysia, *International Journal of Accounting and Business Management*, 4(2), pp. 98–106.

Nakayama, A., 2012. Large-eddy simulation method for flows in rivers and coasts constructed on a cartesian grid system. *Memoirs of Construction Engineering Research Institute*, *54*, pp.13-27.

Nakayama, A., Noda, H. and Maeda, K., 2004. Similarity of instantaneous and filtered velocity fields in the near wall region of zero-pressure gradient boundary layer. *Fluid Dynamics Research*, 35(4), pp. 299–321.

Nakayama, A. and Asami, K., 2020. Mechanism of maintaining cobble-bar vegetation and the geomorphic conditions for existence of refugia during large floods. *Journal of Hydro-Environment Research*, *30*, pp.91-99.

Nakayama, T., 1997. Turbulent structures and characteristics of coherent vortices near the free-surface. *Master's thesis, Kyoto University*.

Nakayama, T., 2000. Turbulence and coherent structures across air-water interface and relationship with gas transfer. *PhD thesis, Kyoto University*.

Nepf, H.M., 1999. Drag, turbulence, and diffusion in flow through emergent vegetation. *Water resources research*, *35*(2), pp.479-489.

Robinson, S. K., 1991. Coherent Motions in the Turbulent Boundary Layer. *Annual Review of Fluid Mechanics*, 23(1), pp. 601–639.

Rodi, W., Constantinescu, G. and Stoesser, T., 2013. Large-Eddy Simulation in Hydraulics.

Sharma, V. K. and Priya, T., 2001. Development strategies for flood prone areas, case study: Patna, India. *Disaster Prevention and Management: An International Journal*, 10(2), pp. 101–110.

Shimada, R., Kimura, I. and Shimizu, Y., 2011. Study on 3D flow structures and bed deformations in curved open channels. *Journal of Japan Society of Civil Engineers, Ser. A2 (Applied Mechanics (AM))*, *67*(2), pp.I_703-I_712.

Smagorinsky, J., 1963. General circulation experiments with the primitive equations: I. The basic experiment. *Monthly Weather Review*, *91*(3), pp.99-164.

Shields, A., 1936. Application of similarity principles and turbulence research to bed-load movement.

Termini, D., 2017. Vegetation effects on cross-sectional flow in a large amplitude meandering bend. *Journal of Hydraulic Research,* 55(3), pp.423-429.

Termini, D. and Di Leonardo, A., 2018. Turbulence structure and implications in exchange processes in high-amplitude vegetated meanders: Experimental investigation. *Advances in Water Resources*, 120, pp.114-127.

Vardy, A.,1990. *Fluid Principles*. London: McGraw-Hill Education - Europe.

Versteeg, H. k. and Malalasekera, W., 2007. *An Introducion to Computational Fluid Dynamics The Finite Volume Method*. 2nd edn. Pearson Education Limited.

Wilson, N.R. and Shaw, R.H., 1977. A higher order closure model for canopy flow. *Journal of Applied Meteorology*, *16*(11), pp.1197-1205.

Yang, J.Q. and Nepf, H.M., 2019. Impact of vegetation on bed load transport rate and bedform characteristics. *Water Resources Research*, *55*(7), pp.6109-6124.

Zeng, J., Constantinescu, G., Blanckaert, K. and Weber, L., 2008. Flow and bathymetry in sharp open-channel bends: Experiments and predictions. *Water resources research*, 44(9).

LIST OF PUBLICATION

Goh, H.T. and Nakayama, A., 2019, September. Numerical study of transport and accumulation of floating objects in Perak River during floods. In *AIP Conference Proceedings* (Vol. 2157, No. 1, p. 020003). AIP Publishing LLC.

Goh,H.T., Chai, S.N. and Nakayama,A., 2018. Characteristics of transport of floating objects in meandering vegetated. In *International Symposium on Environmental Hydraulics ISEH 2018*, pp.32-25,

Goh. H.T and Nakayama, A., 2019. Numerical study of transport and accumulation of floating objects in Perak River during floods. In *International Symposium on Green & Sustainable Technology ISGST*

Nakayama, A., Chai, S.N. and Goh, H.T., 2018. Numerical Simulation of Transport and Accumulation of Floating Objects in Meandering River. *Journal of Japan Society of Civil Engineers*, *74*(4), pp.I_751-I_756.